High Efficiency Thermophotovoltaic Microgenerators

by

Walker R. Chan

B.S., Massachusetts Institute of Technology (2008)
M.Eng. Massachusetts Institute of Technology (2010)

Submitted to the Department of Electrical Engineering and Computer Science
in partial fulfillment of the requirements for the degree of

Doctor of Philosophy

at the

MASSACHUSETTS INSTITUTE OF TECHNOLOGY

June 2015

Author .....
Department of Electrical Engineering and Computer Science
May 20, 2015

Certified by .....
Dr. Ivan Celanovic
Principal Research Scientist
Thesis Supervisor

Accepted by .....
Professor Leslie A. Kolodziejski
Chair of the Committee on Graduate Students

High Efficiency Thermophotovoltaic Microgenerators

by

Walker R. Chan

Submitted to the Department of Electrical Engineering and Computer Science
on May 20, 2015, in partial fulfillment of the
requirements for the degree of
Doctor of Philosophy

Abstract

We proposed, designed, and demonstrated a first-of-a-kind millimeter-scale thermophotovoltaic (TPV) system using a metallic microburner, photonic crystal (PhC) emitter, and low bandgap TPV cells. Many technologies (fuel cells, Stirling, thermoelectric, etc.) that potentially enable a portable millimeter-scale hydrocarbon microgenerator are under active investigation because conventional fuels offer energy densities fifty times that of batteries. In a TPV system, combustion heats an emitter to incandescence and the resulting thermal radiation is converted to electricity by photovoltaic cells. Our approach uses a moderate temperature (1000–1200°C) microburner coupled to a high emissivity, high selectivity PhC selective emitter and low bandgap TPV cells. The PhC emitter and low bandgap cells minimize total microgenerator mass by enabling simultaneous high efficiency and high power density, even at moderate temperatures which allow efficient coupling to the combustion process by reducing undesired heat loss mechanisms. This approach is predicted to be capable of up to 30% efficient fuel-to-electricity conversion within a millimeter-scale form factor.

Although considerable technological barriers need to be overcome to reach full performance, we have performed a robust experimental demonstration that validates the theoretical framework and the key system components. We first demonstrated a first-of-a-kind TPV system built from a 10×10 mm catalytic silicon MEMS microburner with a Si/SiO_2 1D PhC matched to the InGaAsSb ($E_g = 0.55$ eV) cells which achieved 2.7% fuel-to-electricity efficiency, a millimeter-scale record, at a power of 344 mW_e. We then proposed, designed, and demonstrated a highly robust metallic platform comprised of a 20×20 mm Inconel microburner and a higher performance 2D tantalum PhC emitter. With the new system, we experimentally demonstrated a similar efficiency but can achieve 5% with simple mechanical improvements. These two experimental demonstrations will pave the way for a lightweight, high energy density TPV microgenerator. We modeled a complete microgenerator based on the experimental system and found an energy density of 850 Wh/kg and power density of 40 W/kg are achievable.

Thesis Supervisor: Dr. Ivan Celanovic
Title: Principal Research Scientist

Acknowledgments

I would like to express my sincere gratitude to my advisor Dr. Ivan Celanovic for his inspiration, support, guidance, and encouragement. I would also like to thank Dr. Jay Senkevich for his advisement and for lively and insightful discussions. I wish to acknowledge the thesis committee: Prof. Marin Soljacic, Prof. John Joannopoulos, Prof. Jeffery Lang, and Prof. David Perreault, for their advice and feedback.

I wish to express my warmest thanks to the present and former members of the TPV group: Veronika Stelmakh, Xiawa Wang, Ognjen Ilic, Dr. Adrian Yeng, Dr. Veronika Rinnerbaurer, Daniel Peykov, Dr. Sidy Ndao, Dr. Peter Bermel, Mohammad Araghchini, visiting student Dr. Alejandro Datas, and UROPs Nate Pallo, Shavi Sukesh, and Elaina Chai. I wish to specifically acknowledge Nate for characterization of the cells and his work on the MPPT, Mohammad for fabricating the silicon microburners, Shavi for his work on the microburner packaging, and Elaina for her work on cell packaging, Peter for performing the numerical optimization of the Si/SiO_2 emitter, and Veronika Stelmakh for providing the 2D Ta PhCs. On a personal level, I would like to thank Nate, Elaina, and Veronika Stelmakh for their friendship.

This work would not have been possible without the support of Dr. Christine Wang of MIT Lincoln Laboratory who provided the InGaAsSb cells used in this work and the assistance of Leo Messigia and Peter OBrien who performed the initial packaging and ARC deposition. I am indebted to Dr. Chris Marton, Dr. Brandon Blackwell, and Prof. Klavs Jensen for providing the silicon microburner and for their ongoing assistance and advisement as well as for teaching me basic chemical engineering. I would like to thank Prof. Ben Wilhite of Texas A&M for performing the CFD analysis of the Inconel microburner, assisting with the experiments, and for advisement on microburner design.

I wish to thank all the dedicated MIT staff who made it possible to conduct this work: Mark Belanger of the Edgerton Shop, Kurt Broderick of EML, and Amy Tatem-Bannister and Bill DiNatale of ISN. I would like to specifically acknowledge Mark for teaching me machining and for his patience and assistance machining difficult materials. I also wish to thank the lab staff of our collaborating institutions: Meredith Metzler of Cornell for

depositing the Si/SiO_2 emitter, and Andrew McGhie and Steven Szewczyk of University of Pennsylvania for performing the DSC and CTE measurements of the solder glass.

Last but not least, I would like to thank my parents and family for both their love and support and for instilling a love of science from an early age.

Contents

List of Figures

List of Tables

List of Symbols

A_s	Area of the sides of the microburner
A_t	Cross sectional area of the microburner support tubes
A_e	Emitter area
C_p	Heat capacity
D	Diffusivity
D_h	Hydraulic diameter
E_g	TPV cell bandgap
F	Radiative view factor between the emitter and cells
I_0	TPV cell saturation current, dark current
I_{ph}	Photocurrent
I_{sc}	TPV cell short circuit current
K_{hs}	Heat sink thermal conductance
L_t	Length of the microburner support tubes
M_f	Fuel mass
M_g	Microgenerator dry mass
M_{tot}	Total (microgenerator and fuel) mass
P_p	Pumping power for heat sink
P_{net}	Net electrical power output
Q_{cavity}	Radiation lost in transit to the cell
Q_{cell}	Radiation incident on the cell
Q_{comb}	Heat of combustion of the fuel in the microburner
Q_{cond}	Heat conducted down the support tubes of the microburner

Q_{elec}	Electrical output of the cell
Q_{emit}	Heat radiated from the emitter
Q_{exh}	Heat lost out the exhaust of the microburner
Q_{iv}	Electrical losses in the cell
Q_{out}	Net power produced by microgenerator
Q_{side}	Heat radiated from the edges of the microburner
Q_{spec}	Radiation with wavelengths outside the cell's QE
R_s	TPV cell series resistance
R_{sh}	TPV cell shunt resistance
T_a	Ambient temperature
T_b	Microburner temperature
T_g	Glass transition temperature
T_j	TPV cell junction temperature
V_{oc}	TPV cell open circuit voltage
η_{rec}	Recuperator effectiveness
λ	Wavelength
λ_g	TPV cell bandgap expressed as a wavelength
ϕ	Equivalence ratio, oxygen to fuel ratio relative to stoichiometric
ρ_c	Diffuse reflectance of TPV cell
ρ_e	Diffuse reflectance of emitter
σ	Stefan-Boltzmann constant
τ_d	Diffusion time
τ_r	Residence time
τ_x	Reaction time
ε_e	Emissivity of the emitter
ε_s	Emissivity of the sides of the microburner
ε_{in}	In-band emissivity of step function emitter
ε_{out}	Out-of-band emissivity of step function emitter
c	Speed of light
e	Elementary charge

$e_b(\lambda, T)$	Blackbody spectrum given by Plank's Law
h	Plank's constant
k_B	Boltzmann constant
n	TPV cell ideality factor
$\dot{n}$	Molar flow rate
p	Mission power density
p_0	Characteristic power density
q_{ci}	Heat flux into TPV cell
q_{co}	Heat flux out of TPV cell
q_{ei}	Heat flux into emitter
q_{eo}	Heat flux out of emitter
u	Mission energy density
u_∞	Characteristic energy density
EQE	TPV cell external quantum efficiency
FF	TPV cell fill factor
IQE	TPV cell internal quantum efficiency

Chapter 1

Introduction

Today's soldiers carry upwards of twenty pounds of batteries on a three day mission to power their electronics [1, 2]. The power demand of a soldier's electronics falls into an awkward range: it is too large to be comfortably supplied by low energy density batteries yet is too small to warrant the weight of a conventional generator. Microgenerators promise to fill this awkward power range by extending the high energy density of conventional fuels into the millimeter-scale.

This thesis presents the evolution of a millimeter-scale propane-fired thermophotovoltaic (TPV) microgenerator. Thermophotovoltaics is a method of converting heat to electricity using infrared light as an intermediary. Our motivation is to tap into the high energy density of hydrocarbon fuels for portable power generation in the 1–100 W range where batteries are insufficient but a traditional generator would be overkill. Typical hydrocarbon fuels have energy densities close to 12.8 kWh/kg (46 MJ/kg) whereas state of the art rechargeable batteries are closer to 180 Wh/kg (0.6 MJ/kg) as in Table 1.1. Thus, even a relatively inefficient generator can significantly exceed the energy density of batteries.

The idea of carrying a microgenerator to supplement or replace batteries has been around well before modern portable electronics. Since the 1960s, the military has been pursuing microgenerators. Many different technologies have been researched since for both military and commercial applications: advanced batteries, fuel cells, mechanical engines, thermoelectrics, thermophotovoltaics, and other more exotic technologies [1–5]. Nevertheless, batteries remain ubiquitous in the 1–100 W range.

Energy source	Type	Energy density	
Hydrogen	Fuel	120.7 MJ/kg	33 528 Wh/kg
Propane	Fuel	46.2	12 833
Gasoline	Fuel	43.4	12 055
Diesel	Fuel	42.6	11 833
Methanol	Fuel	20.1	5583
Li-$SOCl_2$	Primary	1.69	470
Hydrogen (hydride)	Fuel	1.0	278
Li-SiO_2 (BB-5590)	Primary	0.88	246
Lithium ion	Rechargeable	0.65	180
Ni-MH	Rechargeable	0.25	70

Table 1.1: Energy density of fuels and batteries. Energy density of fuels was calculated from their lower heating value.

There are many lessons to be learned from these microgenerators. As an illustrative example, we will look at one: the commercially available Horizon MiniPak. The 120 g MiniPak is a palm-sized proton exchange membrane hydrogen fuel cell with a nominal 2 W electrical output designed for battery recharging [6]. Ten liters of hydrogen are stored in a 105 g metal hydride filled cartridge that can supply 14 Wh. The system is pictured in the inset of Fig. 1-1.

The common motivation for microgenerators is the limited battery life of consumer electronics. Many have long fantasized about butane powered phones and hydrogen powered laptops. Perhaps the time has come, as one review of the MiniPak boldly declared, "this *is* an important date in technology history because run-time will soon cease to be a limiting factor to productivity, connectivity, and lifestyle-enhancing [electronics]" [7]. However, the numbers tells a different story. We plotted the required mass to provide 2 W for a given amount of time, using both the MiniPak and a typical lithium-ion battery, in Fig. 1-1. Under no circumstances is the total weight one must carry reduced by using the MiniPak

Even if we could build a 2 W hydrocarbon-fueled microgenerator that weighs 200 g and has a net fuel-to-electricity efficiency of 5%, it is of dubious utility to the average consumer. As in Fig. 1-1, this microgenerator only beats the battery after 15–20 hours of *continuous* operation. Every microgenerator has a fundamental timescale that describes how long it must run to effectively amortize its dry weight which is typically a day to a week. A single

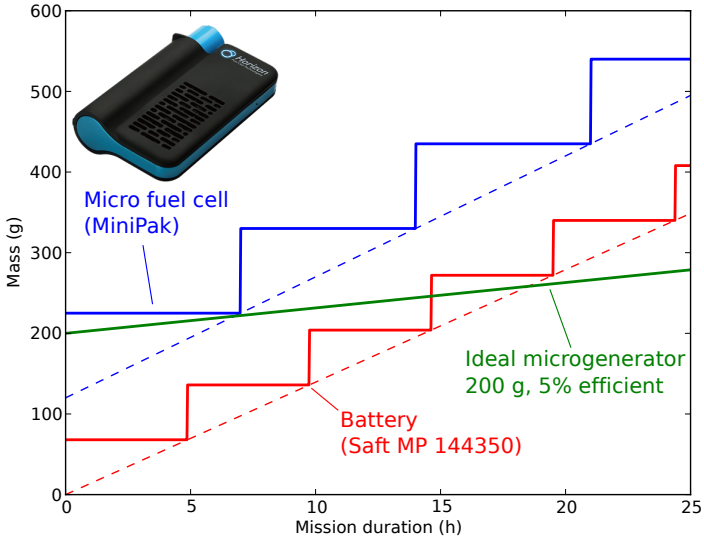

Figure 1-1: Beginning-of-mission mass required to supply 2 W for a given mission duration. A battery, the MiniPak, and an ideal hydrocarbon-fueled microgenerator with a mass of 200 grams and a fuel-to-electricity efficiency of 5% are considered. The dashed lines indicate the limit as the fuel cartridges or batteries become small.

day is simply too short justify the mass of the microgenerator even though the fuel alone is lighter than batteries. Given that a typical consumer is rarely far from the electrical grid, and almost never without access to electricity for more than 24 hours, initial technology demonstration efforts should be directed towards long duration applications because these make best use of the high energy density of hydrocarbon fuels and penalize the generator weight the least. Examples of these missions are powering a dismounted soldier on a three day mission, a remote sensor on an oil pipeline, or an autonomous robotic platform on a long mission. These applications will allow the technology to gain traction by creating a market and generating sales that will fuel further development and performance improvements leading to an eventual consumer market.

The final issue with the MiniPak is that hydrogen is not a good fuel because of its low volumetric density—even liquid hydrogen has a volumetric energy density less than 25% that of gasoline. When stored in a metal hydride as in the MiniPak, the gravimetric energy density is too low to compete with lithium batteries. Furthermore, hydrogen is not readily available, eliminating the opportunity to refuel in the field and the associated reduction in

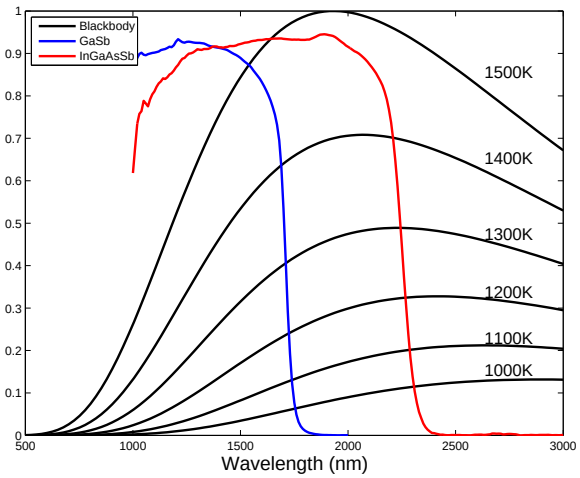

Figure 1-2: Blackbody spectra and QE of some common TPV cells.

total weight and increase in mission flexibility.

TPV is another approach to microgeneration that promises to solve many of the problems of the MiniPak. A TPV microgenerator can burn easy-to-store hydrocarbon fuels, has an inherently high power density, and promises a reasonable efficiency. There are clearly defined routes towards better efficiency that can be deployed once acceptable system performance is demonstrated. Of course TPV is not without its own challenges, primarily associated with the high temperatures involved.

1.1 TPV background

TPV is a method of converting heat to electricity using infrared light as an intermediary, essentially an optical heat engine. Combustion heats an emitter to incandescence and the resulting thermal radiation is converted to electricity by a photovoltaic (PV) cell. The difference between a PV system and a TPV system is that a TPV system produces its own light—the spectrum does not need to be the solar spectrum or even blackbody and the cells (termed TPV cells) do not need to be silicon.

Figure 1-2 shows the quantum efficiency (QE, ratio of incident photons to electrons at the terminals) of two TPV cells and blackbody spectra at a variety of temperatures. The TPV cell can convert in-band radiation (photon energies above its bandgap corresponding

to wavelengths below its bandgap) reasonably efficiently to electricity. With a blackbody spectrum, the fraction of convertible radiation (the spectral efficiency) is relatively low. Thus, the key challenge of TPV is making efficient use of the thermal radiation. For efficient heat-to-electricity conversion, the thermal radiation spectrum needs to matches the quantum efficiency of the PV cell. This spectral matching can be accomplished with a selective emitter (either natural or engineered) that strongly emits at some wavelengths and weakly emits at others, a cold side filter that transmits some wavelengths to the cell and reflects others back to the emitter, or both. We focus on selective emitters because cold side filters require an extremely low loss optical cavity which is difficult to achieve experimentally.

Despite the seemingly convoluted energy conversion pathway, TPV offers some advantages over batteries and other microgenerator technologies:

- **Static conversion process.** Mechanical engines do not scale down well to the millimeter-scale because an unfavorably high surface area to volume ratio increases frictional and thermal losses. For example, a smaller displacement volume in a piston engine requires a higher operating speed to develop appreciable output power, resulting in increased frictional losses as well as increased noise, vibration, and wear. The TPV conversion process does not fundamentally require moving parts although any microgenerator will likely requires auxiliary cooling and combustion air fans and a fuel pump.

- **High power density.** As seen in Fig. 1-1, the microgenerator itself contributes significantly to the total mass. The TPV conversion process leverages the T^4-dependence of thermal emission and the extreme power density of combustion to achieve a high output power density, resulting in a compact microgenerator.

- **Physically separate hot and cold sides.** The TPV process requires that only the burner and emitter be at high temperatures—both these components are relatively simple which allows for reliability. The difficult conversion to electricity is accomplished separately on the cold side. The hot side and cold size can use materials optimized for their specific functions and can be engineered independently. Further-

more, there are no fundamental temperature gradients across materials which cause thermal stresses during startup and operation.

- **Continuous combustion.** In a TPV system, the fuel is simply combusted in a continuous fashion, which allows for efficient combustion resulting in excellent fuel utilization and low emissions, high power density, multi-fuel operation, and the ability to use conventional fuels such as gasoline, diesel, and JP-8.

Unfortunately, the demonstrated fuel-to-electricity efficiency of TPV has traditionally been limited to a few percent as in Table 1.2. This is not a fundamental limitation: heat-to-electricity efficiencies exceeding 20% have been demonstrated [8] and a 10–15% fuel-to-electricity efficiency is realistic [9]. Furthermore, in this thesis we offer a clear route to higher efficiency that only requires applying recent research to TPV as well as good system-level design and optimization.

1.2 TPV development

The efficiency of a TPV system is largely determined by how well the emission spectrum can be tailored to match the quantum efficiency of the cells [22]. Selective emitters are not a new idea: the history of TPV arguably began in the 1800s with the development of efficient gas lighting which maximized the output of visible light from a gas flame. The key invention of the era was the Welsbach mantle, a woven fabric bag that is imbibed with metallic salts and immersed in a gas flame. Upon the first heating, the fabric burns away and the salts convert to oxides, leaving behind a fine network of ceramic fibers. The rare earth oxides, thorium and cerium oxides in this case, have a high emissivity in the visible and low emissivity in the infrared. Thus, the flame's energy is minimally wasted on infrared radiation—allowing the mantle to reach extreme temperatures where it can emit more effectively in the visible. Furthermore, the oxides can be directly excited by free radicals present in the flame (candoluminescence) resulting in emission exceeding the blackbody limit [23]. The result is that a brilliant white light is emitted from the mantle when in an otherwise invisible gas flame.

The full TPV conversion was first demonstrated by Kolm at MIT Lincoln Laboratory

Year	Temp	Emitter	Filter	Cell	Output	Efficiency	Ref.
1997		Er_2O_3		InGaAs	6.5 W	0.5%	10
1999	1700°C	SiC	interference	GaSb	8.0 kW		11
1999		Yb_2O_3		Si	122 W	1.0%	12
1999	1180°C	coated $TaSi_2$		GaSb	162 W	1.8%	13
2001	1014°C	coated Pt		GaSb	25 W	1.9%	14
2002		Yb_2O_3		Si	1.0 W	3.0%	15
2003	770°C	Si		GaSb	1.0 mW	0.1%	16
2004	1200°C	W		GaSb	3.0 W	1.7%	17
2004	1000°C	SiC	interference	GaSb[1]	135 W	1.5%	18
2004	1093°C	SiC[2]	tandem	InGaAs[4]	13.4 W	23.6%	8
2005	850°C	SiC		GaSb	810 mW	0.6%	19
2013	1427°C	Yb_2O_3[3]		Si[1]	50 W	4.0%	20
2013	800°C	Si/SiO_2[3]		InGaAsSb[1]	344 mW	2.7%	21
2013	740°C	Si[3]		InGaAsSb[1]	220 mW	1.6%	21
2015	800°C	Inconel[3]		InGaAs[1 4]	1.5 W	1.5%	
2015	990°C	Ta PhC[3]		InGaAsSb[1]	1.7 W	2.4%	

Table 1.2: TPV experimental results in literature. (1) external cooling, (2) electrically heated emitter, (3) externally preheated air or pure oxygen, (4) back surface reflector. The last four entries are from this work.

in the 1950s using a Coleman lantern (containing a modern Welsbach mantel) and silicon PV cells [24] but no further research was conducted. TPV was again proposed in the 1960s by Aigrain while at MIT [25], which sparked some interest. The first generation of TPV systems were built in the 1960-70s fueled primarily by the US Army's interest in developing a portable power source. Experiments used high temperature rare earth oxide emitters and silicon or germanium cells. Development slowed because of lack of promising results and the Army eventually chose to pursue thermoelectrics [26, 27].

A system with a rare earth oxide emitter and silicon PV cells was built at the Paul Scherrer Institute: it featured a gas burner that heated ytterbia (Yb_2O_3) mantle to 1400–1500°C which was surrounded by silicon PV cells [20, 29]. The rare earth oxide emitter roughly tailored the thermal emission spectrum to match silicon's bandgap, but the total convertible power available from a source at a temperate attainable by combustion was limited. Additional sources of loss were the poor view factor between the emitter and cells and the lack of an vacuum packaging to prevent convection losses. The systems achieved fuel-to-electricity conversion of 2–3% at 15, 30, and 50 W.

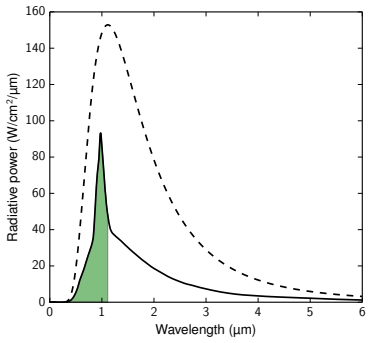

(a) Ytterbia at 2600 K and Si.

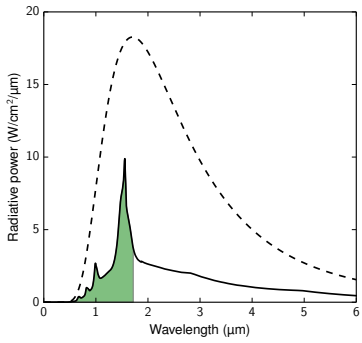

(b) Erbia at 1700 K and GaSb.

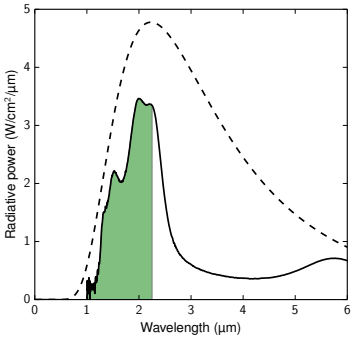

(c) Si/SiO_2 at 1300 K and InGaAsSb.

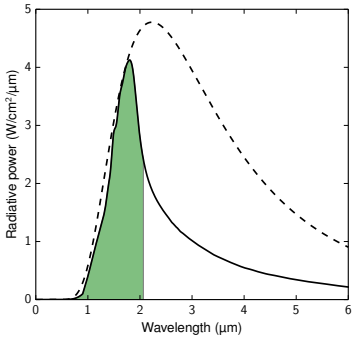

(d) Ta PhC at 1300 K and InGaAsSb.

Figure 1-3: Emission spectrum of rare earth oxides [28] and the photonic crystal emitter used in this work as well as a blackbody at the same temperature. The convertible region of the matched semiconductor is highlighted. Low bandgap cells and high emissivity, high selectivity photonic crystal emitter enable high efficiency and high power density.

Material	Bandgap		Temp.	Emitter
Si	1.11 eV	1.1 µm	2360°C	Yb_2O_3
GaSb	0.72 eV	1.7 µm	1430°C	Er_2O_3
Ge	0.66 eV	1.9 µm	1250°C	Er_2O_3
InGaAs	0.60 eV	2.1 µm	1100°C	Ho_2O_3
InGaAsSb	0.53 eV	2.3 µm	990°C	Ho_2O_3

Table 1.3: Bandgaps for TPV materials. The temperature refers to the temperature of the blackbody whose peak occurs at the bandgap, which corresponds to the peak heat-to-electricity efficiency for a blackbody emitter. The emitter refers to the rare earth emitter whose emission most closely matches the bandgap.

Even if we assume perfect spectral control resulting in blackbody in-band emission and zero out-of-band emission, the theoretical maximum fuel-to-electricity efficiency of a 1460°C Yb_2O_3 emitter and silicon cells is about 10% [20]. The cells are not the problem because silicon cells are highly efficient compared to specialty low bandgap TPV cells—indeed, silicon cells are 85% of their thermodynamic limit. The low system efficiency is mainly due to (1) the low spectral efficiency as seen in Fig. 1-3a and (2) the high temperature required for an appreciable in-band power. The high-temperature emitter is not effectively "impedance matched" to the combustion because it cannot extract a large portion of the flame's heat, otherwise the temperature would drop. As a result, most of the flame's heat is lost out the exhaust.

Interest in TPV was renewed in the 1990s with new developments in III-V semiconductors, enabling low bandgap cells. Despite their low bandgap, previously available Ge cells never performed well because of their high surface recombination rate. The groundwork for high performance, low bandgap cells was laid by Fraas with the development of Zn diffused GaSb cells for GaAs/GaSb tandem solar cells [26]. Other low bandgap cells were soon developed: epitaxial InGaAs on InP and epitaxial InGaAsSb on GaSb cells. Table 1.3 lists TPV cell materials, their bandgaps, and the temperature of the blackbody whose peak occurs at the bandgap.

A low bandgap TPV cell is important for two reasons: (1) it allows a lower temperature to be used reducing heat loss, and (2) it allows a greater portion of the emission spectrum to be captured despite the lower temperature. Ref. 14 describes a self-contained TPV

microgenerator which used a dielectric coated platinum emitter and GaSb cells and achieved about 3% net fuel-to-electricity efficiency at a power of 20 W. Ref. 13 describes a similar microgenerator relying on a dielectric coated $TaSi_2$ emitter. Despite promising initial results on TPV microgenerators, progress towards a high efficiency microgenerator stalled [26], in part because of lack of high performance emitter materials. One of the shortcomings natural selective emitters is their low power density. Low radiated power not only reduces the power density but also lowers the efficiency. The hot side is a highly leaky system: energy that is not radiated is quickly lost through other heat loss mechanisms. Thus, an efficient emitter has not only a high selectivity but also approaches blackbody in the convertible region.

Recent advances in photonic crystals, which allow near perfect control of the thermal emission spectrum, spurred renewed interest in TPV [30–38]. Photonic crystals are classified as 1D, 2D, or 3D according to the number of periodic dimensions and their emission spectrum is primarily determined by the geometry rather than by specific material properties, allowing the cutoff wavelength to be tuned. Moreover, they typically offer near blackbody emission resulting from resonant phenomenon at the desired wavelengths and near zero emission elsewhere resulting form the low loss materials from which they are fabricated. The emission spectrum of the two photonic crystal emitters used in this work are shown in Fig. 1-3c and 1-3d.

We compared the photonic crystal emitter to the natural rare earth oxide emitters in Fig 1-4, where we plotted the in-band radiated power of these emitters as a function of temperature. Ideal emitters (blackbody in-band emissivity and zero out-of-band emissivity) were also plotted. With an ideal emitter and GaSb or InGaAsSb cells, a reasonable power density can be achieved with an emitter under 1200°C which is the practical limit for most high-temperature materials, whereas silicon cells require an impractically high temperature. The photonic crystal emitter allows a high power density to be achieved at a temperature much lower than the natural emitter. Lower temperatures reduce heat loss for higher fuel-to-electricity efficiency and reduce material stressing and associated implementation difficulties.

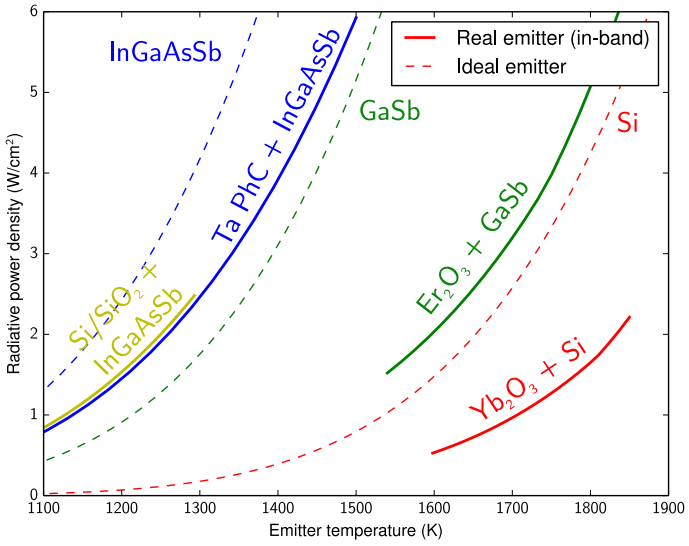

Figure 1-4: In-band (referenced to the indicated cell) radiative power density for real and ideal emitters. An ideal emitter has blackbody in-band emission and zero out-of-band emission, with the cutoff at the cell's bandgap.

1.3 Our approach

This thesis presents a new approach to design of a high efficiency TPV microgenerator system that addresses the fundamental limitations of the historical systems. Our system is comprised of the following components:

- **Moderate temperature suspended microburner.** The microburner is designed to operate at 1000–1200°C, resulting not only in better heat extraction from the combustion process but also reduced thermal stresses resulting in potentially high reliability and larger spectrum of available microburner and emitter materials. The microburner is fully enclosed and thermally isolated from its surroundings to minimize heat loss.

- **High emissivity, high selectivity photonic crystal emitter.** The photonic crystal offers excellent spectral selectivity with near blackbody emission in the convertible region. The downside of the photonic crystal is that it is relatively difficult to fabricate and must be operated in vacuum to prevent oxidation and other contamination.

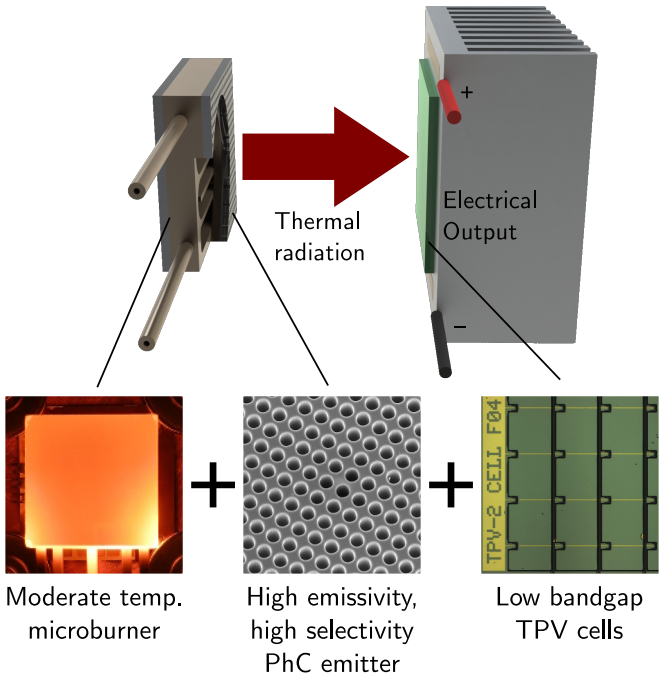

Figure 1-5: The three key components of our TPV system: the moderate temperature microburner, the high emissivity, high selectivity photonic crystal, and the low-bandgap TPV cells.

	Silicon system	Metallic system
Microburner	10 × 10 × 1.4 mm silicon 2× borosilicate (premixed feed) Microfabrication, glass brazing	20 × 20 × 4.2 mm Inconel 2–5× Inconel (segregated feed) Machining, welding
Emitters	(1) Bare silicon (2) Five-layer Si/SiO_2 stack	(1) Bare oxidized Inconel (2) 2D tantalum photonic crystal
Cells	1×1 InGaAsSb array	1×1 InGaAsSb array or 2×2 InGaAs array
Typical operation	<1 hour at 13 W and 800°C	135 hours at 60 W and 1000°C

Table 1.4: Parameters of the two experimental systems developed in this thesis.

The need for vacuum packaging adds greatly to the experimental complexity.

- **Low bandgap TPV cells.** The low bandgap enables a lower temperature emitter while capturing a larger portion of the spectrum, leading to a higher power density and fuel-to-electricity efficiency.

This system differs from the historical systems in its use of a moderate temperature high emissivity emitter. We hypothesize that these innovations will enable a high efficiency, high power density TPV system.

1.4 Thesis contributions

In this thesis we present the evolution of our TPV system and put our results in the context of a microgenerator that is both useful and technically viable. We differentiate between a system and a microgenerator: a system is a laboratory demonstration of the active area with external auxiliary components, whereas a microgenerator is a self-contained package containing the TPV system and all required auxiliary components. Experimentally, we leave the subject of microgenerators unexplored.

The primary contributions were the modeling, design, fabrication, and testing of two TPV systems summarized in Table 1.4:

- **Silicon system.** We built a first-of-a-kind millimeter-scale TPV system with record setting fuel-to-electricity efficiency for that scale. The system used a simple Si/SiO_2

selective emitter deposited directly on a silicon MEMS microburner that doubled the fuel-to-electricity conversion efficiency relative to a bare silicon emitter. Many innovations in the packaging of the microburner were necessary.

- **Metallic system.** The silicon system was limited in its operating temperature and lifetime. We quantified these fundamental limitations, then proposed, designed, and demonstrated first-of-a-kind metallic system to address the shortcomings and improve stability and performance. We then integrated an a tantalum photonic crystal emitter for the first ever demonstration of a photonic crystal in a TPV system.

- **Modeling.** We implemented a semi-analytical system-level multi-physics model that is accurate enough to predict system efficiencies and operating temperatures, yet simple enough to allow for insight. Extensive characterization was performed on each of the individual components (microburner, emitter, and cells) for both systems to provide the parameters of the model. We extended the model to extrapolate the energy density and power density of a TPV microgenerator based on our experimental results.

These three major contributions make great progress towards realizing a TPV microgenerator.

1.5 Thesis organization

This thesis is organized roughly chronologically into five subsequent chapters:

- **Chapter 2** describes the multi-physics TPV system model we developed, with a focus on understanding component behavior and interactions. The model is mainly applied in the following chapters to predict temperature, electrical power output, and energy flows within the TPV system.

- **Chapter 3** describes the characterization of the silicon microburner, the development of a TPV system, our integration of a Si/SiO_2 emitter, our experimental results, and the fundamental limitations of the silicon system.

- **Chapter 4** describes the advantages offered by the metallic system, our design and characterization of the microburner, the TPV system we built with both a bare Inconel emitter and a tantalum photonic crystal emitter.
- **Chapter 5** extends the model from Chapter 2 to extrapolate a the performance of self-contained microgenerator from the results in Chapter 3 and 4.
- **Chapter 6** concludes the work by comparing the modeled TPV microgenerator to other microgenerator technologies and recommends a path towards a TPV microgenerator demonstration.

Additional details needed to reproduce the results are found in the appendices.

Chapter 2

TPV Model

A hydrocarbon TPV system is a complex system involving three major components (a microburner, an emitter, and TPV cells) that exchanges energy across four domains: chemical, thermal, optical, and electrical. We divided the process into three subsystems: (1) the thermal subsystem model describes the conversion of fuel into heat inside the microburner, (2) the optical subsystem model describes the radiation transfer from the emitter to the cell, and (3) the electrical subsystem model describes the conversion from incident photon flux on the cell into electricity delivered to the load. Together, these three subsystems cover the entire fuel to electricity conversion process.

The purpose of the model is to understand the flow of energy within a TPV device: how much of the energy content of the fuel is converted to electricity and how the balance is lost in the conversion process. Experimentally we can only measure the fuel input and electrical output as well as the microburner temperature under some circumstances. Thus, we thus must rely on the model to determine the heat flow within the system. The energy flow can serve as a guide for what improvements will have the greatest benefit to the fuel-to-electricity conversion efficiency.

The energy flows within the TPV system are shown graphically in a Sankey diagram in Fig. 2-1 which is partitioned into the thermal, optical, and electrical domain. The process begins in the thermal domain with the combustion of fuel releasing Q_{comb}. The microburner loses heat out the exhaust (Q_{exh}), by conduction down the support tubes (Q_{cond}), and by radiation from the sides (Q_{side}). Only about half of the energy content of the fuel is radiated

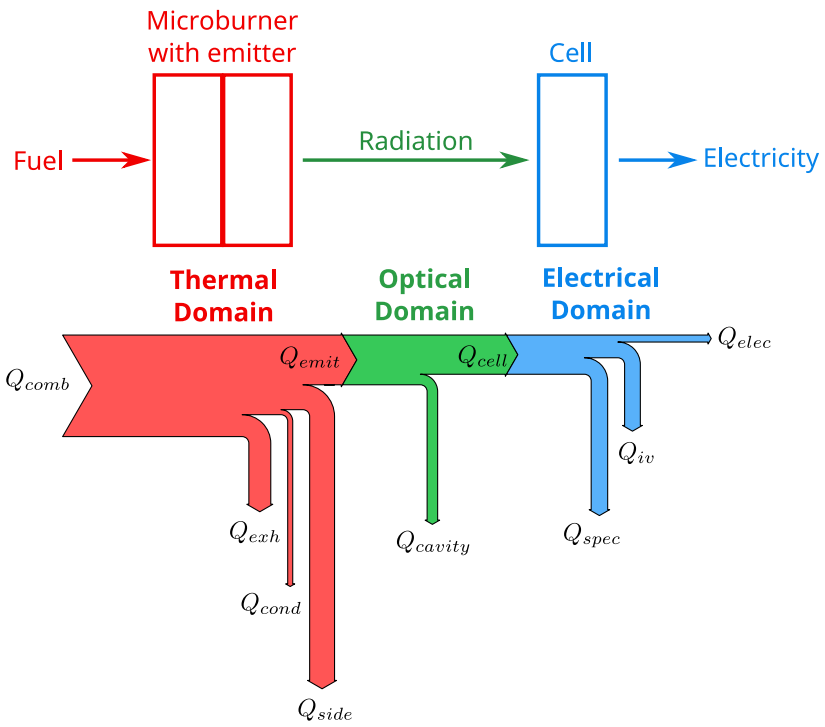

Figure 2-1: A schematic (top) and Sankey (bottom) diagram depicting the energy flow across the thermal, optical, and electrical domains in the modeled TPV system.

from the emitter (Q_{emit}) and continues into the optical domain. Some thermal radiation is lost in transit to the cells (Q_{cavity}) and the rest is incident on the cells (Q_{cell}) and enters the electrical domain. Some energy is lost due to the spectral mismatch between the emitter and cell (Q_{spec}). There are inefficiencies in the cell such as recombination and series resistance that give rise to additional loss (Q_{iv}). A small amount of the original energy is converted to electricity electricity (Q_{elec}), completing the TPV conversion process.

The three domains are treated individually in the next three sections. The thermal domain uses a heat balance to predict the amount of power radiated from the emitter and the microburner temperature. The optical model uses a detailed balance to determine the spectrum incident on the cell. The electrical model integrates the incident spectrum to find the photocurrent then uses parameterized photovoltaic equivalent circuit model to find the electrical output [39]. Each of the domains was modeled accurately enough to be useful but was not made so complex that the fundamental physics was obscured.

2.1 Thermal model

In conjunction with the optical model, the goal of the thermal model is to predict the quantity and spectrum of the radiation injected into the optical cavity from the input fuel flow. A heat- rather than the more common temperature-based model was implemented because in the later, a slight inaccuracy in temperature is amplified by the T^4-dependence when predicting the radiated power. We assumed that the microburner and emitter are at a single, uniform temperature T_b. This is a powerful assumption because it allows every heat flow to expressed algebraically leading to a concise model that does not obscure the underlying physics. The assumption of uniformity does not degrade the accuracy of the model because the TPV cells integrate over the entire area, averaging out any experimental non-uniformity—we have experimentally confirmed this assumption. Another strength of the uniform temperature model is that it is largely independent of the specific microburner design, allowing us to study system level interactions without worrying about the exact internal structure of the microburner.

The heat gain and loss mechanisms that we consider are summarized in Fig. 2-2a, but we will initially focus on just the combustion process. The combustion of propane is

$$\mathrm{C_3H_8} + 5\,\mathrm{O_2}\,(+19\mathrm{N_2}) \longrightarrow 3\,\mathrm{CO_2} + 4\,\mathrm{H_2O}\,(+19\mathrm{N_2}) \tag{2.1}$$

with stoichiometric oxygen (or air). The heat evolved from its complete combustion is

$$Q_{comb} = \dot{n}_f \Delta H \tag{2.2}$$

where $\dot{n}_f$ is the molar flow rate of the fuel and ΔH is the enthalpy of combustion given by the difference in enthalpy of the reactants and products weighted by the stoichiometry of the reaction. We assume that the water in the exhaust exists as vapor (referred to as the lower heating value) rather than liquid (higher heating value). The heat of combustion is transferred to the heat loss mechanisms listed in Fig. 2-2a.

Let us momentarily assume a perfectly insulated microburner whose only heat loss mechanism is the exhaust which is fundamental to the combustion. The resulting heat

balance is

$$Q_{comb} = Q_{exh}. \tag{2.3}$$

The exhaust heat loss is given by a sum over the heat absorbed by the heat capacity of the reaction products:

$$Q_{exh} = \sum_{i \ \epsilon \ \text{prod.}} \dot{n}_i \int_{T_a}^{T_b} C_{p,i}(T) dT \tag{2.4}$$

$$\approx \sum_{i \ \epsilon \ \text{prod.}} \dot{n}_i C_{p,i}(T_b - T_a) \tag{2.5}$$

where T_a is the ambient temperature, T_b is the microburner temperature, $C_{p,i}$ and $\dot{n}_i$ are the molar heat capacity and flow rate of species i, and the sum is over the reaction products i: CO_2, H_2O, excess O_2, and N_2 if using air. The exhaust loss can be approximated by Equation 2.5 which assumes temperature independent heat capacities. The heat balance equation can be solved for the microburner temperature which is the adiabatic flame temperature in this special case. Some fuel-air adiabatic flame temperatures were calculated according to this method and are listed in Table 2.1 with literature values. The values agree to within 200 K. We did not calculate fuel-oxygen adiabatic flame temperatures because they are highly inaccurate primarily because the model neglects the endothermic dissociation of CO_2 and H_2O at high temperatures. These side reactions are not a concern because the microburner operates at a temperature much lower than even the fuel-air adiabatic flame temperature.

We can gain some intuition from a thermal circuit model, where heat is equivalent to current and temperature is equivalent to voltage. The heat of combustion is modeled as a current source and exhaust loss is modeled as a resistor, forming a Norton equivalent circuit as shown in the inset of Fig. 2-2b. The temperature reached by the combustion decreases approximately linearly with the amount of heat extracted as in Fig. 2-2b. The "short circuit current" is heat of combustion and the "open circuit voltage" is the adiabatic flame temperature. The slight nonlinearity due to the temperature-dependent heat capacities in Equation 2.4.

Non-exhaust loss mechanisms are loads to the Norton circuit. We coupled the mi-

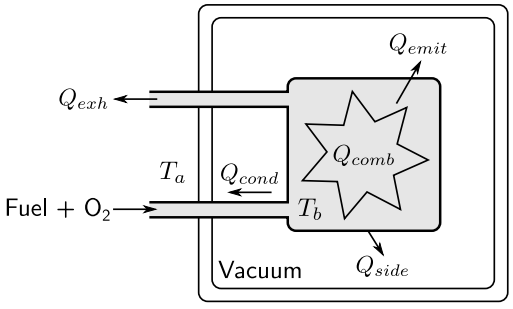

(a) Microburner heat loss mechanisms.

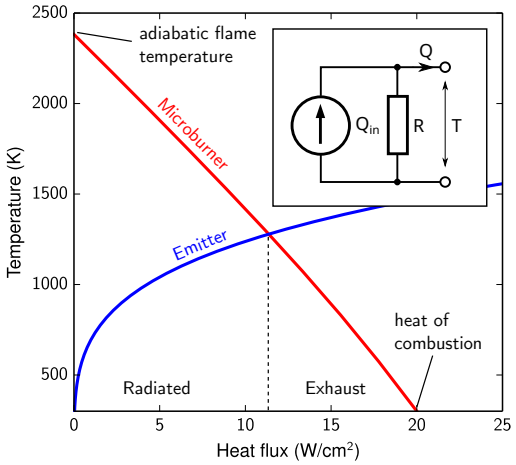

(b) Microburner-emitter model.

Figure 2-2: The heat loss mechanisms considered in this section (a) and a simplified microburner-emitter model only considering combustion, exhaust, and a blackbody emitter.

croburner to a grey body emitter whose radiated power is given by the Stefan-Boltzmann law

$$Q_{emit} = A_e \varepsilon_e \sigma T_b^4 \tag{2.6}$$

where ε_e is the emissivity, A_e is the area, σ is the Stefan-Boltzmann constant, and T_b is the microburner temperature. A single $\varepsilon_e = 1$ curve is plotted in Fig. 2-2b. The microburner and emitter share a single temperature and heat flux, thus the operating point is the intersection of the two curves. The fraction of the heat to the left of the intersection is radiated by the emitter and the fraction to the right is carried out the exhaust. This fraction is termed the burner efficiency. An efficient TPV system requires an effective "impedance match" to maximize transfer heat from the microburner to the emitter, which is obtained with a high emissivity emitter and low temperature microburner.

An efficient TPV system uses a spectrally selective emitter to match the thermal emission to the response of the TPV cell. The exact amount of heat entering the optical cavity must be calculated as in Section 2.2 because a reflective cell will decrease the net heat flux out of the emitter. If we assume that the reflectance is small, the heat loss can be approximated

Fuel	Calculated	Literature
Hydrogen	2510 K	2483 K
Methane	2295 K	2223 K
Ethane	2361 K	2228 K
Propane	2362 K	2210 K

Table 2.1: Stoichiometric fuel-air adiabatic flame temperatures.

from the the emissivity of the emitter:

$$Q_{emit} \approx A_e \int_0^\infty \varepsilon_e(\lambda) e_b(\lambda, T_b) d\lambda, \tag{2.7}$$

where $\varepsilon_e(\lambda)$ is the wavelength dependent emissivity and $e_b(\lambda, T_e)$ is the blackbody spectrum given by Planck's Law,

$$e_b(\lambda, T) = \frac{2hc^2}{\lambda^5} \frac{1}{e^{\frac{hc}{\lambda k_B T}} - 1} \tag{2.8}$$

where λ is the wavelength, h is Plank's constant, c is the speed of light, k_B is the Boltzmann constant, and T is the absolute temperature. For GaSb and InGaAsSb, the above approximation is accurate but the full optical cavity model must be used for InGaAs because of the high reflectivity for $\lambda > \lambda_g$ due a back surface reflector.

The heat loss mechanisms discussed previously (exhaust and radiation from the emitter) are fundamental to TPV. Those discussed next are not fundamental: parasitic radiation and conduction. The parasitic radiation from the sides of the microburner is assumed to be entirely lost, therefore it can be calculated by adapting Eqn. 2.7,

$$Q_{side} = A_s \int_0^\infty \varepsilon_s(\lambda) e_b(\lambda, T_b) d\lambda \tag{2.9}$$

where A_s is the area of the sides, $\varepsilon_s(\lambda)$ is the emissivity of the sides, and other variable are as before. Edge radiation is a major source of loss because edges are 20–30% of the total surface area and emissivity are higher than the emitter.

A small amount of heat is conducted from the microburner by the support tubes according to Fourier's Law,

$$Q_{cond} = \frac{k_t A_t (T_b - T_a)}{L_t} \tag{2.10}$$

where k_t is the thermal conductivity of the tube material, A_t is the total cross sectional area of all tubes, and L_t is the length. This mechanism is relatively unimportant because of the high L_t/A_t ratio for the tubes. A small amount of heat is also radiated from the tubes but we did not include this loss mechanism in the model.

The heat loss mechanisms discusses above are used in a heat balance equation

$$Q_{comb} = Q_{exh} + Q_{emit} + Q_{side} + Q_{cond} \tag{2.11}$$

where Q_{emit} is provided by the optical model. The thermal and optical models are solved self-consistently for the microburner temperature and the spectrum incident on the TPV cell.

2.2 Optical model

The optical cavity model calculates the net heat flux radiated by the emitter and the spectrum incident on the TPV cell. We assume purely diffuse emission and reflection such that radiative transfer between components is governed by the view factor F. We used detailed balance to calculate the flux into (q_{mi}) and out of (q_{mo}) each component m (emitter or cells) for every wavelength, as shown in Fig. 2-3a. The detailed balance model is a statement of conservation of energy and linearity: at every wavelength, the flux leaving a surface is the sum of reflection off the surface and the thermal emission from the surface. If component m has reflectivity and emissivity of ρ_m and ε_m, respectively, the detailed balance equations for the emitter-cell system are

$$q_{eo} - \rho_e q_{ei} = \varepsilon_e e_b(\lambda, T_b) \tag{2.12}$$

$$q_{co} - \rho_c q_{ci} = 0 \tag{2.13}$$

where the first equation is for the emitter and the second equation is for the cells. The left hand side refers to radiation already in the cavity and the right hand side refers to thermal

emission. The detailed balance equations can be put in matrix form

$$\begin{bmatrix} 1 & -\rho_e F \\ -\rho_c F & 1 \end{bmatrix} \begin{bmatrix} q_{eo} \\ q_{co} \end{bmatrix} = \begin{bmatrix} \varepsilon_e e_b(\lambda, T_b) \\ 0 \end{bmatrix} \tag{2.14}$$

and solved

$$q_{eo} = \frac{1}{1 - F^2 \rho_c \rho_e} \varepsilon_e e_b(\lambda, T_b) \tag{2.15}$$

$$q_{co} = \frac{F \rho_c}{1 - F^2 \rho_c \rho_e} \varepsilon_e e_b(\lambda, T_b). \tag{2.16}$$

The quantities of interest are the net flux out of the emitter ($q_{eo} - q_{ei}$) and the spectrum incident on the cell $q_{ci} = F q_{eo}$:

$$q_{eo} - q_{ei} = \frac{1 - F^2 \rho_c}{1 - F^2 \rho_c \rho_e} \varepsilon_e e_b(\lambda, T_b) \tag{2.17}$$

$$q_{ci} = \frac{F}{1 - F^2 \rho_c \rho_e} \varepsilon_e e_b(\lambda, T_b). \tag{2.18}$$

These equations are correct in the limiting cases ($\rho_c = 0$, $\rho_e = 0$, etc.) and match what can be derived through a geometric series method. From Fig. 2-3a, we can write down q_{ci} as

$$q_{ci} = \sum_{n=0}^{\infty} \varepsilon_e F (\rho_c F \rho_e F)^n e_b(\lambda, T_b) \tag{2.19}$$

because the thermal radiation incident on the cell is emitted from the emitter (ε_e), transported across the vacuum gap (F), and can make n round trips across the cavity $(\rho_c F \rho_e F)^n$. The geometric series can be summed to find the same result as Equation 2.18. A similar approach can be used to verify Equation 2.17.

The view factor is simply defined as the fraction of radiated power leaving one component that reaches another. Let F be the view factor between the emitter and the filter. Although the actual components are rectangular, the view factor is well approximated by two coaxial

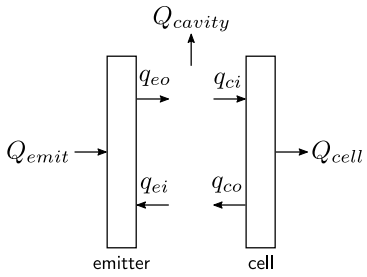

(a) Optical cavity.

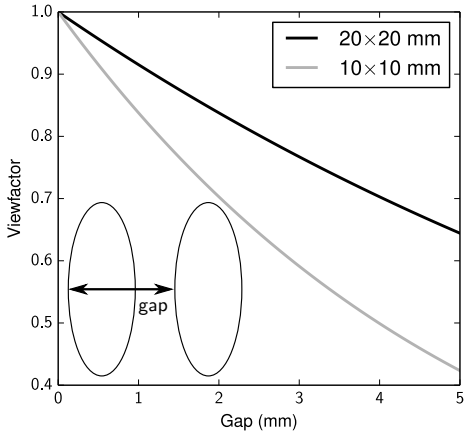

(b) View factor.

Figure 2-3: A block diagram of the optical cavity comprised of the emitter and cell, with total heat fluxes as Q and wavelength dependent heat fluxes as q. The view factor governs radiative transfer between the emitter and cell.

disks of equal area which is given analytically by

$$F = \frac{1}{2}\left[X - \sqrt{X^2 - 4\left(\frac{R_2}{R_1}\right)^2}\right] \tag{2.20}$$

$$X = 1 + \left(\frac{1+R_2}{R_1}\right)^2 \tag{2.21}$$

$$R_i = r_i/d \tag{2.22}$$

where r_i is the radius of disk i (representing either the emitter or cells) and d is the distance between them [40]. The emitter-cell view factor for the systems we built is given in Fig. 2-3b. It is clear that the microburner and cells need to be very close, less than 1 mm, to achieve good radiative transfer.

2.3 Electrical model

The electrical model converts the optical spectrum incident on the cell into electrical power output. It can be divided into two parts: the first converts incident photons into photocurrent using quantum efficiency (QE) and the second converts the photocurrent into a current-voltage (IV) curve using a circuit model from which the electrical power output can

easily be found.

Quantum efficiency is the ratio of photocurrent in electron charges to incident photon flux. By this definition the photocurrent is

$$I_{ph} = e \int_0^\infty \frac{\lambda}{hc} q_{ci}(\lambda) \mathrm{EQE}(\lambda) d\lambda, \tag{2.23}$$

where $q_{ci}(\lambda)$ is the radiated power per unit wavelength incident on the cell, hc/λ is the photon energy, EQE is the external quantum efficiency from Fig. 2-4a and e is the electron charge. The photocurrent becomes a parameter in an equivalent circuit model in order to find the electrical power output.

The equivalent circuit for an externally illuminated photovoltaic cell consists of a current source representing the generated photocurrent and a diode with parasitic series and shunt resistances shown in the inset of Fig. 2-4b. If the photocurrent and all other component values are known then the terminal IV relationship is

$$I = I_{ph} - I_0 \left(\exp \left[\frac{q}{n k_B T_j} (V + I R_s) \right] - 1 \right) - \frac{V + I R_s}{R_{sh}}, \tag{2.24}$$

where I and V are the terminal current and voltage, $q/k_B T_j$ is the thermal voltage, I_{ph} is the photocurrent, I_0 is the diode dark current, n is the diode ideality factor, and R_s and R_{sh} are the shunt and series resistances [41–43]. The equivalent circuit parameters are given in Appendix E and were extracted from experimental data. The experimental data and a the IV curve fit using the equivalent circuit model are shown in Fig. 2-4b. The reported electrical power output was taken at the maximum power point.

2.4 Predictions

The three domains were linked to form a complete system model. First, the microburner heat balance and optical cavity models were solved self consistently. The microburner temperature had to equal the emitter temperature and the net power into the emitter had to satisfy the microburner heat balance. These two cannot be decoupled because a change in the optical cavity will change the microburner's heat balance which in turn will change the

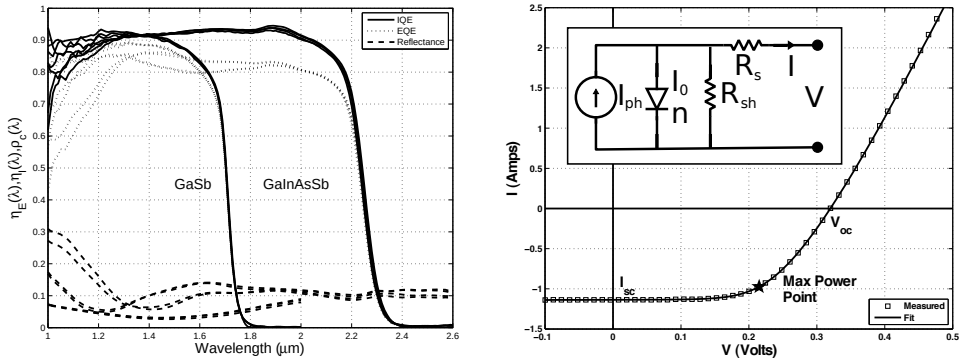

(a) Quantum efficiency and reflectivity. (b) IV curve.

Figure 2-4: Quantum efficiency and reflectance (a) of GaSb and InGaAsSb cells and a single IV curve of a InGaAsSb cell (b) with the equivalent circuit model inset.

radiated power. The microburner temperature is a byproduct of this calculation. Second, the photocurrent was calculated with the quantum efficiency. Finally, the equivalent circuit was calculated from the cell's operating point. The full IV curve was calculated by solving the diode equation. The IV curve yielded the electrical power output, completing the full fuel to electricity model.

We did several simulations with a step function emitter with a constant in-band emissivity of ε_{in} and out-of-band emissivity of ε_{out},

$$\varepsilon_e = \begin{cases} \varepsilon_{in} & \lambda < \lambda_g \\ \varepsilon_{out} & \lambda > \lambda_g \end{cases} \tag{2.25}$$

with a cutoff at the cell's bandgap λ_g. We assumed a microburner with side area occupying 30% of the total area, InGaAsSb cells, and a view factor of $F = 0.9$. These values are similar to those of the experimental systems.

Our first set of simulations focused on understanding the effect of emitter emissivity and side emissivity. We conducted three simulations with a constant $\varepsilon_{in}/\varepsilon_{out} = 2$ but varying values of ε_{in} for two values of side emissivity ε_s. As seen in Fig. 2-5a, with no side losses the exact values of the in-band and out-of-band emissivities do not greatly affect the electrical output, only the ratio does. The efficiency is slightly higher for the low emissivity emitter because it increases the temperature which shifts the blackbody into the convertible region.

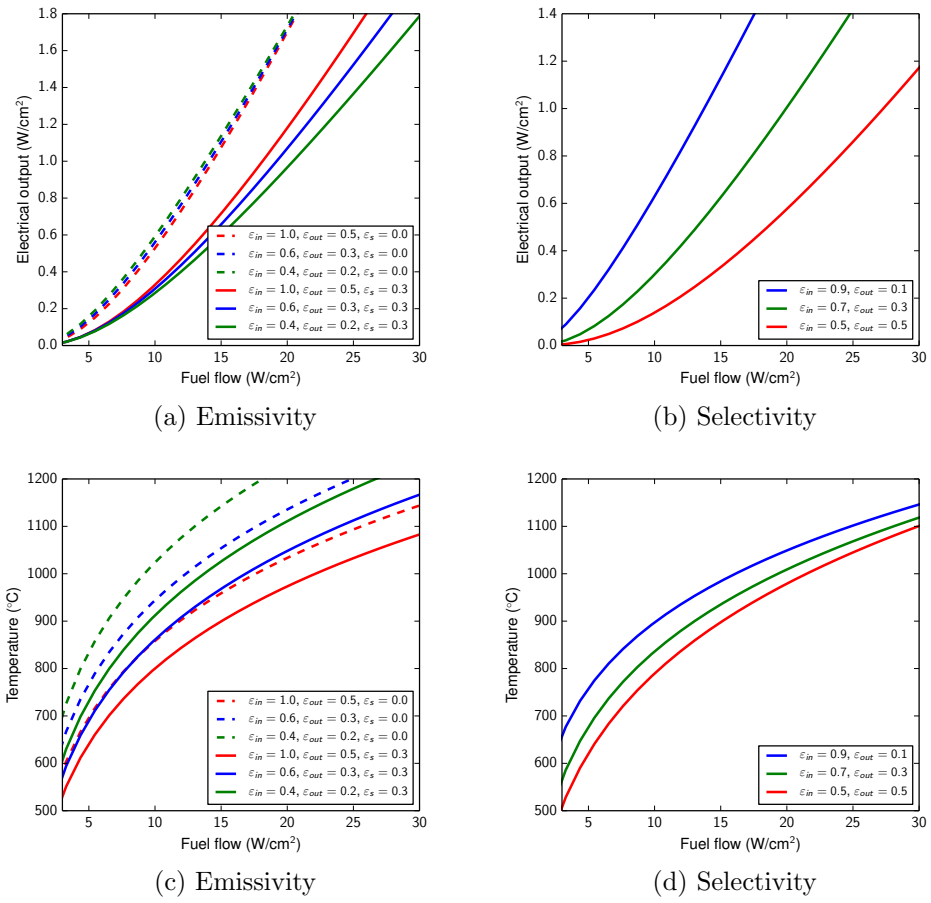

(a) Emissivity (b) Selectivity

(c) Emissivity (d) Selectivity

Figure 2-5: Model predictions for TPV systems with (a, c) varying emitter and side emissivities and (b, d) emitter selectivities.

In the case of non-zero side emissivity, the exact value of the in-band and out-of-band emissivities greatly affects electrical power output. A higher efficiency is achieved for the high emissivity emitter which is able to radiate a larger share of the fuel's energy content than is lost to side radiation.

We also studied the effect of emitter selectivity $\varepsilon_{in}/(\varepsilon_{in} + \varepsilon_{out}) = 0.5$–$0.9$ on electrical power output. Note that our present definition of selectivity differs from spectral efficiency which is the ratio of radiated power not emissivity. We assumed the sides had the same emissivity as the emitter. Higher selectivity had the obvious effect of increasing electrical output for a given input power. Temperature remained relatively constant because increasing selectivity only shifts power from the unconvertible region to the convertible region—there

is only a slight change in total radiated power and hence the heat balance caused by the asymmetry of the blackbody curve with respect to λ_g.

Chapter 3

Generation I: Silicon System

The silicon system was built around a silicon MEMS microburner: a 10×10 mm chip with an internal serpentine channel defined by photolithography and etching. Propane and oxygen were flowed through the channel and reacted on the catalyst-coated walls to generate heat. The heat was then conducted through the silicon to the Si/SiO_2 emitters deposited directly on the front and back surfaces, which radiated the heat to the TPV cells. The silicon system is shown in Fig. 3-1. Initially, silicon seemed to be the ideal material for a TPV system: (1) it has good high temperature oxidation resistance which is important for the interior of the channels and enables operation in air, (2) we could leverage well developed MEMS fabrication techniques, (3) a Si/SiO_2 multilayer selective emitter could be directly deposited on the microburner, and (4) initial work had already been undertaken on a microburner that was believed to fit our needs [16, 44, 45].

In this chapter, we made many improvement to the microburner described in Ref. 44 and integrated it into a TPV system. We designed a multilayer stack to suppress out-of-band radiation and deposited it directly on the microburners. The Si/SiO_2 selective emitter doubled the fuel-to-electricity conversion efficiency compared to bare silicon. Despite these promising results, we found that silicon platform was fundamentally limited by a thermal expansion mismatch.

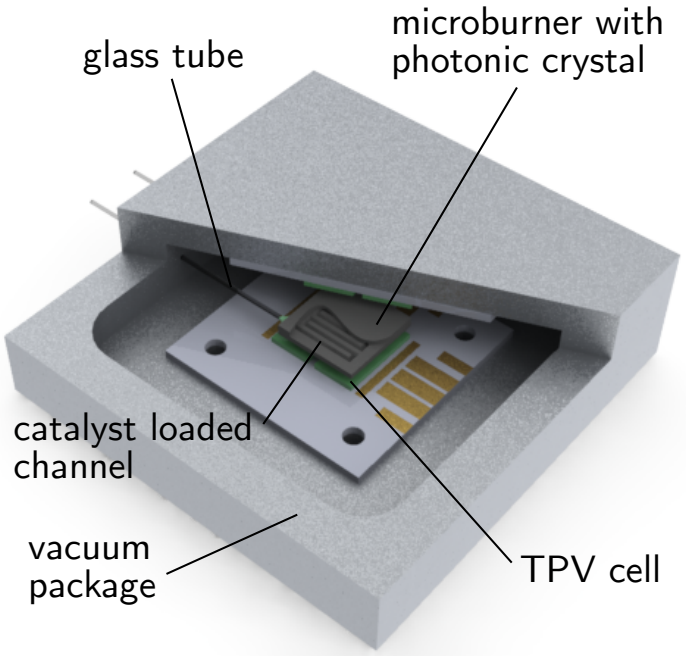

Figure 3-1: Silicon TPV system concept. Propane and oxygen react in a catalyst-coated channel in a silicon MEMS microburner and heat a Si/SiO_2 emitter to incandescence. The radiation is incident on InGaAsSb TPV cells and converted into electricity. The glass capillary tubes double as both mechanical supports and fluidic connections to minimize heat loss. They are bonded to the microburner with glass solder and the vacuum package with a polymer adhesive.

3.1 Microburner fabrication and characterization

The silicon microburner fabrication and packaging process is described briefly below:

1. The silicon microburner was fabricated according to the process given in Ref. 44 involving photolithography and KOH etching with a SiN hard mask to define the serpentine channel followed by wafer bonding. Fabrication was performed by Mohammad Araghchini [46]. A five-layer Si/SiO_2 stack was deposited on one set of wafers by plasma enhanced chemical vapor deposition (PECVD) and low pressure chemical vapor deposition (LPCVD) and the other wafer was left bare.

2. A diced microburner was loaded with an alumina supported platinum catalyst by washcoating with a suspension of catalyst particles in a solution of nitrocellulose binder in an organic solvent as described in Appendix A.

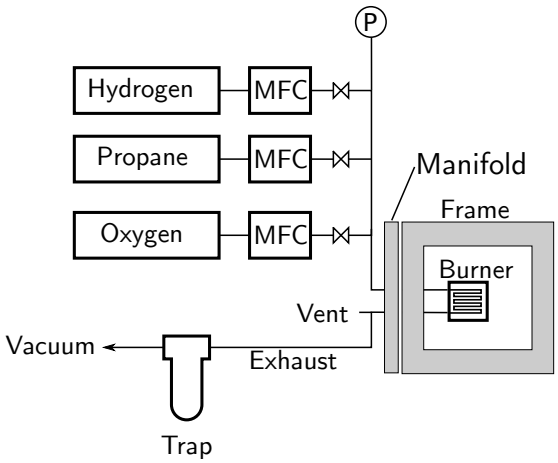

Figure 3-2: Block diagram of the fuel and exhaust systems. "P" indicated a pressure gauge and "MFC" indicates a mass flow controller.

3. Two borosilicate glass tubes that served as both mechanical supports and fluidic connections to minimize heat loss were attached to the microburner by glass soldering. A paste of powdered, coefficient of thermal expansion (CTE) matched PbO-ZnO-B_2O_3 glass (Sem-Com SCC-7) and a nitrocellulose binder in an organic solvent was applied to the joint while held in a jig. The assembly underwent a heat treatment to ~700°C to sinter then devitrify the solder glass to form a tough glass-ceramic composite. The process is given in Appendix B.

4. The microburner's tubes were bonded into holes in a metal frame with a hot-melt polyimide adhesive. The frame allowed connections to be made to the glass tubes, easy handling of the fragile microburner, and would serve as part of the vacuum chamber in later experiments.

The microburner was characterized on its own before being integrated into a TPV system. The primary goal of this characterization was to validate our thermal model (Chapter 2) by matching fuel flow to temperature. A second goal was to become familiar with the operation of the microburner without any danger of damaging the TPV cells. Tests were conducted with the microburner in air then in vacuum to prevent convective heat loss. The experimental setup needed for vacuum was significantly more complicated and was essentially that described in the next section with the cells removed.

The experimental apparatus surrounding the microburner is shown in Fig. 3-2. Three MKS mass flow controllers (MFCs) were used to meter the fuel and oxygen flows. The outputs of all the MFCs were tied together at the inlet manifold and were piped to the microburner. Fuel and oxygen were delivered to the microburner premixed. To prevent flashback, the entire inlet manifold was plumbed in 1/16 inch stainless steel capillary tubing, and as a result we never observed a flame propagating further than the glass capillary tubes even with hydrogen-oxygen. The inlet and outlet connection were made to the microburner by o-ring seals to the edge of the frame. At the exhaust connection, an airflow of 3–4 liters per minute was established between a small vent hole and the laboratory vacuum in order to prevent condensed water from accumulating and clogging the glass capillary tube. The vent maintained the outlet near atmospheric pressure.

When operating with hydrogen, the microburner could be lit by merely flowing the two reactants at room temperature. The hydrogen and oxygen flows were increased gradually, maintaining the equivalence ratio, and the temperature was recorded. An Optris G5L infrared thermometer sensitive to 5 µm thermal radiation was employed to make non-contact measurements of the microburner's temperature. Infrared thermometry was favored over thermocouples because even fine-gauge thermocouples significantly alter the temperature [44] and require electrical feedthroughs when operating in vacuum. The Optris was calibrated to correct for the temperature-dependent emissivity of silicon with OmegaLaq temperature indicating lacquer. A sufficient range of lacquer formulations was available to calibrate nearly the entire temperature range. Microburner temperature as a function of fuel input for hydrogen-oxygen is shown in Fig. 3-3a.

With hydrogen, homogeneous combustion proved to be a problem at high temperatures and flow rates. The mixture would flashback into the glass capillary resulting in a catastrophic failure. Flashback could be mitigated by moving to higher oxygen flow rates. High temperatures could only be achieved with $\phi = 6$, leading to inefficient operation and excessively high flow rates.

For propane and butane, the microburner had to be preheated to about 300°C by co-feeding a small amount of hydrogen until autothermal operation was achieved at which point the hydrogen was shut off. Butane proved to be much more stable than hydrogen.

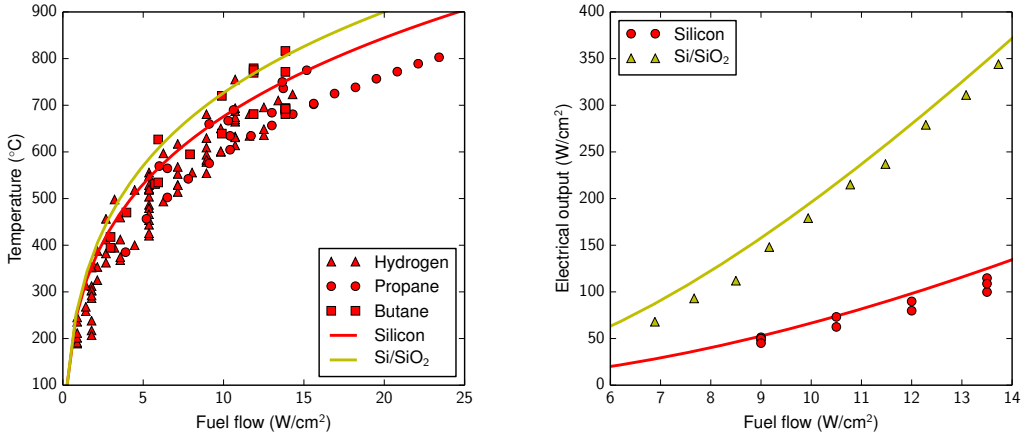

(a) Temperature.

(b) Electrical power.

Figure 3-3: Measured (points) and simulated (lines) performance of the silicon microburner. Temperature measurements were made for a variety of fuels and conditions for the bare silicon microburner. No temperature measurements were made on the Si/SiO_2 microburner. Simulated temperatures for different fuels are overlapping.

Homogeneous combustion was never observed with $\phi = 1.5$ due to butane's lower flammability. One of the difficulties encountered during system testing was that the microburner experiences occasional temperature fluctuations due to condensed butane entering the fuel supply. Butane was delivered to the microburner as a gas but occasional droplets, representing additional fuel, entered the inlet stream resulting in a sudden increase in temperature. Propane was the most stable fuel tested: no flashback was observed for $\phi = 1.0$–1.5 and its higher vapor pressure ($\sim$10 atm) compared to butane ($\sim$1 atm) prevented condensation. The temperature data are presented in Fig. 3-3a for hydrogen, butane, and propane. The graph contains measurements made in air and in vacuum, and at varying vacuum levels, and at various equivalence ratios in the case of hydrogen. Note that the plot is given as a function of input power not fuel flow. Overall, we achieved good agreement between the simulation and experiment.

3.2 TPV experiment

Next, the silicon microburner was integrated with the TPV cells. The experimental challenge was design of an experimental apparatus to establish a small $\sim$1 mm vacuum gap

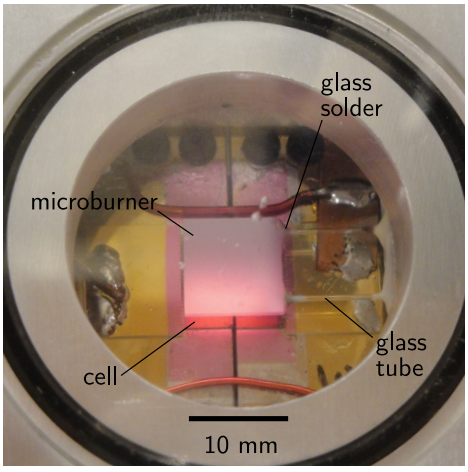

(a) Microburner in operation.

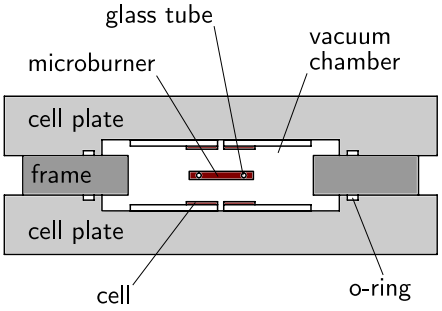

(b) Cross section.

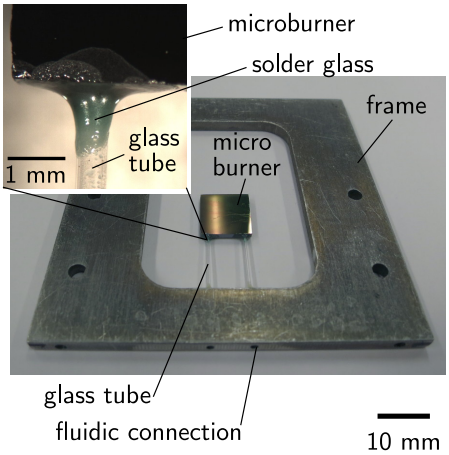

(c) Microburner frame.

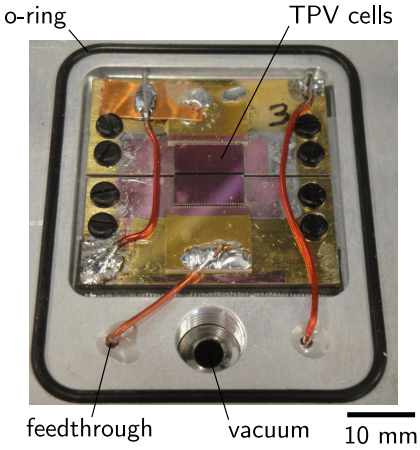

(d) Cell plate.

Figure 3-4: The silicon TPV experimental setup.

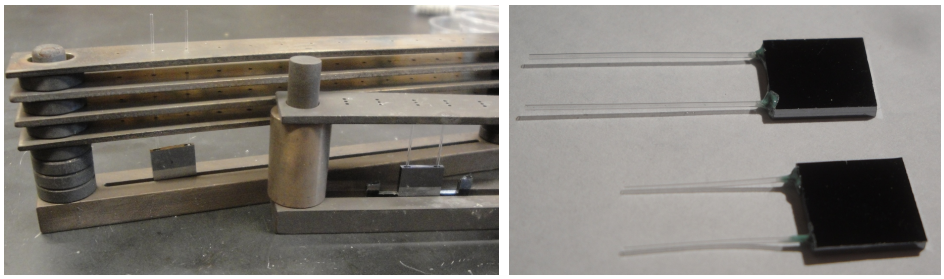

(a) Glass brazing jig. (b) Microburners with attached tubes.

Figure 3-5: The new (back) and old (front) jigs used for solder glass application and firing, and microburners soldered in their respective jigs. Additional supports in the new jig prevented the glass tubes from deforming.

between the microburner and the cells and axial alignment between the components. Furthermore, apparatus was to be compact, without any large vacuum chambers or positioning stages, to simplify the transition to a standalone microgenerator. We designed the modular experimental setup shown in Fig. 3-4 which was comprised of three-layer stack: (bottom) cell plate, (middle) microburner frame, and (top) either a window plate with a CaF window or a second cell plate. The cell plates had two packaged InGaAsSb cells and were water cooled. The microburner frame had a permanently packaged microburner. The three layers were sealed with o-rings to form the vacuum chamber which was evacuated to 30 mTorr with a mechanical vacuum pump. The gap between the microburner and cells was set by the thickness of the microburner frame, which could be varied.

The thickness of the microburner plate was limited by the straightness of the glass support tubes. The 0.550 mm outside diameter borosilicate tubes (Vitrocom) deformed during the glass soldering process because the required temperature near 700°C exceeded the $T_g = 520$°C glass transition temperature at which deformation becomes possible. We designed an improved glass soldering jig (Fig. 3-5) that prevented the tubes from deforming during the glass soldering process, allowing for tighter control of the microburner-to-cell distance and a better view factor. With this improvement, we decreased the thickness of the frame from 12.7 mm (0.5 in) to 4.7 mm (0.188 in), corresponding to an improvement in view factor from $F = 0.37$ to 0.84.

A second challenge we faced was mounting the glass soldered microburners in the frames. Initial work used a high-temperature epoxy (Aremcobond 526N) with limited success be-

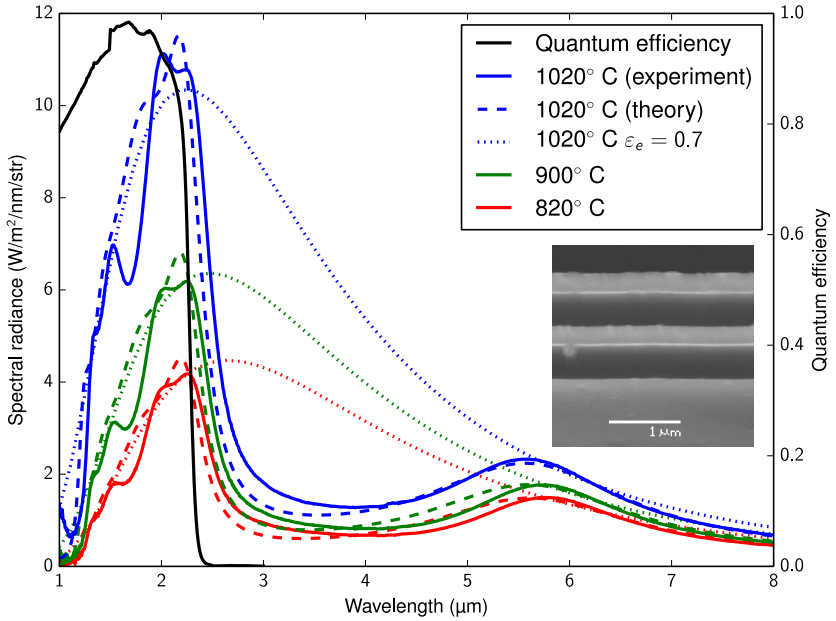

Figure 3-6: Measured and simulated emission spectrum for the Si/SiO_2 structure at 820, 900, and 1020°C. Inset: an SEM micrograph of the structure.

cause the heat from the exhaust gases degraded the epoxy causing a leak, and the resulting off-gas contaminated the cells. We switched to a high-temperature hot-melt polyimide adhesive (Imitec). Molten polyimide was flowed into the joint at 250°C and cross-linked at 350°C for one hour while the assembly was held in a jig to ensure proper alignment. Most epoxies were only stable to about 200–300°C while the polyimide was stable to 350–400°C. The polyimide seals suffered no visible degradation over the course of a typical run. We also found that it was important to make the seal over length of the mounting hole, rather than just with fillet on the surface.

Finally, a five-layer Si/SiO_2 stack was deposited directly on the microburner to serve as a selective emitter. The layer thicknesses were globally optimized using the product of efficiency and power density by Peter Bermel [38]. The stack was characterized room temperature reflectance and high temperature emissivity measurements. Room temperature reflectance was measured on an Optronics Laboratory OL750 spectrophotometer. High temperature emissivity measurements were performed on a Nicolet Nexus 870 FTIR using an

Emitter	Sides	Cells	View factor
Si	$\varepsilon_s = 0.7$	2× 5×10 mm InGaAsSb	$F = 0.59$ (3.0 mm gap)
Si/SiO_2	$\varepsilon_s = 0.7$	4× 5×10 mm InGaAsSb	$F = 0.84$ (1.0 mm gap)

Table 3.1: Summary of the TPV systems experimentally investigated. The gap is different between the two systems because we continued to make improvements to the glass soldering process.

external high vacuum heater apparatus and blackbody calibration described in Refs. 47, 48. The measured spectra are shown in Fig. 3-6. The Si/SiO_2 structure improved the spectral efficiency from 14% to 22% at 800°C and 25% to 35% at 1000°C versus bare silicon. The average (blackbody-weighted) in-band emissivity is $\varepsilon_{in} = 0.62$ and the average out-of-band emissivity is $\varepsilon_{out} = 0.36$ at 1000°C.

With these improvements in place, we ran the microburner with TPV cells. The two experimental systems, with and without the Si/SiO_2 selective emitter, are summarized in Table 3.1. The microburner was operated in the same manor as the previous section except the electrical power was recorded instead of the temperature. Robert Pilawa and Nathan Pallo designed a boost converter with maximum power point tracker (MPPT) which (1) provided real-time impedance matching between the TPV cell array and the electric load, and (2) boosted the 1 volt output of the array to 3.6 volts [49, 50]. When operating with the MPPT in place, the output power was simply the output voltage times the output current with a Keithley 2440 source meter as a constant voltage electronic load. When operating without the MPPT, the Keithley swept an IV curve of the entire array in the same fashion individual cells were characterized and the maximum power point was calculated. Electrical power measurements are reported in Fig. 3-3b.

The heat loss breakdown was calculated from the model in Table 3.2. The Si/SiO_2 emitter improve the spectral efficiency defined as the ratio of in-band power to total flux incident on the cell,

$$\eta_{spec} = \frac{Q_{iv} + Q_{elec}}{Q_{spec} + Q_{iv} + Q_{elec}}, \tag{3.1}$$

from $\eta_{spec} = 13\%$ for silicon to $\eta_{spec} = 29\%$. The observed increase in spectral efficiency was greater than the increase originally expected from analysis of the emission spectrum

Emitter	Temp.	Q_{exh}	Q_{cond}	Q_{side}	Q_{cavity}	Q_{spec}	Q_{iv}	Q_{elec}
Si ($F = 0.59$)	1027 K	13.3%	0.2%	24.7%	27.4%	30.0%	3.5%	1.0%
Si ($F = 0.77$)	1031 K	13.4%	0.2%	25.0%	11.3%	43.4%	5.1%	1.5%
Si/SiO_2	1123 K	15.3%	0.2%	35.3%	9.2%	28.6%	8.7%	2.7%
Step func.	1181 K	16.5%	0.2%	43.2%	7.6%	10.1%	17.1%	5.3%

Table 3.2: Heat loss analysis for the silicon system at 14 W of input power. All assume a view factor of $F = 0.77$ unless noted. The step function emitter has $\varepsilon_{in} = 0.9$, $\varepsilon_{out} = 0.1$, and $\varepsilon_s = 0.7$.

because the temperature increased. The Si/SiO_2 emitter improved the spectral efficiency by suppressing unconvertible radiation which had the consequence of proportionally increasing the heat loss from the sides of the microburner which remained bare silicon.

Preliminary work was undertaken to develop a low emissivity coating for the edges. The coating would need to withstand the glass brazing process at nearly 700°C in air, hence platinum was chosen for its high reflectance and oxidative stability. The reflectance of a metal film quickly degrades because the most metals readily reacted with the silicon substrate to form silicides [51]. Tantalum may have been a suitable because it forms a Ta_2O_5 diffusion barrier at the Ta-Si interface [52], except it could not survive the brazing process in air. We did not investigate further because limitation of the silicon microburner were becoming evident.

3.3 Limitations of the silicon microburner

We used a PbO-ZnO-B_2O_3 solder glass (Sem-Com SCC-7) expansion matched to silicon to seal the borosilicate tubes to the silicon microburner. During the firing cycle to ∼700°C, a crystalline phase precipitated (devitrification) to form a glass-ceramic composite that can nominally operate above the firing temperature [53]. We observed cracking of the solder glass joint on the inlet tube when the microburner was operated above ∼800°C. Blackwell confirmed that the solder glass limited the operating temperature to ∼900°C and to only 710°C for reliable operation despite two years of ad hoc investigation [44]. We conducted a more rigorous investigation into the solder glass.

We prepared micrographs of the solder glass on silicon after the sintering and devitrifying

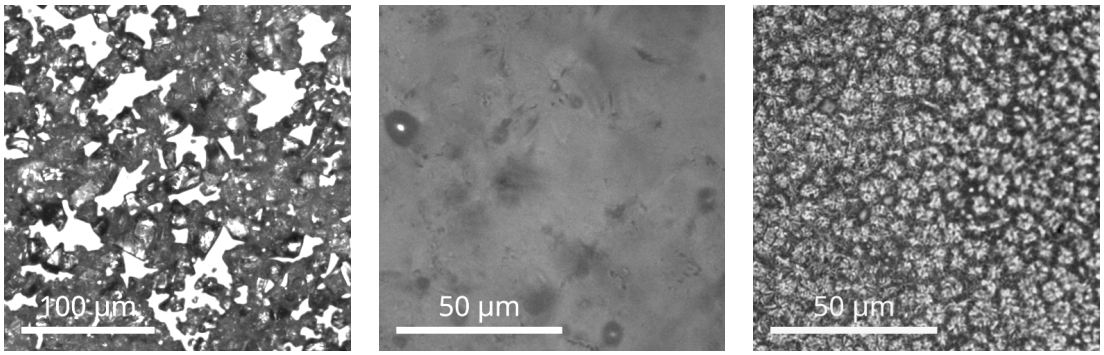

(a) Unfired (b) Sintered (c) Devitrified

Figure 3-7: Unfired, sintered, and devitrified solder glass, prepared by spin coating a dilute suspension on silicon. The unfired sample looked opaque green-white and had visible particles. The sintered sample was heated to 620°C for 1 hour and was translucent dark green with air bubbles. The devitrified sample was heated to 680°C for 1 hour and was opaque green-grey because the crystalline phase scattered light.

phases of the firing cycle in Fig. 3-7. We used differential scanning calorimetry (DSC) measurements (Fig. 3-8a) to understand firing cycle: the region around 550°C at point A is the glass transition, the small peak B at 620°C is the glass particles coalescing, and the large peak C at 740°C is devitrification [54]. Temperatures determined by DSC are typically higher than those used in the actual firing cycle because in the DSC we use a 10°C/min ramp whereas in the firing cycle we dwell at a lower temperature but for a longer duration.

The most critical factor in making a glass seal is matching the CTEs of all components. The CTEs should be matched within about $0.2 \times 10^{-6}\,\mathrm{K}^{-1}$ and a mismatch of 0.5 to $1.0 \times 10^{-6}\,\mathrm{K}^{-1}$ is considered the upper limit [55, 56]. At room temperature, both silicon and borosilicate glass have a CTE of $\sim 3 \times 10^{-6}\,\mathrm{K}^{-1}$. These numbers are commonly quoted but greatly oversimplify the problem. The CTEs of all material must match at room temperature, at the maximum temperature they are exposed to, and everywhere in between. The CTE of the sintered and devitrified glasses was measured as a function of temperature by thermomechanical analysis (TMA). The sintered sample was fired at 620°C for 1 hour; the devitrified sample was sintered at 620°C for an hour then devitrified at 680°C for another hour. Fig. 3-8b plots the total expansion of the solder glass (both sintered and devitrified) and silicon (from [57]) as a function of temperature. For the sintered sample, the change in thermal expansion at point D marks the glass transition. The hook at point E

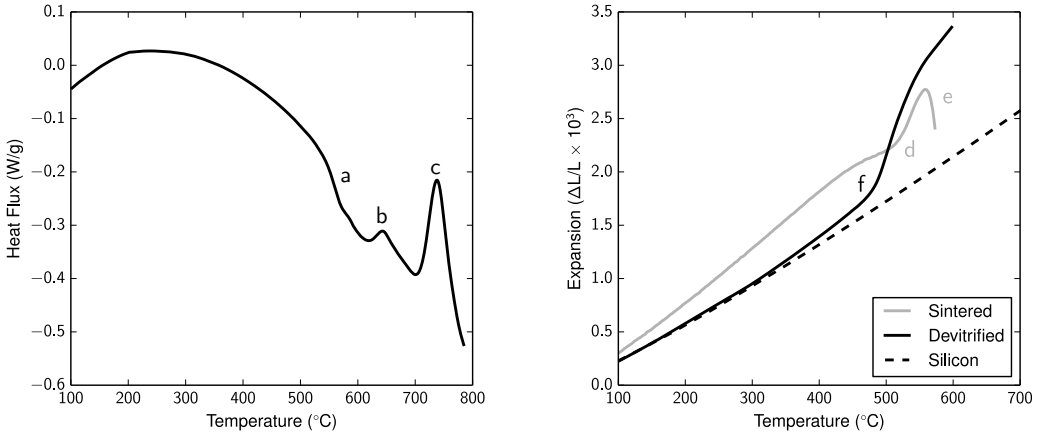

(a) DSC analysis.

(b) TMA analysis.

Figure 3-8: (a) DSC trace of SCC-7 solder glass at 10°C per minute. The glass transition (point a), sintering (b), and devitrification (c) are visible. (b) Thermal expansion of silicon and SCC-7 measured by TMA of samples were prepared by firing the glass in a graphite mold then grinding the ends flat and parallel. The glass transition (d, f) and melting (e) are visible.

is caused by the glass deforming. Devitrification reduces the CTE below the glass transition temperature to match that of silicon very well. Past the glass transition (point F) the rate of expansion increases, leading to cracked joints. The CTE mismatch at 500°C limits the maximum safe operating temperature which in turn limits efficiency and power density.

Given the limitations of the solder glass-silicon interface, we had several options:

- Fabricate the both the microburner and tubes entirely from silicon to eliminate the thermal expansion mismatch. The difficult low-yield fabrication process combined with the extremely delicate finished product [16, 45] was the original motivation for the glass tubes [44].

- Change tube materials, possibly to Kovar as used in the microturbine project, and use solder glass with a higher glass transition temperature [58]. This approach only expands the operating region because the solder glass has a glass transition temperature and silicon does not—there will be an expansion mismatch at some temperature.

- Move to a metallic material system that relieves stress through plastic deformation rather than brittle fracture. A metallic system also promises simplified fabrication

and improved mechanical robustness.

We chose the last option and we proposed, designed, and demonstrated a highly robust metallic TPV system built around an Inconel microburner.

Chapter 4

Generation II: Metallic System

The silicon system presented in Chapter 3 and its predecessors suffered from cracking due to the CTE mismatch between silicon and the solder glass at elevated temperatures. The problem could have been fixed by an improved solder glass formulation but our solution was a fully metallic platform which promised improved reliability and performance. The advantages are outlined below:

- **CTE matched.** The microburner and the tubes were made from a single material without the heterogeneous borosilicate-solder glass-silicon interface required in the previous work, thus eliminating thermal expansion mismatches.

- **Robust.** The metallic microburner was naturally more robust against thermal and mechanical shocks because metals tend to deform rather than crack under stress. It was able to withstand handling, fast thermal ramping, and homogeneous combustion. These characteristics facilitated experiments and will be critical for a portable microgenerator.

- **Easy fabrication.** The metallic microburner was fabricated with conventional machining and welding, both of which are fast, high yield, and relatively cheap. While microfabrication was able to leverage batch manufacturing, the ability to cheaply and reliably fabricate the few samples needed for an experiment proved valuable.

- **Fewer fabrication restrictions.** More designs are possible with machining than with microfabrication because we were no longer limited to the characteristic KOH-etched channel cross sections. As a result, the reaction zone could occupy a greater fraction of the total microburner volume and have a greater surface area, thus allowing a larger amount of fuel to be combusted.

- **Segregated inlet.** Because of the larger size of the metallic system, we were able to use a coaxial tube-in-tube segregated feed for the inlet where propane entered through the inner tube and oxygen through the annulus, thus preventing flashback and allowing the catalyst to be reloaded.

- **Improved emitter.** Metallic photonic crystals offer higher performance than the Si/SiO_2 stack used in the previous section. Although preliminary investigations have been undertaken on photonic crystal fabrication in thick sputtered tungsten on silicon [59] and titanium coated silicon microcavities [60], neither the long term stability of such coatings nor the stability of microstructures were evaluated. In the case of the metallic system, a metallic photonic crystal can be fabricated independently and integrated by welding or brazing or fabricated directly on a tantalum film sputtered on the microburner.

A comparison of the new metallic microburner with the old silicon microburner is presented in Fig. 4-1.

In this chapter, we first present the design and characterization of a bare Inconel microburner without TPV cells. The lessons learned were incorporated into an improved five-tube metallic microburner which was tested with TPV cells. Finally, we integrated a 2D tantalum photonic by electron beam welding. The integrated system did not have the desired efficiency due to unforeseen issues and we propose a solution.

4.1 Microburner design

Our initial goal was an initial demonstration of the Inconel microburner as a proof of concept of the new material system. We would use a serpentine catalyst-loaded channel design

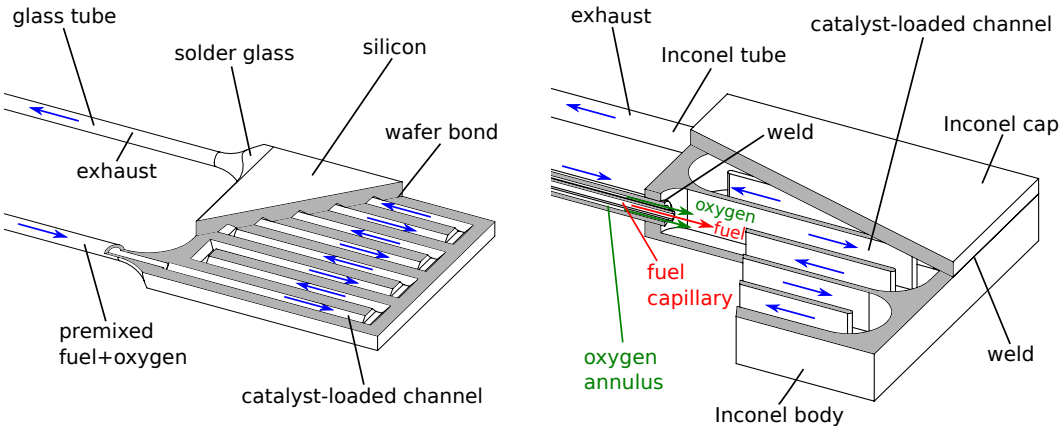

(a) 10×10 mm silicon microburner. (b) 20×20 mm metallic microburner.

Figure 4-1: Schematics of the silicon and metallic microburners.

because (1) its predecessor used the same design, (2) the catalyst lowers the temperature necessary to prevent quenching at the walls making the microburner easier to design and implement, and (3) catalytic combustion is a surface effect which uses the high surface area to volume ratio of a microburner to our advantage [61]. Complete reactant mixing and combustion cannot be assumed given the small size of the microburner and resulting short residence time. Thus, we used a simple model to determine the channel dimensions required for complete combustion.

Our microburners are sufficiently large compared to the molecular scale of combustion that same physics applies, albeit in a different regime than their conventional counterparts. We modeled catalytic combustion is a two step process [44]:

1. **Diffusion (τ_d).** The fuel is transported by diffusion to a catalyst site on the channel wall. Because of the size of the channel, flow is laminar and mass transport occurs primarily my molecular diffusion. The diffusion time is given by

$$\tau_d = \frac{D_h^2}{4D} \tag{4.1}$$

where d_h is the hydraulic diameter of the channel ($D_h = 4A/P$ where A is the cross sectional area and P is the wetted perimeter of the cross section) and D is the fuel's diffusivity.

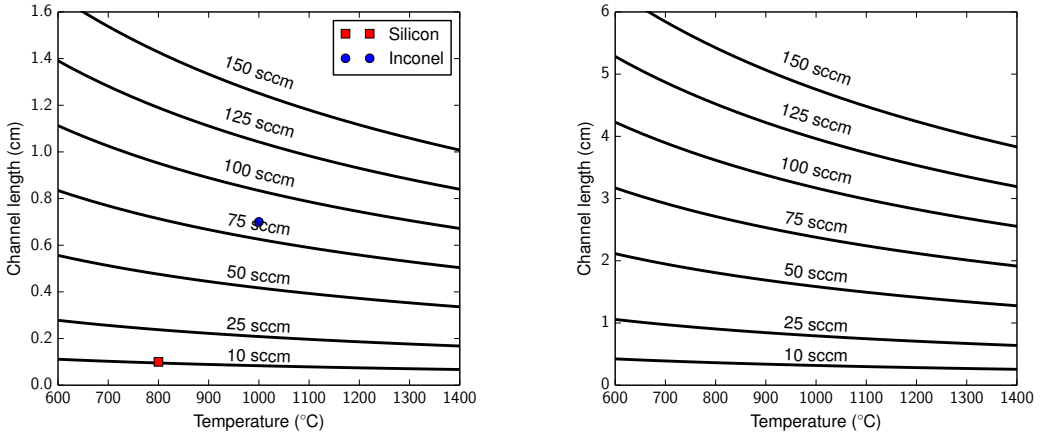

(a) Oxygen (b) Air

Figure 4-2: Minimum channel length to fully react ($\tau_d = \tau_r$) a propane flow with either oxygen or air with an equivalence ratio $\phi = 1.5$ as a function of temperature. Typical operating points for the silicon and metallic microburners are indicated.

2. **Reaction (τ_x).** The fuel reacts with oxygen at the catalyst site, and the rate of reaction is accelerated by temperature. Finding the reaction time constant, either numerically or experimentally, is beyond the scope of this work.

For our microburner with high temperature operation and moderate wall thermal conductivity, the diffusion time is greater than the reaction time and hence the process is diffusion-limited [62]. Even in the case where $\tau_d \approx \tau_x$, this simple model is still useful because the diffusion time is trivial to calculate.

We assume complete combustion if $\tau_r \gg \tau_d$, thus, though a simple analysis of the timescales of the system we were able to determine the required length of channel for complete combustion. The residence time is given by

$$\tau_r = \frac{LD_h^2}{\dot{V}} \tag{4.2}$$

where L is the length and D_h is the hydraulic diameter of the channel, and $\dot{V}$ is the total volumetric flow rate. We calculated the length for $\tau_r = \tau_d$ taking into account both the volumetric expansion and the temperature-dependent diffusivity [63] and plotted the minimum length in Fig. 4-2. Note that this quantity does not depend on the diameter—

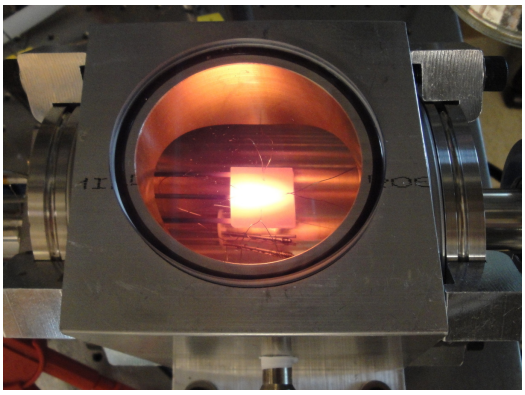

(a) Photograph.

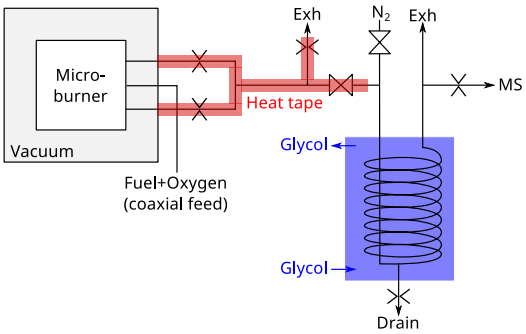

(b) Schematic.

Figure 4-3: The experimental apparatus used to characterize the microburner.

increasing the diameter increases both the diffusion time and the residence time. Typical operating points for both the silicon and Inconel microburners are plotted. Both fall into the complete combustion regime: in the case of silicon only a few millimeters of channel are required but the length is nearly 8 cm, in the case of Inconel less than 1 cm is required but the actual length is close to 14 cm. In the case of Inconel, we experimentally verified we were achieving complete combustion.

4.2 Microburner fabrication and characterization

The microburner was fabricated as described below:

1. A top and bottom half were machined from Inconel 600 according to the drawings in Appendix C.

2. First the tubes were attached then the two halves were joined by electron beam welding.

3. The microburner was mounted in stainless steel a frame by silver soldering or electron beam welding.

4. The catalyst was loaded with the same procedure used for the silicon microburner described in Appendix A.

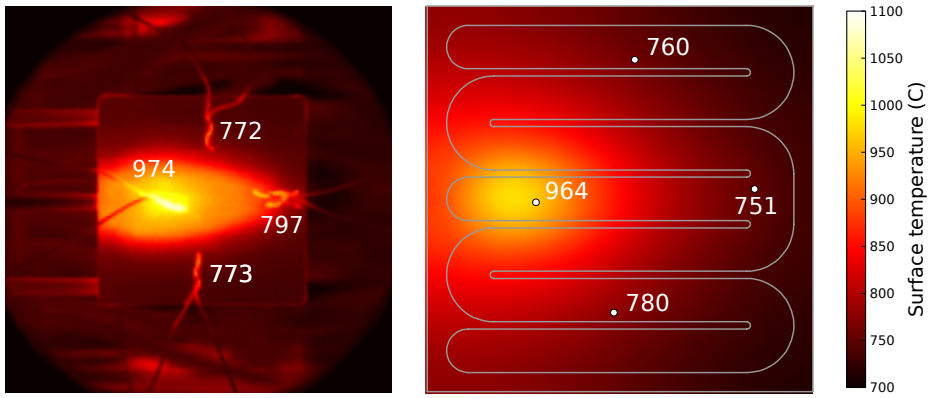

(a) Thermal image (b) CFD simulation result

Figure 4-4: A thermal image (a) and CFD simulation result (b) for the microburner operating at $Q_{comb} = 60$ W and $\phi = 1.5$.

The finished microburner was mounted the vacuum chamber shown in Fig. 4-3a to prevent convective heat loss and was plumbed as shown in Fig. 4-3b. Fuel and oxygen were metered by two mass flow controllers and delivered coaxially to the microburner through the central inlet tube. Each outer outlet tube was plumbed to an orifice before being combined to ensured equal flow distribution between the two halves of the microburner. The exhaust lines, especially the orifices, were heated to 120°C to prevent condensation.

The exhaust was passed through a condenser built from coiled copper tubing immersed in a recirculated glycol bath chilled to 0°C to remove water vapor. The condenser was filled with stainless steel ball bearings to minimize volume, both to improve response time and to prevent the buildup of a potentially flammable gas mixture during startup and shutdown. The outlet of the condenser was sniffed by a Pfeiffer GSD 301 mass spectrometer (MS). Exhaust composition was found using a least-squares method to fit a combination of NIST mass spectra and our own calibrations to the raw data.

An automated de-watering system was devised to allow for long, unattended runs. A timer actuated solenoid valves for one minute every hour. During the de-watering sequence, a valve opened to allow 100 psi nitrogen to blow accumulated water out a drain at the bottom of the condenser. Another valve was closed to protect the microburner from the resulting excursion while and temporarily diverted through a pressure relief valve.

Thermal instrumentation consisted of four K-type thermocouples and a FLIR SC660 thermal imaging camera. The thermocouples were spot welded to the body of the mi-

croburner and are visible in Fig. 4-4(a). The thermal imaging camera looked through a NaCl window at the microburner. The thermal images were calibrated from thermocouple readings.

To ignite the microburner, it was heated to approximately 400°C with a halogen lamp. Above that temperature, the propane kinetics over the catalyst were sufficient for autothermal operation, and the halogen lamp was shut off. Hydrogen assisted combustion could have also been used for ignition.

Steady state temperature versus total propane flow was measured by increasing propane flow in increments from 30 to 60 standard cubic centimeters per minute (sccm), corresponding to a total latent heat input of $Q_{comb} = 60$–91 W, while maintaining an oxygen flow of 7.5 times that of propane (an equivalence ratio of $\phi = 1.5$). Surface temperatures were allowed to stabilize at each set of flow conditions, typically 5 to 10 minutes. Flow rates were then decreased to 30 sccm propane to investigate possible hysteresis. Experimental data is presented in Figure 4-5.

At a constant propane feed of 40 sccm, the equivalence ratio was varied between $\phi = 1$–2 by a similar process. For all equivalence ratios $\phi \geq 1.25$, only carbon dioxide and unreacted oxygen were present in the exhaust, indicating complete combustion.

Initially, the analytical model described in Chapter 2 was used to predict microburner temperature, assuming $\varepsilon_e = \varepsilon_s = 0.5$. The analytical model accurately captures the trend versus propane flow in Fig. 4-5 but obviously cannot predict the observed 200°C temperature distribution. A uniform temperature is important for efficient operation of the TPV cells and reactor robustness.

In order to model the temperature distribution, Ben Wilhite conducted a computational fluid dynamics (CFD) simulation of the microburner in COMSOL using the Chemical Engineering Module and a combination of weakly compressible flow, convection and conduction and Maxwell-Stefan multicomponent diffusion physics packages [64]. The homogeneous combustion of propane was described using a single-expression kinetic model [65]. Gas-phase dynamic viscosity, thermal conductivity, heat capacity, and diffusivity were calculated according to the methods in Ref. 66–68 from literature data. Inlet flow was assumed to have a uniform velocity across the channel cross-section, have a uniform temperature

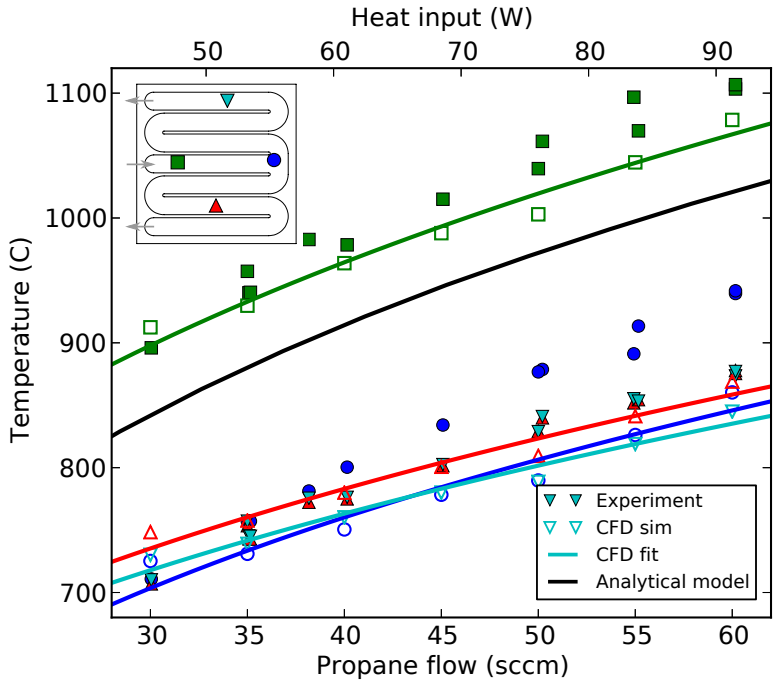

Figure 4-5: Steady state temperatures as a function of propane flow with $\phi = 1.5$. Individual CFD simulations do not fall exactly on a smooth curve because of the mesh size used.

of ambient, and consist of uniformly premixed propane and oxygen with no tube-in-tube segregated feed to facilitate convergence. Outlet boundary conditions assumed constant pressure of 1 bar and were open to convective heat and mass transport. A combination of no-slip, no mass flux (impermeable wall) and continuity of heat flux boundary conditions were used to describe fluid-wall interfaces. Radiative heat losses from all external surfaces of the solid-phase were described using a simple Stefan-Boltzmann expression assuming an emissivity of $\varepsilon = 0.5$ for all surfaces. Finite-element meshes consisted of approximately 10^5 individual elements, corresponding to 10^6 degrees of freedom. Typical solution times were an hour.

Simulation predictions of burner surface temperature at $Q_{comb} = 60$ W and $\phi = 1.5$ are presented alongside thermal images obtained experimentally in Fig. 4-4. A summary of measured and simulated thermocouple temperatures over the span of propane flow rates studied is presented in Fig. 4-5, alongside the analytical model. Simulations predict a more symmetric and focused hot-spot than experimentally observed; this is attributed to a combination of (i) assumption of pre-mixed fuel and oxidant leading to a pre-mixed flame shape,

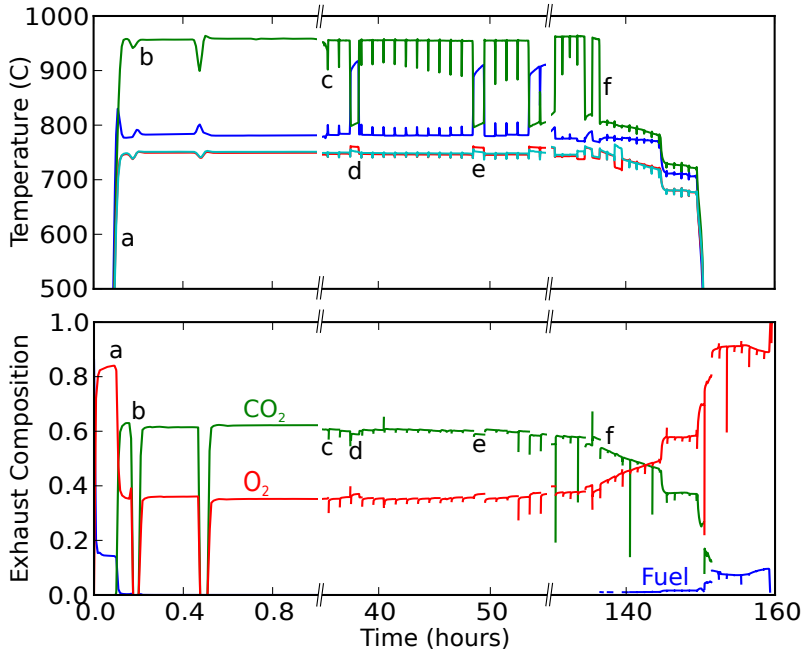

Figure 4-6: Temperature (top) and exhaust composition (bottom) of the long term study of the microburner running at $Q_{comb} = 60$ W and $\phi = 1.5$. The labeled points are described in the text.

as opposed to a diffusion-flame shape expected with segregated feed, and (ii) known limitations of the single-expression kinetic model for accurately predicting flame location [69]. Even with these assumptions, we obtained a good overall temperature agreement.

Once the above data was obtained, we conducted a long term study summarized in Fig. 4-6. The microburner was ignited at $Q_{comb} = 60$ W and $\phi = 1.5$ (point a). The periodic dips in temperature and MS data (points b and c) are caused by the periodic de-watering of the condenser. The occasional changes in steady state temperature (point d and e) are due to a transition between homogeneous and catalytic combustion. The MS data begins to indicate incomplete combustion around 135 hours (point f), indicated by reduction in CO_2 signal and increased O_2 and propane signals.

As noted above, two distinct operating regimes were observed within the microburner, corresponding to homogeneous and catalytic combustion which are shown in Fig. 4-7. In the homogeneous regime, a stable flame is present near the reactor inlet, as evidenced by the presence of an intense hot-spot located at the reactor inlet. In contrast, the catalytic

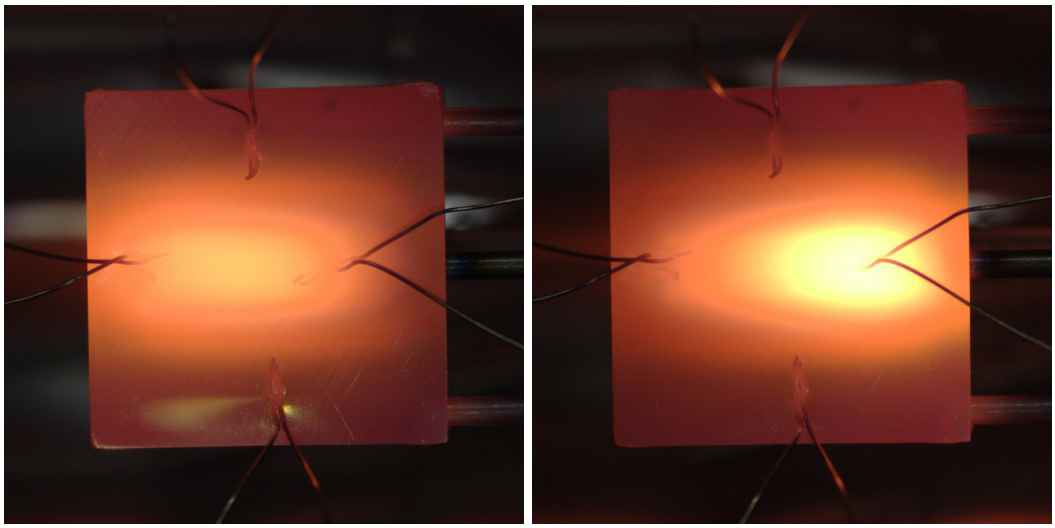

(a) Catalytic combustion (b) Homogeneous combustion

Figure 4-7: Catalytic and homogeneous modes of combustion. Homogeneous combustion has a more concentrated hot spot located closer to the inlet.

regime is characterized by a cooler and more distributed hot-spot along the entire central channel length. The microburner would oftentimes begin in the catalytic regime but would transition the the homogeneous regime. Once in the homogeneous regime, it would not transition back to the catalytic regime without some external disturbance, such as a brief decrease in fuel flow. Given that homogeneous combustion was predominant in the present study, simulations reported herein neglected catalytic combustion.

After the 150 hour run, we assessed the microburner. The center inlet tube was bowed several millimeters over its approximately 5 cm length. We attributed this to differential thermal expansion. The center inlet tube was cooled by the flowing gases and the outer outlet tubes were heated by the hot exhaust. The joint between the center inlet tube and the microburner leaked throughout the entire experiment but not enough to alter the heat input or degrade the vacuum enough for convection to occur. On the microburner itself, the area of the hot spot was bowed outwards and darkened, as shown in Fig. 4-8.

We cross sectioned the microburner at both the inlet and outlet channel to determine the cause of failure. The cross sections are shown in Fig. 4-8. The body (point a) and cap (point b) were visible. The catalyst in the outlet channel appeared black (point c) similar to fresh catalyst. The catalyst at the inlet appeared white and glassy (point d).

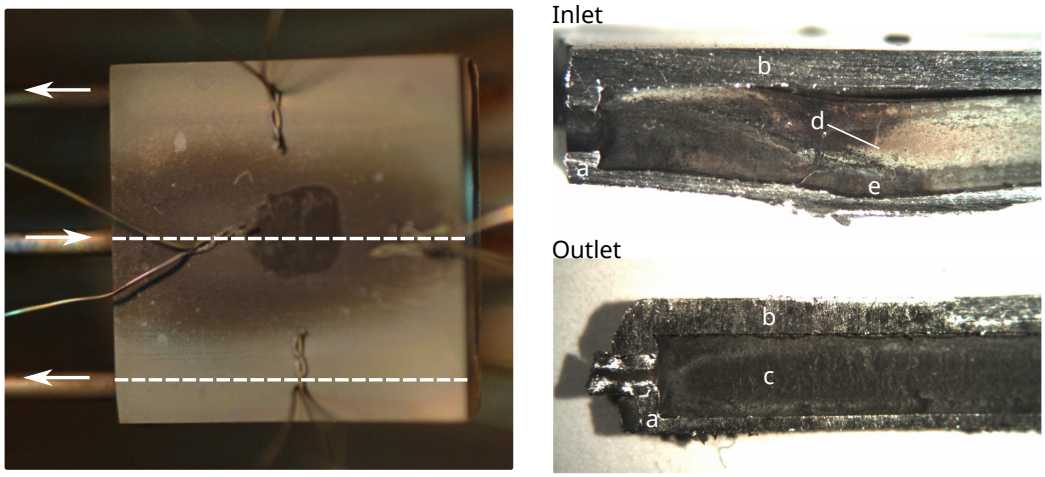

Figure 4-8: Microburner surface and cross sections of the inlet and an outlet channel after the 150 hour experiment. Labeled points are described in the text.

We suspect that the intense heat sintered the alumina support, deactivating the platinum catalyst. While alumina melts at 2072°C, it has been sintered as low as 1400°C. Given that the outside of the top surface reached 950°C and the bottom surface bowed (point e), the inside could have reached that temperature in the intense heat of a propane-oxygen flame.

4.3 TPV experiment

For the TPV system, we made several improvements to the three-tube design discussed in the previous section focused on eliminating the hot spot:

- **Additional inlet tubes.** The multiple inlets serves to divide the input power more uniformly to force a more uniform temperature distribution and, more importantly, eliminate extreme hot spots. We used five tubes: tubes 1 and 5 were tube-in-tube inlets delivering propane and oxygen coaxially, tubes 2 and 4 were additional propane inlets, tube 3 was the exhaust outlet. Tubes 2–4 had loops for strain relief. Multiple inlets also simplified the experimental setup: while orifice were still used to divide the flow, they did not need to be heated.

- **Interdigitated channel.** The combustion regime (homogeneous or catalytic) can be controlled through thermal and radical quenching by altering the channel geome-

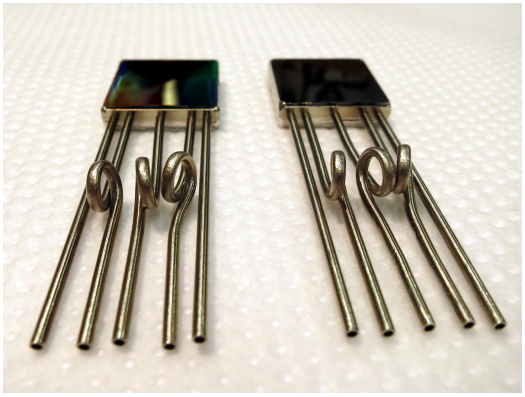

(a) Microburners after welding.

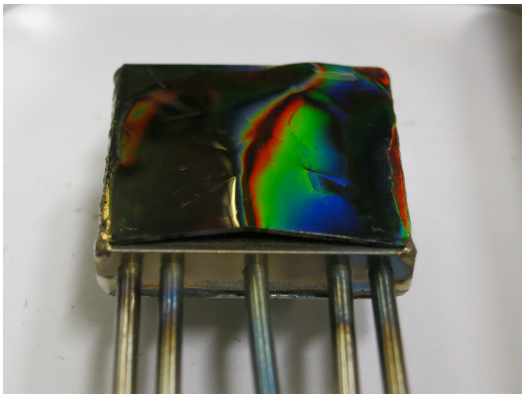

(b) Warped photonic crystal.

Figure 4-9: Photographs of the five-tube microburner.

try [70]. Because a smaller channel can prevent homogeneous combustion, we designed a top piece with a set of fingers that bisected the channels in the bottom piece. Thus, the channel width was cut in half without incurring the associated fabrication penalty of requiring tiny, fragile end mills. Experimentally, the smaller channel was observed to reduce the chance of homogeneous combustion but did not entirely eliminate it. We suspect that the quenching distance at ∼1200°C is ∼100 µm.

Not much time was invested in studying the combustion regimes and these two measures were meant to be simple fixes because a TPV microgenerator would use air rather than oxygen in the combustion reaction. The addition of nitrogen would greatly reduce the geometric requirements for pure catalytic combustion by (1) decreasing the flammability limit, (2) increasing the autoignition temperature, and (3) increasing the linear flow velocity while decreasing the flame velocity making it possible to blow the flame out [71].

We fabricated the improved five-tube microburners as described in Appendix C with two different emitters as listed in Table 4.1: (1) oxidized Inconel to provide a high emissivity surface, and (2) a tantalum photonic crystal. The photonic crystal was microfabricated by deep reactive ion etching using a SiO_2 hardmask patterned by interference lithography on a polished 500 µm tantalum 3%-tungsten substrate by Veronika Stelmakh [72]. The completed microburners are shown in Fig. 4-9a.

We integrated the new five-tube microburner into a larger version of the experimental setup used for the silicon system. The top cells were replaces with a window to allow for

Emitter	Sides	Cells	View factor
Inconel	$\varepsilon_s = 0.8$	1× 20×20 mm InGaAs	$F = 0.87$ (1.5 mm gap)
Ta PhC	$\varepsilon_s = 0.5$	2× 5×10 mm InGaAsSb	$F = 0.91$ (1.0 mm gap)

Table 4.1: Summary of the TPV systems experimentally investigated. The view factor calculation assumes a full 20×20 mm array.

optical ignition and infrared temperature measurements. In the case of oxidized Inconel, a single 20×20 InGaAs cell was used on the bottom. In the case of the photonic crystal, an a single 10×10 InGaAsSb cell array was used on the bottom. Reported electrical power output is scaled to a full cell array on both sides. The experimental setups are summarized in Table 4.1. The new microburner was operated in the same fashion as the three-tube microburner, with additional plumbing to feed the extra inlets.

Experimental results are shown in Fig. 4-10. The approximate emissivity of the oxidized Inconel was determined by comparing temperature readings with the infrared thermometer with and without a spot of high emissivity black paint. The two measurements matched when $\varepsilon_e = 0.8$ over the entire temperature range and agree reasonably well with the model. The temperatures were lower than those reported in Section 4.2 because of the higher emissivity. The temperature of the photonic crystal was not measured because its wavelength-dependent emissivity made infrared measurement difficult and we did not want to damage it with black paint.

The electrical power produced by the bare Inconel system matches well with the model and is similar to the bare silicon system which has a similar emissivity. The electrical power produced by the photonic crystal system fell short of the model prediction. We observed warping of the emitters after welding and further warping after extended high temperature operation as seen in Fig. 4-9. At the completion of this study, the gap was over 1 mm at the center. Given that the coefficient of thermal expansion (CTE) of Inconel is $12.6 \times 10^{-6}\,\mathrm{K}^{-1}$ and that of tantalum is only $6.5 \times 10^{-6}\,\mathrm{K}^{-1}$, we suspect that the tantalum deformed under the thermal stress at the operating temperature then bowed during cooling.

In vacuum, any gap (regardless of size) forces purely radiative transfer between the microburner and emitter. The heat transfer can be modeled analytically. Assume three black surfaces: (1) a hot surface at T_h, (2) a middle surface at temperature T_m, and (3)

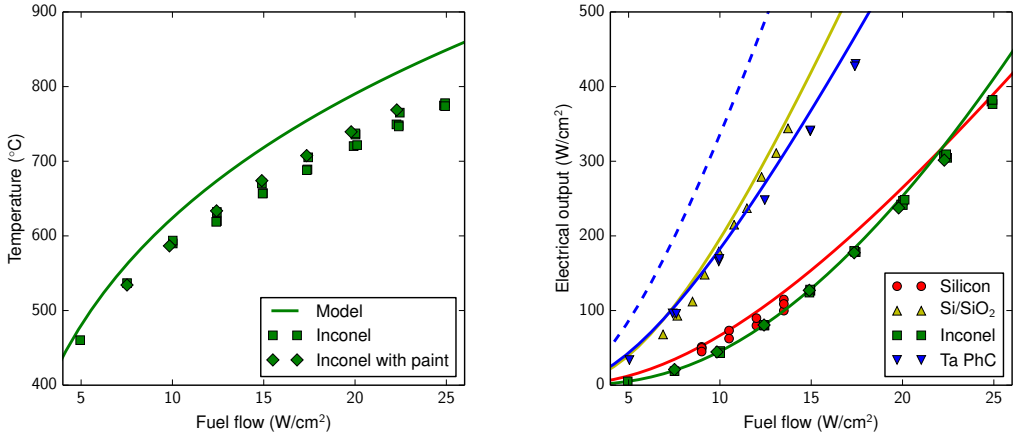

(a) Temperature.

(b) Electrical power.

Figure 4-10: Measured (points) and simulated (lines) temperature and power for the bare Inconel microburner.

Emitter	Temp.	Q_{exh}	Q_{cond}	Q_{side}	Q_{cavity}	Q_{spec}	Q_{iv}	Q_{elec}
$\varepsilon_e = 0.8$	1113 K	15.1%	3.6%	23.7%	7.9%	43.6%	4.4%	1.6%
PhC (rad.)	1262 K	18.2%	7.1%	45.6%	2.1%	15.2%	9.3%	2.4%
PhC (cond.)	1202 K	17.0%	6.7%	33.6%	3.2%	19.8%	15.5%	4.3%
Step func.	1198 K	16.9%	6.7%	33.2%	3.4%	11.5%	22.1%	6.3%

Table 4.2: Heat loss breakdown for the metallic system. The experimental photonic crystal system was simulated assuming radiative (rad.) and conductive (cond.) transfer between the microburner and photonic crystal. The step function emitter has $\varepsilon_{in} = 0.9$, $\varepsilon_{out} = 0.1$, and $\varepsilon_s = 0.5$. The $\varepsilon_e = 0.8$ has an input power of 100 W and all other systems are 60 W.

cold surface at T_c. Assuming only adjacent surfaces can communicate radiatively, the middle surface reaches a temperature

$$T_m = \left(\frac{T_h^4 + T_c^4}{2}\right)^{1/4} \tag{4.3}$$

and the heat transfer is reduced by half assuming $T_h \gg T_c$ as is the case in this situation. The true reduction in electrical output is greater than one half because (1) the lower emitter temperature has a lower spectral efficiency, (2) the emissivity on the back of the photonic crystal is lower than the front which further lowers the temperature, and (3) the reduced effective emissivity reduces the heat extraction from the combustion. We modified our model to support different microburner and emitter temperatures, with either pure conductive

or radiative coupling between the microburner and emitter. The necessary heat transfer equations were added to the heat balance, allowing the solver to find both temperatures by detailed balance as before.

The heat loss breakdowns for the experimental systems at operating points corresponding to the maximum experimental data point are given in Table 4.2, as well as for the photonic crystal system assuming conductive transfer from the microburner. In the oxidized Inconel system, the bulk of the heat was lost from the spectral mismatch between the grey body emission and the cells, as expected. The cavity loss was high because InGaAs cells have increased reflectivity outside their conversion region. In the experimental photonic crystal system, the bulk of the heat was radiated from the sides because the photonic crystal had an insulating effect on the microburner. Assuming conductive transfer, the side losses decrease and the cell losses increase due to the increased photocurrent.

We have proposed and performed a preliminary investigation into alternative photonic crystal integration methods: directly sputtering tantalum on Inconel and brazing. Although photonic crystal structures in 8 µm and 30 µm sputtered tantalum on Inconel coatings have been shown to be stable for short high temperature anneals, combining traditional machining and welding with microfabrication in a monolithic microburner-emitter will likely prove challenging. Diffusion brazing (BNi-2 foil from Lucas-Milhaupt, Ni-7%Cr-2.8%B-4.5%Si-3.0%Fe composition, 971°C solidus, 1000°C liquidus) was tested with tantalum and Inconel coupons and is a very promising pathway for near-term integration. During the brazing cycle at 1150°C in vacuum, the boron and silicon, which depressed the initial melting point of the braze, diffused into the parent metals thus allowing the brazed joint to remain solid above the original brazing temperature [73].

Chapter 5

Microgenerator Model

In this chapter, we extend the TPV system model from Chapter 2 to predict the performance of a complete TPV microgenerator in terms of its energy and power density by predicting its mass. Because the heat sink would likely be the heaviest component of a complete microgenerator, we developed a heat sink model and a temperature dependent cell model in order to find the lightest and most efficient microgenerator possible. We preformed the microgenerator optimization over the entire 1–100 W range and calculated the performance metrics developed in this chapter in order quantify the performance of our approach to a TPV microgenerator.

5.1 Energy and power density

As alluded to in Chapter 1, key properties for any microgenerator are its net electrical output power (P_{net}) and total beginning-of-mission mass which is comprised of the microgenerator mass (M_g) and fuel mass (M_f). It is helpful to normalize these quantities by defining the mission energy density and power density:

$$u = \frac{E_{tot}}{M_g + M_f} \tag{5.1}$$

$$p = \frac{P_{net}}{M_g + M_f} \tag{5.2}$$

where E_{tot} is the total net electrical energy produced over the course of the mission. We define the microgenerator's characteristic energy density and power density as:

$$u_\infty = \frac{E_{tot}}{M_f} \tag{5.3}$$

$$p_0 = \frac{P_{net}}{M_g} \tag{5.4}$$

where the characteristic energy density is achieved on an infinite length mission and the characteristic power density is achieved on an infinitesimal mission. Thus, the total mass (M_{tot}) can be written as

$$M_{tot} = M_g + M_f = \frac{P_{net}}{p_0} + \frac{E_{tot}}{u_\infty} \tag{5.5}$$

which allows us to determine a microgenerator's performance on any given mission. There are two limiting cases for the total mission mass, microgenerator mass dominated and fuel mass dominated:

$$M_{tot} \approx \begin{cases} P_{net}/p_0 & t \ll u_\infty/p_0 \text{ (Microgenerator mass dominated)} \\ E_{tot}/u_\infty & t \gg u_\infty/p_0 \text{ (Fuel mass dominated)} \end{cases} \tag{5.6}$$

where t is the mission duration. The crossover point u_∞/p_0 (where $M_f = M_g$) serves as a timescale for the microgenerator, which is approximately one day for our TPV microgenerator. Unfortunately, we cannot approximate mission energy density with the relatively well characterized u_∞ because typical mission durations are on the order of the u_∞/p_0. Thus, we will need to determine p_0 through modeling.

5.2 Required components

In order to accurately predict microgenerator performance, we need both u_∞ which is derived from the well characterized fuel-to-electricity efficiency and p_0 which is derived from poorly characterized microgenerator mass. Most experimental TPV work focuses on the TPV system (microburner, emitter, cells) or individual components, rather than a complete microgenerator. Theoretical studies were focused on the fuel-to-electricity or

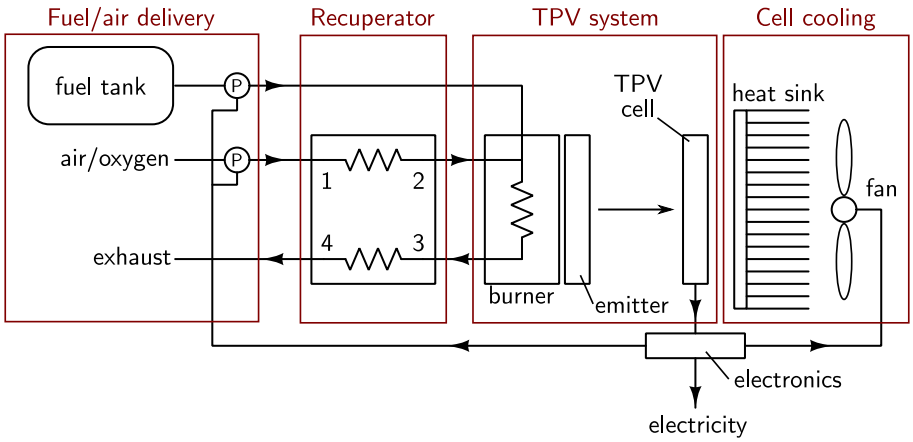

Figure 5-1: A block diagram of a TPV microgenerator. In addition to the TPV system itself, the microgenerator requires a fuel/air delivery system, recuperator, cell cooling, and power and control electronics.

heat-to-electricity efficiency rather than microgenerators [9, 74, 75]. Even for demonstrated TPV microgenerators with balance-of-plant, the was mass optimized and often not reported directly [12–14]. Thus, we are forced to resort to modeling to predict M_g by analyzing the components necessary for a TPV microgenerator, shown in Fig. 5-1:

- **A heat sink and fan** that can reject the waste heat from the cells with minimal temperature rise and minimal power consumption. For efficient fuel-to-electricity conversion, the cells must be cooled to as close to ambient as possible. If we assume InGaAsSb cells in a system similar to our experimental system, we will achieve 5.5% fuel-to-electricity at 20°C cell temperature, at 40°C the efficiency has dropped to 4.8% and at 60°C it is only 4.0%. The common laboratory approach of an external chilled water supply is not practical in a microgenerator. In a microgenerator, effective cell cooling costs both weight and power in the form of a large heat sink and fan.

- **A recuperator** to recover heat from the exhaust stream and transfer it to the incoming air. Our experiment used pure oxygen which greatly reduced the exhaust heat loss but is not practical in a microgenerator. In order to maintain the same microburner temperature and fuel-to-electricity efficiency with air, we need a $\eta_{rec} \approx 0.7$ recuperator according to the analysis in Table 5.1. Recuperators are classified according to their

effectiveness, the ratio of the achieved heat transfer to the maximum heat transfer:

$$\eta_{rec} = \frac{h_2 - h_1}{h_3 - h_1} \approx \frac{T_2 - T_1}{T_3 - T_1} \tag{5.7}$$

where h denotes enthalpy (subscripts given in Fig. 5-1) which can be approximated as temperature because the air and exhaust have approximately the same heat capacities. Lightweight recuperators with effectivenesses $\eta_{rec} \approx 0.6$–0.8 are under development for TPV [76] and microturbines [77, 78].

- **A fuel and air delivery** system that can deliver the reactants in the proper ratio to the microburner with minimal power, using either an electric blower or a Venturi powered by the vapor pressure of the propane. Because our experimental work used external mass flow controllers, we were not concerned with the pressure drop in the microburner. In a self-contained microgenerator, the pressure drop of the microburner and recuperator will need to be optimized. A microburner with minimal pressure drop was demonstrated by using multiple short channels in parallel instead of one long channel [79, 80]. We did not include the blower or Venturi, valves, or plumbing in the microgenerator mass because they will be light compared to the other components and their mass is largely independent of net electrical power output, and we did not account for the balance-of-plant electrical load because a Venturi could be used.

- **Vacuum packaging** to prevent oxidation and contamination of the photonic crystal emitter. Our experimental setup included an external vacuum pump which is not practical in a microgenerator. While difficult from an engineering perspective, vacuum packaging has been perfected for incandescent and fluorescent light bulbs, CRT monitors, and certain MEMS devices [81]. We expect the vacuum package to add minimal additional mass to the microgenerator.

The two heaviest components of a TPV microgenerator are the two heat exchangers: the recuperator and the heat sink. The heat sink will be heavier because of the low ΔT, thus providing our motivation to study it in detail.

Configuration	$T_2 - T_1$	T_b	Q_3	Q_4	Efficiency
Oxygen	0 K	1314 K	18 W	18 W	5.3%
Air	0 K	1211 K	40 W	40 W	3.0%
Recuperator	733 K	1314 K	45 W	18 W	5.3%

Table 5.1: A comparison of the TPV system performance with oxygen, air, and air with a recuperator for a fuel input of $Q_{comb} = 90$ W in all cases. With the recuperator, 45 W of heat are contained in the exhaust directly from the microburner, of which 27 W are recovered and used to preheat the incoming air by 733 K, and the remaining 18 W leave the recuperator in the exhaust stream.

5.3 Cell cooling model

In this section we attempt to understand the three-way trade off between heat sink mass, fan power, and thermal resistance in order to numerically build a microgenerator with minimum total mass. To do this, we modeled a fan cooled heat sink—fan cooling was chosen because even a modest air flow can greatly reduce the size of the heat sink necessary for a given thermal resistance, thus increasing the energy density relative to earlier modeling work on passively cooled microgenerators [82]. The final result is a model that can predict the thermal conductance of a optimal heat sink for given external dimensions and pumping power (pressure drop $\times$ flow), which was later incorporated into our TPV system model to form a complete microgenerator model. Our choice of pumping power as the model's input rather than the more common air flow velocity complicated the heat sink model but simplified the microgenerator model because we need only specify how much electrical power is allocated to the fan. We assumed a constant fan efficiency.

Using the procedure detailed in Appendix F, we modeled a fully ducted heat sink with geometry as given in Fig. 5-2: the heat source was a square TPV cell with width W_{tpv} connected to the square heat sink with width W_{hs} by a heat spreader plate of thickness H_{base}. The heat sink itself was comprised of fins of width W_{fin} and height H_{fin}, and the channels between fins were of width W_{ch}. We assumed an airflow over the fins with a free-stream volumetric flow rate of $\dot{v}$.

Given all six heat sink dimensions (W_{tpv}, W_{hs}, H_{base}, H_{fin}, W_{fin}, and W_{ch}) and the air flow ($\dot{v}$), we calculated the thermal conductance between the TPV cell and the air as well

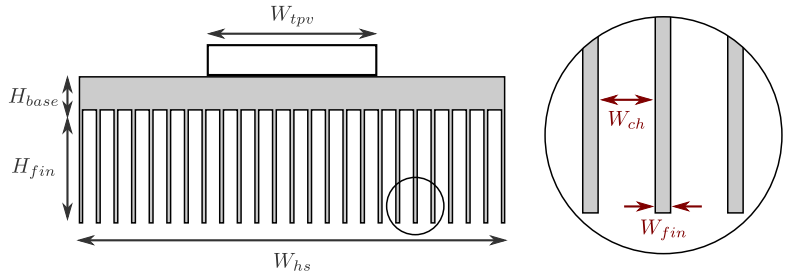

Figure 5-2: The geometry of the heat sink. Dimensions shown in red are determined algorithmically.

as the pumping power required to move the air across the heat sink in a straightforward manner. As an example, in Fig. 5-3a we calculated the thermal conductance of a copper heat sink with fixed external dimensions ($W_{hs} = W_{tpv} = 20$ mm, $H_{fin} = 10$ mm, $H_{base} = 3$ mm) as a function of the internal dimensions (W_{fin} and W_{ch}) for a pumping power $P_p = 0.1$ W. At each point of the graph, an airflow was found to satisfy the pumping power specification then that airflow was used to calculate the thermal conductance as usual.

This calculation was not particularly useful for our purpose because we do not know these dimensions beforehand and we did not want to add seven dimensions to the already complex problem of designing a TPV microgenerator. Fortunately, there was clearly an optimal set of internal dimensions: the highest thermal conductance achievable was $K_{hs} = 0.72$ W/K with a fin width $W_{fin} = 0.08$ mm and channel width of $W_{ch} = 0.55$ mm. Thus, with specified external dimensions (W_{tpv}, W_{hs}, H_{base}, and H_{fin}) we can determine the fin and channel dimensions (W_{fin} and W_{ch}) that provide the highest thermal conductance for a given pumping power. We applied this method and calculated the thermal conductance of the heat sink with optimized internal dimensions as a function of width (W_{hs}) and pumping power (P_p) for fixed $W_{tpv} = 20$ mm, $H_{fin} = 10$ mm, and $H_{base} = 3$ mm in Fig. 5-3b. At each point on this graph, the internal dimensions were optimized and the thermal conductance was calculated from those dimensions.

This model effectively captures the three-way trade off between heat sink mass, fan power, and thermal conductance. As in Fig. 5-3b, increased pumping power or heat sink size increases the thermal conductance. Exactly what thermal conductance is required and whether it is better to pay with microgenerator mass or additional fuel is the subject of the

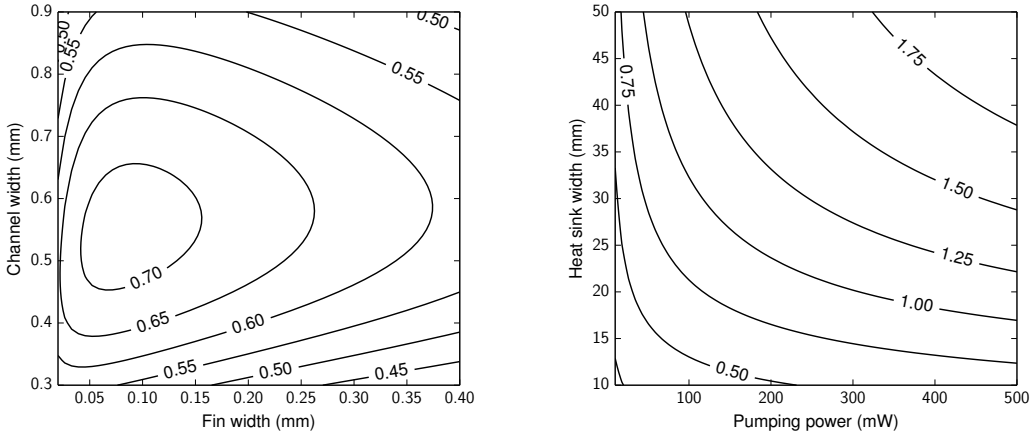

(a) Fixed geometry. (b) Optimized geometry.

Figure 5-3: Thermal conductance [W/K] of a heat sink with (a) fixed geometry and pumping power and (b) optimized internal geometry for specified external geometry and pumping power.

microgenerator optimization.

5.4 Microgenerator optimization

In this section, we combined the heat sink model, temperature dependent cell model, and TPV system model to predict microgenerator performance. We assumed a TPV system identical to the experimental system except with perfect microburner-emitter thermal contact, a side emissivity of $\varepsilon_s = 0.2$, and variable dimensions as shown in Fig. 5-4a. We allowed the TPV system width and heat sink dimensions to vary but kept the microburner thickness and microburner-cell gap fixed at 4.2 mm and 1.0 mm, respectively. Design of the microgenerator is a five-dimensional problem: square microburner and cell width (W_{tpv}), square heat sink width (W_{hs}) and height (H_{hs}), heat sink base thickness (H_{base}), and pumping power (P_p). We assumed a constant fan efficiency of $\eta_{fan} = 25\%$.

We plotted total (microgenerator and fuel) mass for variable W_{tpv} and W_{hs} and for fixed $H_{hs} = 20$ mm, $H_{base} = 2$ mm, $P_{fan} = 0.25$ W in Fig. 5-4b. We assumed a 5 W electrical load and a three day mission. This was accomplished by combining the heat sink and fan model, temperature dependent cell model (Appendix E), and the TPV system model

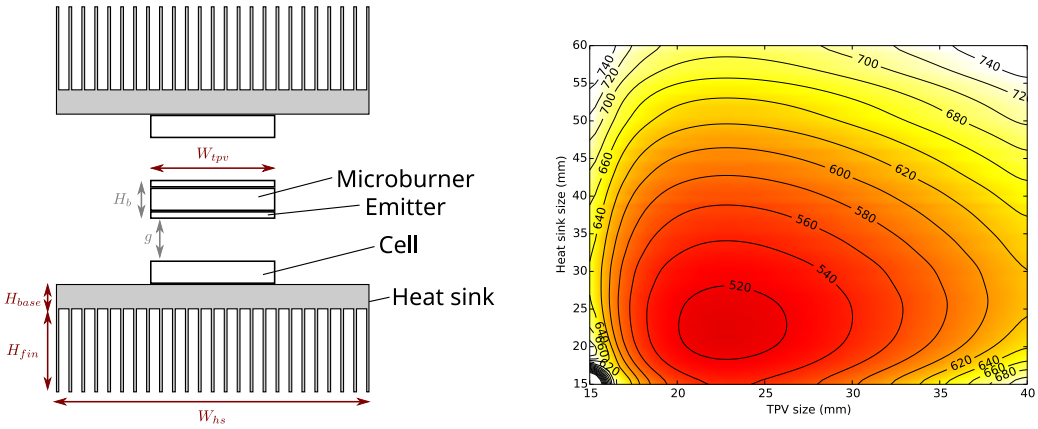

(a) Geometry (b) Heat sink

Figure 5-4: (Left) The geometry of the TPV system to be optimized. Grey dimensions are fixed and red dimensions are optimized. (Right) Total mass [g] for variable W_{tpv} and W_{hs} and for fixed H_{hs}=20 mm, H_{base}=2 mm, P_{fan}=0.25 W, for a 5 W, 3 day mission. The simulation failed to converge in the bottom left corner because no fuel flow could meet the power spec.

(Chapter 2) to form a complete microgenerator model. The heat sink and fan model was used to find the thermal conductance between the TPV cells and the ambient. Then, the TPV model was run to find the electrical output for a given fuel flow, while accounting for cell temperature. The fuel flow was adjusted (by SciPy's `newton` which implemented the Newton-Raphson method) such that the electrical output power $P_{net} = P_{elec} - 2\eta_{fan}P_p$ (we assumed a fan on each side) matched the specified net electrical power. Calculation of each point took about a minute.

Fig. 5-4b illustrates both the trade-off with W_{tpv} and W_{hs}. The TPV width sets the power density and hence emitter temperature, and the trade-offs discussed in Section 2.1 apply. The heat sink size trades off thermal conductance for mass. In this case, the minimum mass occurs when the TPV system and heat sink are approximately the same size, aided by the spreading resistance.

We applied the above procedure to optimize a family of microgenerators (over all five dimensions) with specified powers ranging P_{net} = 1–100 W on a three day mission. Total (microgenerator and fuel) mass was used as the figure of merit and the optimization was carried out with SciPy's `fmin` which implemented the Nelder-Mead simplex algorithm. The runtime for an individual optimization was 20 minutes to several hours, depending on the

Net power	T_b	T_j	M_g	M_f	u
1 W	1280 K	320 K	9.7 g	123 g	456 Wh/kg
5 W	1331 K	329 K	48 g	440 g	703 Wh/kg
10 W	1365 K	328 K	149 g	844 g	706 Wh/kg
20 W	1386 K	334 K	328 g	1560 g	717 Wh/kg

Table 5.2: Microgenerator optimization results.

initial guess. Optimization results for several values of P_{net} are listed in Table 5.2 and all data are plotted in Fig. 5-5. The average characteristic energy and power density for the range are given in Table 5.3.

Microgenerator width, heat sink width, and fan power were the most sensitive optimization parameters. In Fig. 5-5a and 5-5b, points from individual optimizations fall along a line for each graph, indicating convergence and validating the scaling of our TPV microgenerator. The spread is caused by the fact that multiple microgenerators can be designed that have approximately the same energy density and some optimizations may have failed to reach the global optimum. The TPV active area was consistently sized at $\sim$1 W/cm^2 of microburner area (500 mW/cm^2 of cell area). Higher power power densities are not desirable both because the high photocurrent causes excessive losses in the cell's series resistance and the higher microburner temperature leads to increased parasitic losses. Heat sink thermal conductivity scaled linearly with electrical power to maintain a $\sim$40°C temperature rise to $\sim$60°C. This was accomplished by a linear increase in heat sink area to maintain an area slightly larger than the TPV area and a linear increase in fan power up to about $P_{net} = 80$ W. Above this power, the spreading resistance associated with a larger heat sink became prohibitive and increased fan power was used to maintain the cell temperature. This effect limits the useful power range for this microgenerator design. At higher powers, heat pipes or liquid cooling (rather than the base of the heat sink which serves as a heat spreader) would need to be employed to effectively transfer the $\sim$1 kW of waste heat to a larger heat sink where it can be dissipated. Pyrolytic graphite would is also an appealing heat spreader material because of its high in-plane conductivity and low density [83].

Fuel mass, microgenerator mass, and total mass increase approximately linearly with net electrical power, indicating constant energy density and power density: the average

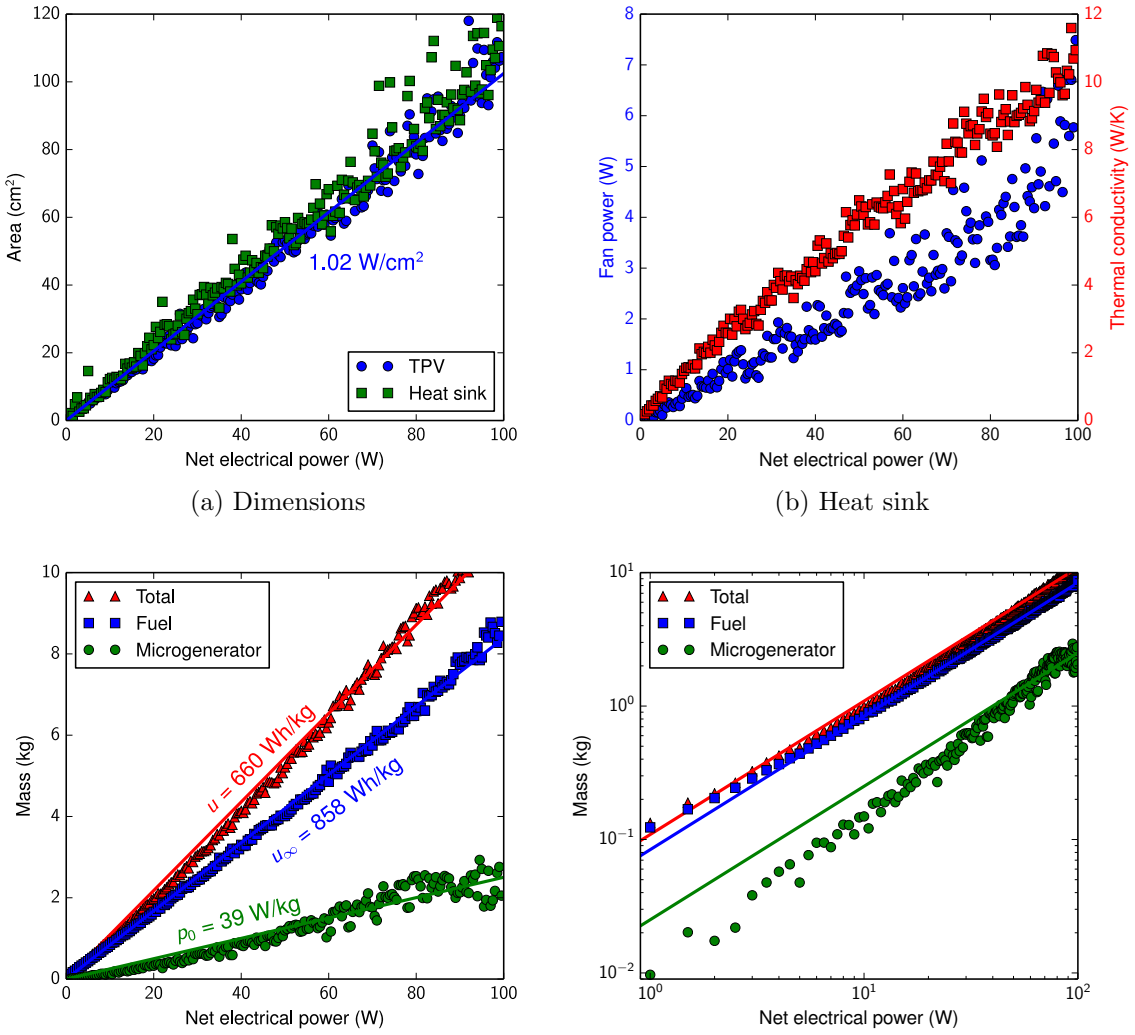

(a) Dimensions

(b) Heat sink

(c) Mass (linear scale)

(d) Mass (log scale)

Figure 5-5: TPV microgenerator optimization results as a function of net electrical output power. All other parameters are as before.

fuel-only energy density is 858 Wh/kg, the total energy density is 660 Wh/kg, and the power density is 39 W/kg, as summarized in Table 5.3. When plotted on a logarithmic scale to emphasize low electrical powers, we see that the constant energy and power density approximation are not completely accurate. At low electrical powers, the microgenerator mass is lighter than expected and the energy density is lower than expected. Two effects are responsible for this: (1) at low powers, the generator weight becomes more significant and the optimization will trade efficiency for generator weight, and (2) at low powers it becomes

Microgenerator	u_∞	p_0
Current	858 Wh/kg	39 W/kg
Improved	1109 Wh/kg	45 W/kg

Table 5.3: Modeling predictions for the optimized 1-100 W TPV microgenerators based on the current experimental setup and with an improved photonic crystal and added cold side filter.

more difficult to build an efficient generator because of the fixed microburner thickness and microburner-cell distance.

5.5 TPV microgenerator improvements

While the predicted TPV microgenerator performance was good, we can further improve performance by incorporating the following:

- **Cold side filter.** A cold side filter is an optical filter on the front surface of the TPV cell that transmits convertible radiation to the cell and reflects unconvertible radiation back to the emitter, as shown in Fig. 5-6a. A cold side filter can improve efficiency by recycling photons back to the emitter and can reduce the thermal load on the heat sink. The demands on the cold side filter in at photonic crystal TPV system are relatively modest compared to those in a system that relies solely on the cold side filter for spectral control.

- **Filled photonic crystal.** The emissivity of a photonic crystal emitter decreases quickly for off-normal angles resulting in greatly reduced total hemispherical emission. Recent developments suggest the off-normal emissivity of a dielectric-filled photonic crystal can approach the normal emissivity as shown in Fig. 5-6b.

We analyzed a TPV microgenerator with a cold side filter and a filled photonic crystal.

5.5.1 Cold side filter

Historically, cold side filters have been used with a blackbody emitter as an alternative to selective emitters. Although simple interference filters can be used [34], the large stop

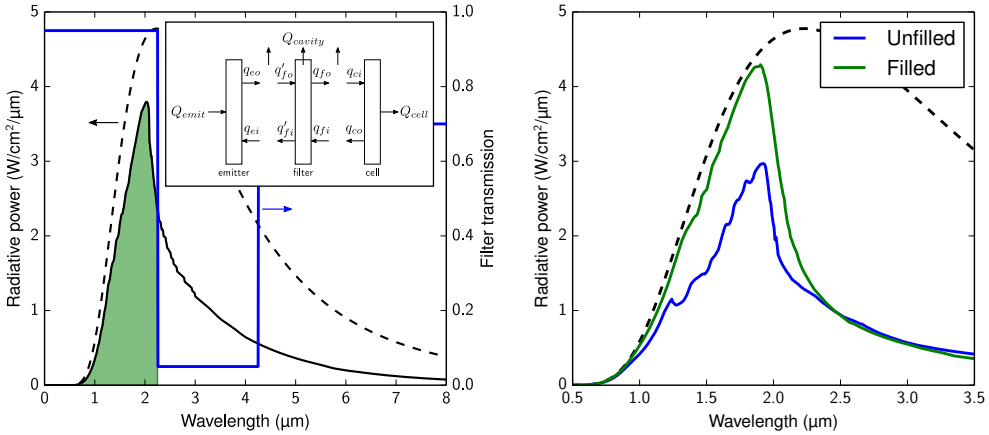

(a) Filter. (b) Filled cavities.

Figure 5-6: TPV system improvements include (a) a cold side filter and (b) a filled cavity photonic crystal. In (b), the hemispherically averaged thermal emission is shown.

band of ∼10 μm required for effective photon recycling is better covered by a tandem combination of an interference filter and a plasma filter [84–86] or micro-resonator frequency selective surface [87]. In addition to the experimental difficulties associated with the large stop band (>50 layers, exotic materials), the approach had limited applicability to TPV microgenerators because of the high required cavity efficiency thus placing severe restrictions on the view factor and the acceptable loss or out-of-band transmission of the filter.

When used with a selective emitter, the cold side filter needs only "clean up" the relatively slow roll off of the emitter which can be achieved with a simple interference filter with a stop band of only $\lambda_{bw} \approx 2$ μm. We assume a lossless filter with reflectance given by

$$\rho_f = \begin{cases} 0.05 & \lambda < \lambda_g \\ 0.95 & \lambda_g < \lambda < \lambda_g + \lambda_{bw} \\ 0.30 & \lambda > \lambda_g + \lambda_{bw} \end{cases} \tag{5.8}$$

where λ_g is the desired cutoff wavelength at the bandgap of the TPV cell and λ_{bw} is the bandwidth of the stop band. This approximation was used in Ref. 48 and is consistent with the performance of the above filters.

We extended the optical cavity model from Chapter 2 to three components: an emitter,

filter, and cell as shown in the inset of Fig. 5-6a. The detailed balance matrix equation becomes:

$$\begin{bmatrix} 1 & -\rho_e F & 0 & 0 \\ -\rho_f F & 1 & 0 & -\tau_f \\ -\tau_f F & 0 & 1 & \rho_f \\ 0 & 0 & -\rho_c & 1 \end{bmatrix} \begin{bmatrix} q_{eo} \\ q'_{fo} \\ q_{fo} \\ q_{co} \end{bmatrix} = \begin{bmatrix} \varepsilon_e e_b(\lambda, T_e) \\ 0 \\ 0 \\ 0 \end{bmatrix} \tag{5.9}$$

which can be solved for the quantities of interest:

$$q_{ci} = \frac{F\tau_f}{(1-\rho_f\rho_c)(1-F^2\rho_e\rho_f) - F^2\rho_c\rho_e\tau_f^2}\varepsilon_e e_b(\lambda, T_e) \tag{5.10}$$

$$q_{eo} - q_{ei} = \frac{(1-F^2\rho_f)(1-\rho_f\rho_c) - F^2\tau_f^2\rho_c}{(1-\rho_f\rho_c)(1-F^2\rho_e\rho_f) - F^2\rho_e\rho_c\tau_f^2}\varepsilon_e e_b(\lambda, T_e) \tag{5.11}$$

which reduce to the case of no filter when $\tau_f = 1$ and $\rho_f = 0$. For simplicity and to be consistent with the literature, we used the normal incidence reflectance even though the hemispherically averaged reflectance would be more accurate.

5.5.2 Filled photonic crystal

Although emissivity at normal incidence is commonly reported, the emissivity of a photonic crystal emitter decreases quickly for off-normal angles resulting in greatly reduced total hemispherical emission. Indeed, in our simulations we used the hemispherically averaged emissivity to account for this effect. Recent developments suggest that dielectric filled cavities can improve off-normal emissivity by reducing the physical hole diameter while maintaining the same optical diameter to minimize diffraction [88, 89].

In order to quantify the performance of the emitters, we found the average in-band (ε_{in}) and out-of-band (ε_{out}) emissivities for filled and unfilled photonic crystals. We performed a least-squares fit of a sigmoid function of the form

$$\varepsilon = \varepsilon_{in} - \frac{\varepsilon_{in} - \varepsilon_{out}}{1 + e^{-k(\lambda - \lambda_c)}} \tag{5.12}$$

where λ_c is the cutoff wavelength and k describes the sharpness of the cutoff, on the filled and unfilled photonic crystal emitters using a 1200°C blackbody curve as weighting. The results

Structure	ε_{in}	ε_{out}	λ_c	k	Ref.
Unfilled	0.583	0.184	2.40 µm	1.68×10^7	
Unfilled	0.594	0.168	2.09 µm	1.36×10^7	88
Filled	0.922	0.154	2.10 µm	1.29×10^7	88

Table 5.4: Hemispherical emission parameters for filled and unfilled photonic crystals. The first row is the photonic crystal used in this work.

from literature structures as well as the photonic crystal used in this work are presented in Table 5.4. A filled photonic crystal offers a 55% relative increase in in-band emissivity without a detectable increase in out-of-band emissivity. In this simulation, we shifted the cutoff wavelength to match the InGaAsSb cells used in this work while maintaining the average in-band and out-of-band emissivities.

5.5.3 Results

We repeated the microgenerator optimization over the 1–100 W range and found an energy density of $u_\infty = 1109$ Wh/kg and a power density of $p_0 = 45$ W/kg with a cold side filter and filled photonic crystal. The results are shown in Fig. 5-7 and listed in Table 5.3.

We have not exhausted the opportunities for improvement: the fuel-to-electricity efficiency for an idealized combustion driven TPV system is about 30% and the theoretical limit is twice that [9]. Improved TPV cells represent another avenue for improved efficiency. Current fabricated TPV cell performance is limited to about 50% of the thermodynamic limit whereas current state-of-the-art silicon PV cells approach ∼85% of the thermodynamic limit [75]. Thus, if some of the innovations from silicon PV were applied to TPV, the heat-to-electricity conversion efficiency could greatly increase.

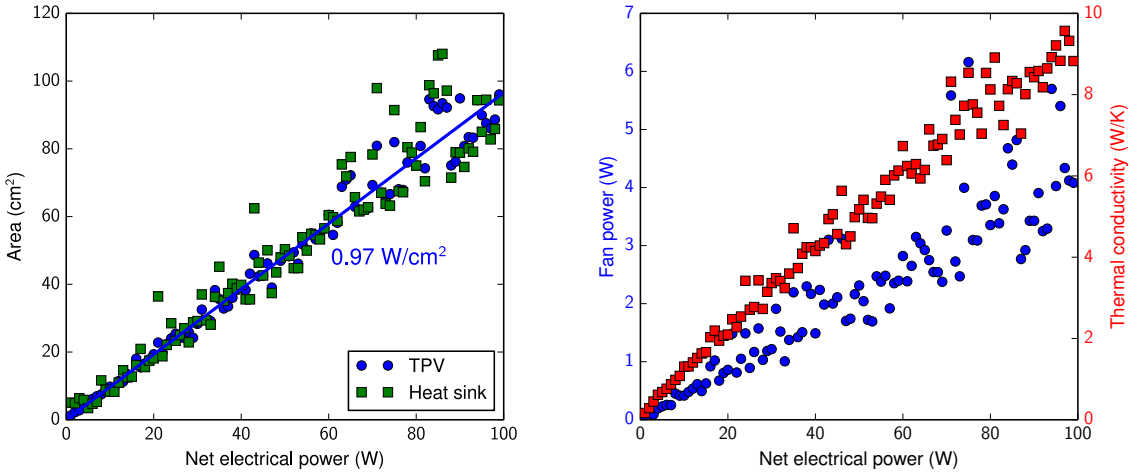

(a) Dimensions

(b) Heat sink

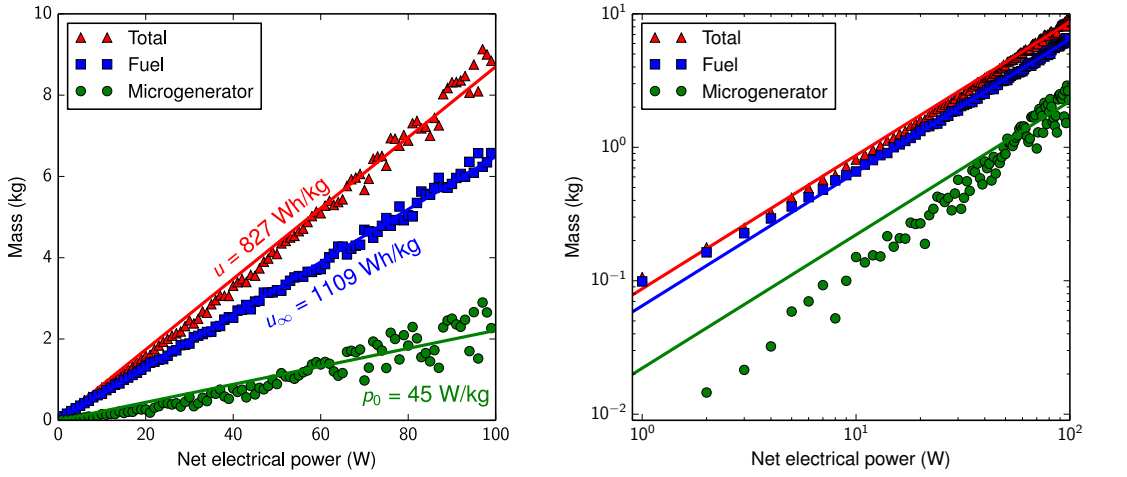

(c) Mass (linear scale)

(d) Mass (log scale)

Figure 5-7: Microgenerator optimization results including a cold side filter and filled photonic crystal.

Chapter 6

Conclusion

In this chapter we compare the performance of the modeled TPV microgenerator with literature microgenerators, and confirm our hypothesis that it is possible to build a high performance TPV microgenerator with a photonic crystal emitter. We then outline a plan to realize the proposed TPV microgenerator. Finally, we summarize the thesis results and contributions.

6.1 Comparison with other microgenerators

We scoured the literature for experimental demonstrations of all classes of microgenerators: electrochemical, mechanical, and thermal. Their characteristics were converted to u_∞ and p_0, and these values as well as rated electrical power output and are reported in Table 6.1. Microgenerators were plotted on a Ragone plot in Fig. 6-1a which plots energy density against power density [90]. Individual microgenerators appear as points at coordinates given by u_∞ and p_0. Batteries appear as lines because they can be discharged at a variable rate. Diagonal lines represent the runtime for which microgenerator mass and fuel mass contribute equally to the total mass in the case of a microgenerator and discharge time in the case of a battery. The Ragone plot does not capture scaling effects: there is no indication of the absolute size of the microgenerator. Thus, we plotted the mission energy density for a three day mission as a function of power in Fig. 6-1b.

Our approach to a TPV microgenerator has characteristic energy and power densities

Microgenerator		P_{net} [W]	u_∞ [Wh/kg]	p_0 [W/kg]	Ref.
MTI	DMFC	0.5	205.7	5.6	2
MiniPak	PEMFC	2.0	133.3	16.7	6
Motorola	DMFC	2.5	850.0	7.1	2
Lilliputian	SOFC	2.5	2391.3	12.6	91
MTI	DMFC	5.0	212.8	5.0	2
Marton	TE	6.0	386.2	6.0	79
PowerTrek	PEMFC	6.5	233.3	24.1	92
Cox	Piston	10.2	253.2	237.2	93
uTurbine	Turbine	15.0	937.5	300.0	94
Ball	DMFC	20.0	1200.0	11.4	2
Doyle	TPV	20.0	257.5	7.7	14
MICSE	Piston	21.1	1582.9	42.2	95
Sunpower	Piston	35.0	2188.8	21.9	96
D-STAR	Piston	40.0	643.8	40.0	4
Teleki	TE	45.0	99.2	8.3	97
DecaWatt	Turbine	50.0	643.8	200.0	98
Corry	TE	63.0	412.0	11.6	99
Corry	TE	78.0	579.4	12.3	99
Quantum	TPV	85.0	93.7	12.5	12
Corry	TE	100.0	309.0	4.7	100
Protonex	SOFC	200.0	2222.2	16.7	101
AMI	SOFC	245.0	2187.5	22.5	102
Angello	TE	280.0	448.6	24.9	103
Protonex	DMFC	300.0	833.3	18.8	104
Neild	TE	300.0	423.3	29.4	105
Angello	TE	560.0	448.6	35.6	103
Bass	TE	605.0	415.8	25.8	106
Angello	TE	840.0	448.6	37.3	103
Honda	Piston	900.0	2011.8	69.1	107
DynaJet	Turbine	2600.0	1545.0	173.3	108

Table 6.1: Power and energy densities of microgenerators from the literature, with output powers ranging over nearly four orders of magnitude. Microgenerators are classified as proton exchange membrane (PEM), direct methanol (DMFC), or solid oxide (SOFC) fuel cells, as piston or turbine mechanical engines, or as thermoelectric (TE) or TPV solid state generators.

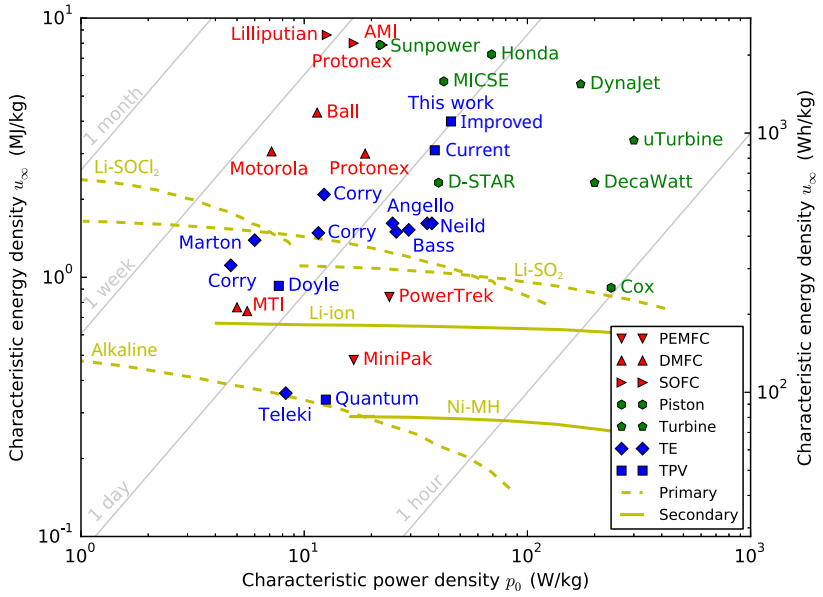

(a) Ragone plot of characteristic energy density (u_∞) and characteristic power density (p_0).

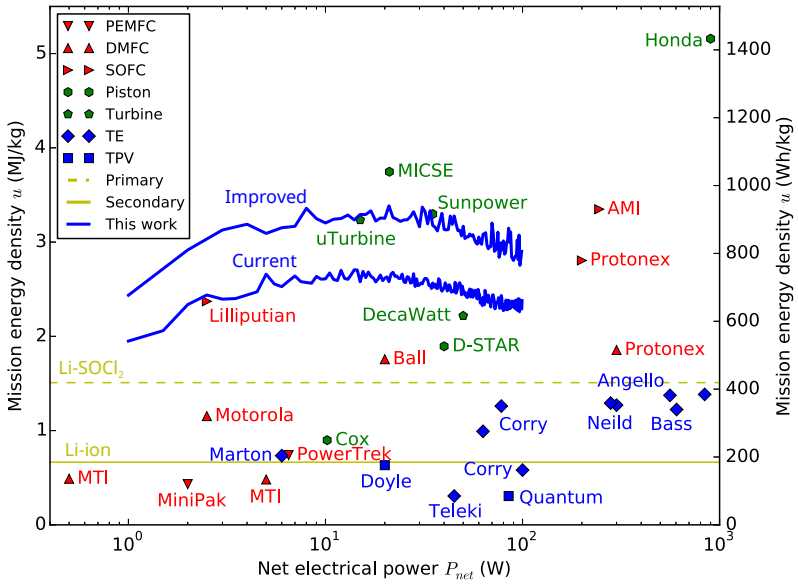

(b) Total energy density for a three day mission as a function of power.

Figure 6-1: The performance of the modeled TPV microgenerator compared to the literature both in terms normalized for size (a) and in terms of size (b).

comparable to other microgenerators. Its advantage lies in the 3–30 W range where it can easily outperform most fuel cells but before mechanical engines and fuel cells with active balance-of-plant become feasible. TPV may even be advantageous in the 30–100 W range because it is a static conversion process and can burn dirty fuels.

The plotted microgenerators are broadly classified as

- **Piston engines** are scaled-down versions of conventional engines and are able to leverage a mature and highly developed technology. Internal combustion engines tend to have the highest power density but a low efficiency at small scales. The rapid decrease in efficiency is caused by increased surface area to volume ratio resulting in increased mechanical and thermal losses, increased leakage and friction losses due to fabrication challenges, increased operating speed due to decreased displacement volume, and difficulties of discontinuous combustion resulting in poor fuel usage and requiring low energy fuel such as methanol/nitromethane. Nevertheless, millimeter-scale piston engines with respectable energy density have been demonstrated. Alternative internal combustion engines such as Wenkel engines [109] and swing engines [95] as well as sterling engines which decouple combustion from the thermodynamic cycle [96] are promising although noise and vibration are a challenge for all mechanical engines.

- **Turbine engines** have a single albeit complex moving part allowing for potentially simplified fabrication and increased reliability. Furthermore, the compression, combustion, and expansion cycles are physically decoupled, making it easier to sustain combustion at the mesoscale compared to an internal combustion engine. Like other mechanical engines, turbines performance suffers when scaled down: in addition to added heat loss, the decreased rotor diameter forces the rotation speed to increase (upwards of one million rpm [94]) to develop appreciable power resulting increased frictional losses and material stresses as well as challenging associated with the bearings.

- **Proton exchange membrane fuel cells (PEMFCs)** are a mature technology that relies on a polymer (often DuPont Nafion, a sulfonated tetrafluoroethylene) membrane permeable to protons but not electrons or the reactants. In a PEMFC, hydrogen is

supplied at the anode and air is supplied at the cathode:

$$\mathrm{H_2} \xrightarrow{\mathrm{Pt}} \mathrm{H^+} + 2\,\mathrm{e^-} \qquad \text{(anode)} \tag{6.1}$$

$$\tfrac{1}{2}\mathrm{O_2} + 2\,\mathrm{H^+} \xrightarrow{\mathrm{Pt}} \mathrm{H_2O} \qquad \text{(cathode)} \tag{6.2}$$

where protons diffuse through the membrane separating the anode and cathode, and electrons move through the external electrical load. The electrodes are comprised of catalyst supported on porous carbon embedded with electrically conductive fibers to allow for electron and reactant transport. Although PEMFCs offer efficiencies of 60% at kW power scales [110], their energy density is low primarily because of the difficulty storing hydrogen.

- **Direct methanol fuel cells (DMFCs)** offer higher energy density than PEMFCs because methanol is an easy-to-store liquid. In a DMFC, methanol is supplied at the anode and air is supplied at the cathode:

$$\mathrm{CH_3OH} + \mathrm{H_2O} \xrightarrow{\mathrm{Pt,\ Ru}} \mathrm{CO_2} + 6\,\mathrm{H^+} + 6\,\mathrm{e^-} \qquad \text{(anode)} \tag{6.3}$$

$$\tfrac{3}{2}\mathrm{O_2} + 6\,\mathrm{H^+} \xrightarrow{\mathrm{Pt}} 3\,\mathrm{H_2O} \qquad \text{(cathode)} \tag{6.4}$$

  and protons move through a proton exchange membrane as before. Water management (water is produced at the cathode and consumed at the anode), methanol crossover, low power density, and balance-of-plant at millimeter scales are some challenges [111]. The best power densities reported for DMFC with comparable size to our TPV system are in the range from 4–30 $\mathrm{mW/cm^2}$ at an efficiency of ∼14% [112] but it has not been demonstrated in or extrapolated to a microgenerator.

- **Solid oxide fuel cells (SOFCs)** operate at high temperatures and offer higher energy density than DMFCs because they can process hydrocarbon fuels with twice the energy density of methanol. In a SOFC, internally reformed fuel is supplied to a Ni-$\mathrm{ZrO_2}$ cermet anode and air is supplied to a $\mathrm{La_{1\text{-}x}Sr_xMnO_3}$-$\mathrm{La_{1\text{-}x}Sr_xCoO_3}$ cathode:

$$\mathrm{H_2} + \mathrm{O^{2-}} \xrightarrow{\mathrm{Ni}} \mathrm{H_2O} + 2\,\mathrm{e^-} \qquad \text{(anode)} \tag{6.5}$$

$$\mathrm{CO} + \mathrm{O}^{2-} \xrightarrow{\mathrm{Ni}} \mathrm{CO}_2 + 2\,\mathrm{e}^- \qquad \text{(anode)} \qquad (6.6)$$

$$\tfrac{1}{2}\,\mathrm{O}_2 + 2\,\mathrm{e}^- \longrightarrow \mathrm{O}^{2-} \qquad \text{(cathode)} \qquad (6.7)$$

where the O^{2-} ions diffuse through a yttria-stabilized zirconia membrane which becomes permeable at 400–900°C. Because the oxygen rather than the fuel diffuses through the membrane, the fuel becomes diluted with exhaust and cannot be recycled. In addition to the anode and cathode, a SOFC system needs a (possibly catalytic) fuel reformer to partially oxidize the hydrocarbon fuel to hydrogen and carbon monoxide and a tail gas burner to combust any unreacted fuel to maintain the high temperature, which are all packaged into a single integrated unit [113, 114]. Although demonstrated, implementation of a robust solid oxide fuel cell at the millimeter scale is difficult because of the high temperature, heterogeneous material system.

- **Thermoelectrics (TE)** convert heat to electricity by the thermal diffusion of charge carriers across a temperature gradient. The challenge is engineering the TE materials with high electrical conductivity but low thermal conductivity, which is achieved by creating a complex crystallographic unit cell or through nanostructuring. Typical materials are Bi_2Te_3 and Sb_2Te_3-Bi_2Se_3 alloys for 200–300°C, PbTe, TAGS, and skutterudites for up to 600°C, and SiGe for up to 1000°C [115]. Higher temperatures improve efficiency but heterogeneous materials (the *n*- and *p*-type TE materials, interconnects, electrical isolation, and the heat source) at high temperatures [116, 117] as well as oxidation and sublimation of the TE materials [118, 119] prove challenging. For these reasons and the lack of readily available high temperature TE materials, the microgenerators presented here operate at low temperatures. The low temperature, low figure of merit $ZT \approx 1$ achieved to date, and high gravimetric density of the TE materials severely constrain microgenerator energy density, although experimentally demonstrated high temperature materials such as SiGe [120] in a microgenerator could yield 600–700 Wh/kg [82].

The literature TPV microgenerators suffer from poor energy density and power density because of the relatively low emissivity and low selectivity of their natural emitters as

discussed in Chapter 1. Although our TPV microgenerator has yet to be realized, it has the potential to achieve much higher performance because of its high emissivity, high selectivity photonic crystal emitter.

6.2 Route to a TPV microgenerator demonstration

In this section, we present a practical route to a microgenerator demonstration. Many recommendations have been made in this thesis on how to design and optimize a TPV microgenerator, but this section focuses on a practical approach that can be implemented with limited resources. A microgenerator demonstration is necessary to experimentally validate out performance predictions which will help TPV gain traction.

There are two major technical challenges between our current experimental system and a portable microgenerator: vacuum packaging necessary for photonic crystal stability and implementing a recuperated, air-breathing microburner. We propose to address vacuum packaging first because the photonic crystal emitter is the enabling component in our TPV microgenerator, despite the more common approach of demonstrating a recuperated air-breathing microburner before attempting spectral control [12–14]. We propose that two microgenerators be built:

- **Generation I** will focus on vacuum packaging the current microburner and brazed photonic crystal then demonstrating it with the current TPV cells. Although not practical for portable use, a self-contained microgenerator demonstration can be preformed using stored oxidizer. If passive cooling is used, there will be no balance-of-plant requirements.

- **Generation II** will focus on implementing a recuperated air-breathing microburner and the associated air delivery. The new microburner will be vacuum packaged with the photonic crystal emitter as in Generation I then demonstrated with existing TPV cells. This will be the first demonstration of a practical TPV microgenerator with experimentally measurable energy density.

Additional work refining and optimizing the Generation II microgenerator will be necessary to experimentally achieve the results from Chapter 5.

6.2.1 Generation I

High vacuum packaging is necessary to protect the photonic crystal from degradation during high temperature operation. While the current tantalum photonic crystal is resistant to physical degradation, it is highly susceptible to chemical degradation, particularly to carbon. Although a HfO_2 protective layer deposited by atomic layer deposition (ALD) has been shown to prevent degradation, a high vacuum environment is still required [121]. Ideally, the photonic crystal would be stable in a low vacuum environment sufficient only to prevent bulk oxidation and convective losses. Indeed, novel materials, alloys, and coatings should be investigated but the near-term solution is to design a high vacuum package that can prevent degradation of the current photonic crystal.

A high vacuum package containing the microburner, emitter, and cells would be challenging because the cells limit the bake-out temperature to ∼150°C, whereas one with only the microburner and emitter would require infrared transparent windows but would allow for a high temperature bake-out. Thus, we propose modifying the existing microburner frame concept to accept hermetically sealed windows on either side. The quartz or sapphire windows can be sealed by active brazing to compliant metal rings which are then welded to the frame. The view factor will degrade from the current $F = 0.90$ (1 mm gap) to around $F = 0.75$ (3 mm gap) to account for the microburner-window spacing, window thickness, and window-cell spacing. Additional cavity losses will be encountered due to reflection and absorption from the window. A multilayer stack could be deposited on the window to serve as both an antireflective coating and a cold side filter.

Generation I will use the current microburner with propane/nitrous oxide combustion. The exothermic decomposition of nitrous oxide more than counteracts the additional nitrogen in the exhaust stream, leading to a slight increase in microburner temperature compared to oxygen. Both propane (vapor pressure 8.5 atm at 20°C) and nitrous oxide (vapor pressure 50 atm at 20°C) can be liquefied under pressure, leading to dense storage. Furthermore, the entire fuel/oxidizer delivery can be passive: a manual valve will start the flow of reactants which will be metered through a high pressure drop pinhole orifices. Startup can be accomplished by the previously employed method of optical heating through the windows.

6.2.2 Generation II

Generation II will implement a recuperated air-breathing microburner. We propose a modular approach with the following new components:

- **Redesigned microburner.** The microburner will need to be modified to accommodate the increased flow rate: thickness will be increased to increase the residence time without modifying the combustion power density and the channels will be reconfigured for parallel flow to reduce pressure drop. Enough additional channel length should be added so that the microburner can reach the operating temperature without the recuperator by burning additional fuel. Larger diameter and shorter inlet and outlet tubes may be necessary to further reduce pressure drop. The tubes will likely need to be thermally isolated from housing to prevent heat loss. The microburner will be vacuum packaged using the approach from Generation I.

- **Recuperator.** An Inconel counterflow recuperator will need to be designed and fabricated. The target recuperator effectiveness is $\eta_{rec} = 0.7$ but the primary goal of this iteration will be a validation of modeling and a proof-of-concept of fabrication methods. The recuperator will be located outside vacuum chamber and insulate with conventional ceramic insulation in order to reduce the opportunity for leakage and outgassing as well as allow for easy access for instrumentation and modification.

- **Combustion air blower.** A blower, either centrifugal or piezoelectric, will be required to force atmospheric air through the recuperator and microburner. The pressure drop across all components must be kept to a minimum to ensure maximum net electrical power output. A Venturi powered by the vapor pressure of the propane could possibly pull the air through the recuperator and push the fuel/air mixture into the microburner. Although this approach offers reduced balance-of-plant load, it adds complexity and uncertainty to the design and reduces our design flexibility.

The microgenerator can be first tested with only the new microburner operated with external compressed air and additional fuel to compensate for the lack of recuperator. Startup can again be accomplished by optical heating through the windows. Next, the recuperator will

	Silicon system	Metallic system
Microburner	10 × 10 × 1.4 mm silicon 2× borosilicate (premixed feed) Microfabrication, glass brazing	20 × 20 × 4.2 mm Inconel 2–5× Inconel (segregated feed) Machining, welding
Emitters	(1) Bare silicon (2) Five-layer Si/SiO_2 stack	(1) Bare oxidized Inconel (2) 2D tantalum photonic crystal
Cells	1×1 InGaAsSb array	1×1 InGaAsSb array or 2×2 InGaAs array
Typical operation	<1 hour at 13 W and 800°C	135 hours at 60 W and 1000°C

Table 6.2: Parameters of the two experimental systems developed in this thesis.

be integrated and tested with compressed air. Finally the combustion air blower will be integrated for a self-contained microgenerator demonstration, although external power will be required both for ignition and to run the combustion air blower until the microgenerator becomes self sustaining.

6.3 Summary of results and contributions

In Chapter 1, we proposed a new approach to TPV fundamentally different than previous demonstrations. Our approach involves (1) an efficient, moderate temperature microburner, (2) a high emissivity, high selectivity photonic crystal emitter, and (3) low bandgap TPV cells. Over the course of this thesis we developed two experimental systems summarized in Table 6.2 that demonstrated the validity of our approach:

- **Silicon system.** We built a first-of-a-kind millimeter-scale TPV system with record fuel-to-electricity efficiency for that scale. The system used a simple Si/SiO_2 selective emitter deposited directly on a silicon MEMS microburner that doubled the fuel-to-electricity conversion efficiency relative to a bare silicon emitter. Many innovations in the packaging of the microburner were necessary.

- **Metallic system.** The silicon system was limited in its operating temperature and lifetime. We quantified these fundamental limitations, then proposed, designed, and demonstrated first-of-a-kind metallic system to address the shortcomings and improve

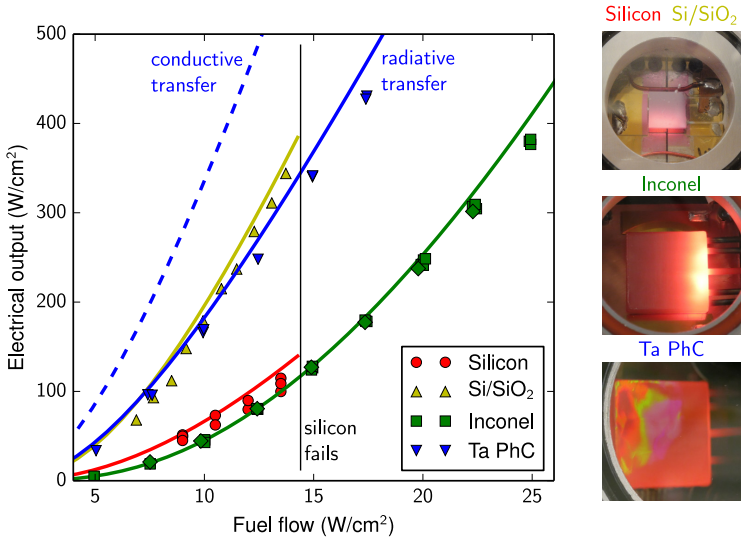

Figure 6-2: Measure (points) and simulated (lines) fuel to electricity conversion results for the silicon and metallic systems. The silicon system failed at about 14 W of fuel input whereas the metallic system could handle much higher temperatures.

stability and performance. We then integrated an a tantalum photonic crystal emitter for the first ever demonstration of a photonic crystal in a TPV system.

Our key experimental results are plotted in Fig. 6-2. The experimental work will have lasting impact beyond this thesis because the metallic system can serve as a robust platform for future TPV work and as a basis for a TPV microgenerator.

In addition to the experimental work, this thesis made modeling and simulation contributions:

- **TPV system model.** We developed a succinct model of the microburner, emitter, and cells to accurately predict microburner temperature and electrical power output, as well as where heat is lost throughout the fuel-to-electricity conversion process.

- **Cell and cooling model.** We developed a model to predict TPV cell efficiency as a function of temperature and a heat sink model to predict thermal resistance as a function of size and fan power. We coupled these two models to understand the trade off between heat-to-electricity conversion efficiency, heat sink mass, and fan power.

- **Microgenerator model.** We coupled the TPV system model and cooling model to predict the energy density of a complete TPV microgenerator. We also developed a framework for comparing microgenerator performance on different missions.

Through the TPV system and microgenerator modeling, we have contributed an understanding of how to design a high efficiency and high power density TPV system, the strengths and weaknesses of a TPV microgenerator, and the applications where one would be suitable. These models can serve as a framework for more detailed microgenerator-level models.

While not specific technical contributions, we wish to highlight four important but previously unmentioned "lessons learned" that permeate this work:

- **Understand system-level interactions.** This entire work is based on a system-level interaction that was either not understood or not explicitly stated in the literature: a high emissivity emitter is necessary for high efficiency, not just for high power density. Our ability to understand that interaction and concisely state it is derived from our analytical modeling, in this case the Norton equivalent circuit model.

- **Use analytical modeling.** We made extensive use of analytical modeling in this thesis, favoring it over numerical methods whenever possible. Simple analytical modeling offers insight and builds intuition, but cannot be accomplished when component-level complexity is carried into a system-level model—this is not only cumbersome but clouds important system-level interactions in unnecessary detail. Thus, we attempted to reduce components to "black boxes" whose behavior and interactions can be understood intuitively and expressed algebraically. For example, we reduced the TPV cells to a parameterized equivalent circuit, compressing the inner-workings of the cell into a handful of constants while maintaining accuracy.

- **Analyze failures.** No experiment works the first time, and the undesired results should receive the same rigorous treatment as the desired ones. When faced with failure we adopted a rigorous and analytical approach to identify the root cause, rather than the more common approach of applying essentially random variation in hopes of a favorable outcome. For example, repeatedly trying the same solder glass

with modifications to the application method and firing cycle, without supporting data or measurements, would be incredibly inefficient and even if successful would not result in any insight. It was fortunate that we rigorously analyzed the solder glass problem because it turned out to be unsolvable with our approach at the time.

- **Do not ignore interfaces.** In this thesis, we have seen two major examples of heterogeneous material interfaces not behaving as expected: the solder glass-silicon interface and the microburner-photonic crystal interface. In both cases, we assumed that our solution (glass solder or electron beam welding) would work and moved directly to a system-level experiment. In both cases we were wrong. Only when we studied the interface in isolation (to remove unnecessary complexity) did we gain insight and arrive at a solution. Thus, high temperature material interfaces should be avoided when possible, and when required they demand extra attention and characterization prior to a system-level experiment.

Even if nothing else is gained from this thesis, we hope that it can serve as a case study in these four valuable lessons.

Appendix A

Catalyst Washcoating

The catalyst was deposited by washcoating with a suspension of 5% Pt on γ-alumina, 325 mesh (Sigma Aldrich 311324), the final result is shown in Fig. A-1. The original procedure from Ref. 44 is summarized below:

1. The catalyst powder was mixed in a 10:1 weight ratio with water and ground in a mortar and pestle until it would remain in suspension for a few minutes, typically 30–60 minutes of grinding. The slurry was further diluted with water to 20:1. The catalyst suspension had a limited lifetime because the particles tended to conglomerate, but could be renewed by grinding for a few minutes.

2. The microburners were cleaned ultrasonically in acetone then rinsed with acetone and IPA and blown with nitrogen and dried on a hotplate at 80°C.

3. The catalyst suspension was injected into the microburner inlet with a syringe until it came out the outlet, filling the channel with catalyst suspension. It was dried flat at ∼80°C on a hotplate for one hour. The process was repeated and the microburner was dried on the opposite side. Excess catalyst was wiped from the outside of the microburner.

4. The microburner was weighed before and after catalyst loading, with ∼1 mg weight gain for silicon. An abnormally high weight usually indicated a clog and abnormally low weight indicated insufficient catalyst. For these cases, the catalyst was removed

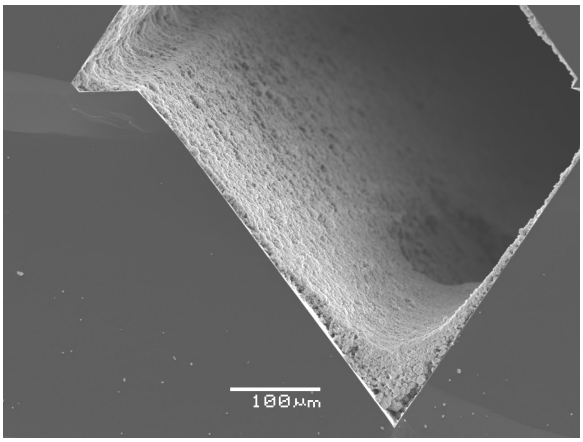

Figure A-1: Cross section of the silicon microburner showing the channel and catalyst. Note the misaligned wafers.

by these microburners ultrasonically and the process was repeated.

The high percentage of clogged reactor motivated refinement of the basic washcoat recipe by addition of an organic binder. The binder eliminated the need for grinding and improved consistency of catalyst dosage by keeping the particles in suspension longer. It also allowed us to blow out the channel before drying because the binder glued the catalyst to the walls. The improved procedure is as follows:

1. The catalyst powder was mixed in a 10 wt% suspension in a 2 wt% solution of a nitrocellulose (Ladd Research 10837) in amyl acetate (Sigma Aldrich W504009) for fast drying or diacetone alcohol (4-hydroxy-4-methyl-pentan-2-one, Sigma Aldrich H41544) for slow drying. No grinding was necessary.

2. The microburners were cleaned as before.

3. The catalyst suspension was injected into the channel with a syringe then immediately blown out with compressed air. A thin coating remained on the walls. In the case of the larger metallic system, the catalyst was collected and reused.

4. The microburner was heated to ∼100°C to dry the solvent. The drying temperature must be maintained below 180°C, at which point the nitrocellulose decomposes.

5. The microburners were weighted as before to determine the catalyst loading.

6. The binder was burned out by external heating to at least 350°C, which occurred during the glass soldering process for the silicon system. Nitrocellulose is an ideal binder because it decomposes into gaseous byproducts without air whereas other cellulose derivatives (hydroxyl ethyl cellulose, ethyl cellulose, methyl cellulose, etc.) tend to coke the catalyst.

The new nitrocellulose based catalyst is very versatile and the proportions of catalyst and binder can be tailored to the application.

Appendix B

Glass Soldering

The glass tubes were bonded to the silicon microburner with glass solder (Sem-Com SCC-7). The original procedure from Ref. 44 is summarized below:

1. Microburners and tubes were loaded into the stainless steel jig.

2. A paste of powdered glass and water was prepared by adding water drop-by-drop to the glass until a consistency of thin Plaster of Paris was reached. If too much or too little water was added, the solder glass would not seal properly. Throughout the process, it was necessary to add additional water to maintain the paste in a workable state.

3. The paste was applied to each joint with a fine wire and formed into a fillet. The paste quickly became unworkable and it was necessary to complete each joint in about 30 seconds.

4. The assembly was carefully loaded into a box furnace and the following heating cycle was executed: step to 350°Cand soak for 120 min, ramp 10°C/min to 690°C and soak for 120 min, ramp 1°C/min to 400°C, shut off the furnace.

This procedure suffered from low yield. We modified the procedure as follows:

1. The microburners and tubes were loaded into the jig as before. A 10% solution of nitrocellulose in ethyl acetate was used to glue everything in place. The assembly was baked at 80°C until dry.

2. A solution of 1 wt% solution of nitrocellulose in isophorone was added to the powdered glass in the same manor as before. The high boiling point of the solvent (215°C) extended the working time and the nitrocellulose provided mechanical strength to the dried paste. Nitrocellulose is the only suitable binder because it does not leave behind any residue upon decomposition. Residual carbon can reduce the lead oxide used in the braze to metallic lead.

3. The paste was applied to the joints as before.

4. A thin piano wire was inserted into each tube to clear any clogs. Because the tubes and microburners were glued to the jig, this did not disturb the joint.

5. The assembly was dried at ∼120°C. Cracks and voids can result if the solvent was not entirely removed from the joint before firing. The paste continued to flow during the drying process, so the assembly was dried upside down eliminate the possibility of clogging.

6. A thin piano wire was again inserted into each tube to check for clogs. The clog could not be cleared at this point but any defective microburners were noted.

7. The assembly was loaded into a box furnace and fired as described below.

The heating cycle is described below.

1. Step to 350°C and soak for 30 min. This step burned out the nitrocellulose binder. If not completely removed, trapped gases can cause voids or bubbles in the glass.

2. Ramp 10°C/min to 590°C and soak for 60 min. This step allowed the glass to sinter. The temperature was low enough that the glass does not devitrify but high enough to allow for flow.

3. Ramp 10°C/min to 680°C and soak for 60 min. This step devitrified the glass, transforming it to a glass-ceramic composite that remains solid above 680°C.

4. Allow to cool. The furnace was allowed to cool to room temperature with the door closed.

The new glass soldering procedure greatly improved the yield. Failed microburners could be recycled by etching the glass in either hot nitric acid or a mixture of hot hydrogen peroxide and acetic acid.

Appendix C

Metallic Microburner Fabrication

The microburner was fabricated by CNC machining at either the MIT Edgerton Student Shop or the Central Machine Shop according to the drawing in Fig. C-1. The five-tube microburner used both the body and the lit. The three-tube microburner used just the body and a piece of 1 mm thick Inconel for the lid. The holes for the tubing were drilled and reamed to a light press fit.

We added strain relief to the tubes to prevent damage during heating. (In a two-tube design, the microburner is free to rotate.) We bent a loop in all but two of the tubes for strain relief by bending the tube around progressively smaller cylinders to prevent kinking. Because the length changes during the bending process, tubes were cut over-sized then placed in a jig and ground to the desired length.

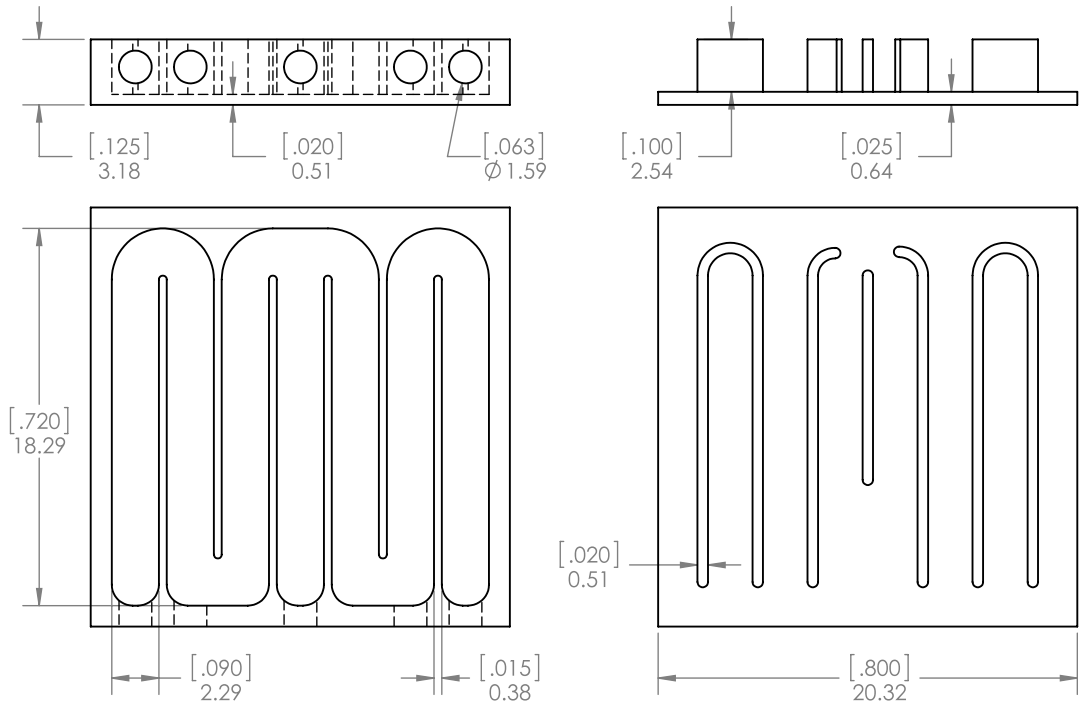

Figure C-1: Drawing of the microburner body (left) and lid (right) dimensioned in mm [inches].

Figure C-2: Machined microburner parts.

Appendix D

Cell Packaging

The cells for this work were hand selected from about 500 existing cells grown at Lincoln Labs. IV curves were measured for each growth run and the better runs were subject to more extensive characterization. Electrically, cells were selected for high shunt resistance and low series resistance. Mechanically, they were selected for being free of scratches and chips, and the metallization being well adhered and in good condition. Two sets of two matched cells from the same wafer and one set of four were selected and packaged by indium reflow soldering to a copper submount. Indium solder was necessary because the cells can be damaged by subjecting them to high temperatures.

D.1 Lincoln lab packaging

The copper substrates were first machined to size. They were cleaned and prepared for soldering according the the following procedure:

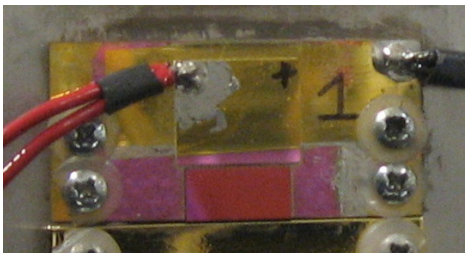

Figure D-1: Photograph of packaged GaInAsSb cell mounted on aluminum heat sink.

1. Rinse with acetone and methanol followed by water. Scrub with a Kimwipe in soapy water then rinse. Rinse with methanol and isopropanol and blow dry.

2. Soak 3–4 minutes in Shipley Neutraclean 68 copper cleaner. Rinse with water and scrub. Rinse with methanol and isopropanol and blow dry.

3. Ash both sides in oxygen plasma for 2 minutes.

4. RF preclean for 3 minutes then sputter 500 Å Ti, 1000 Å Pt, 500 Å Au.

A thicker layer of gold should be deposited for wire bonding. The metallized substrate except under the cell was masked with Kapton tape and 5 µm of indium was deposited by evaporation. The indium was reflowed in a vacuum oven with the cell held in place by a jig. The copper submount serves as the negative contact. The positive contact was a metallized ceramic pad, and contact was made to the cell's bus bar by wire bonding. Packaging was performed by Leo Missaggia at Lincoln Laboratory.

The following antireflective coating was deposited by Peter O'Brien at Lincoln Laboratory: (substrate) 38.63 nm TiO_2, 40.83 nm Ti, 146.95 nm TiO_2, 80.3 nm Al_2O_3, 31.14 nm TiO_2 (air).

D.2 MIT packaging

A second group of cells was packaged at MIT. A custom patterned copper core printed circuit board (PCB) was used as the substrate, and was supplied by Bergquist. The substrates were comprised of 0.040 inches copper followed by a 0.003 inch polymer dielectric layer followed by 0.0014 inch (1 oz.) copper with a Ni/Pd/Au metallization. The top copper layer was pattered to allow us to package two series-connected cells on a single substrate. The Ni/Pd/Au metallization allowed for gold wire bonding.

Some cells were packaged on unpatterned copper substrates. The copper was first machined to size then deburred. The surfaces were wet ground with 600 grit if needed. The substrate was cleaned ultrasonically in a detergent bath and rinsed with water. The copper was pickled in 18% nitric acid for about one minute until the surface was uniformly pink. Alternatively, a concentrated solution of Citranox was sometimes used. After pickling, the

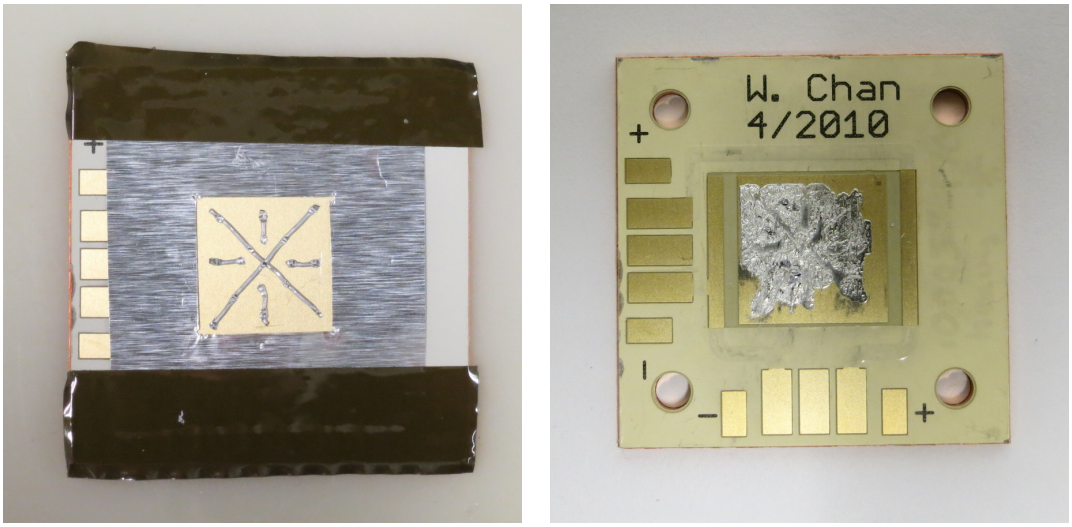

(a) Indium star and foil solder mask. (b) Flowed indium solder.

Figure D-2: An indium soldering test run for a 10×10 mm cell on a Bergquist substrate. The solder distribution can be tested with a glass or silicon dummy cell.

copper was rinsed thoroughly in deionized water and blown dry. The copper substrate was held by a copper wire threaded through one of the mounting holes.

Either wires or connectors were soldered to the Bergquist substrates before the cells. The substrate was preheated to about 100°C on a hotplate before soldering with ordinary lead-free solder. Flux was removed by ultrasonically cleaning in hexane then rinsing with hexane followed by isopropanol and blowing dry.

Indium wire was used for the solder preform. Indium foil was found to produce an inferior bond due to the higher surface area to volume ratio and resulting higher oxide content [122]. The indium was was first rinsed with acetone, methanol, and isopropanol then allowed to air dry. The wire was etched in 10% hydrochloric acid for about a minute until the surface changed from silver to matte grey. The wire was thoroughly rinsed in water followed by isopropanol and allowed to air dry [123]. We either used the indium immediately or stored it under hexane.

We formed an X or star on the pad from the etched indium wire. In the etched state, the indium could be easily cold welded to the Bergquist substrate. This type of shape was required because the air needed a path to escape as the indium melted and flowed to fill the entire pad [122]. The exact shape and length of wire was determined experimentally.

If the indium did not fill the entire pad, more wire was used. If the indium overflowed the pad, less indium was used. If the indium overflowed before filling the entire pad, a solder mask made from ordinary aluminum foil was used to contain the indium. Sample before and after reflow are shown in Fig. D-2.

The cells were carefully aligned and the assembly was loaded into a custom hot press in a nitrogen box. Weights were initially used but it was difficult to place them on the cells without disturbing the alignment. The press was weighted to apply a pressure of about 1 pound for a 1 cm^2 cell. The box was purged with nitrogen. The heater was turned on to 160°C and allowed to come up to temperature before being immediately turned off. The heater was cooled to room temperature with additional nitrogen flow before removing the packaged cell. Much of the lab work was carried out by Elaina Chai.

After soldering, the cells were wire bonded, either at MTL or by IDAX Microelectronics Lab.

The following antireflective coating was deposited on the InGaAsSb cells: (substrate) 20 nm Ta_2O_5, 97 nm Si, 152 nm Ta_2O_5, and 182 nm SiO_2 (air). The layer thicknesses were optimized by Peter Bermel assuming the cell structure was as follows: 500 nm GaSb doped at 10^{18} cm^{-3} for the window layer, 6 µm InGaAsSb doped at 5×10^{16} cm^{-3} for the base and emitter, and 1 mm GaSb doped at 5×10^{16} cm^{-3} for the substrate. The deposition was done at 4Wave by sputtering.

Appendix E

Temperature Dependent Cell Model

The cell model converts the optical spectrum incident on the cell into electrical power out and can be divided into two parts: the first converts incident photons into photocurrent using quantum efficiency (QE) and the second converts the photocurrent into a current-voltage (IV) curve using a circuit model. The IV curve serves as a complete electrical description of the DC behavior of the cell.

E.1 Quantum efficiency

Quantum efficiency is the ratio of photocurrent in electron charges to incident photon flux. By this definition the photocurrent is

$$I_{ph} = e \int_0^\infty \frac{\lambda}{hc} q_{ci}(\lambda) \mathrm{IQE}(\lambda) d\lambda, \tag{E.1}$$

where $q_{ci}(\lambda)$ is the radiated power per unit wavelength incident on the cell, hc/λ is the photon energy, IQE is the internal quantum efficiency from Fig. E-1 and e is the electron charge. There is a distinction between internal quantum efficiency (IQE) and external quantum efficiency (EQE). The former does not include the cell's reflectivity and the later

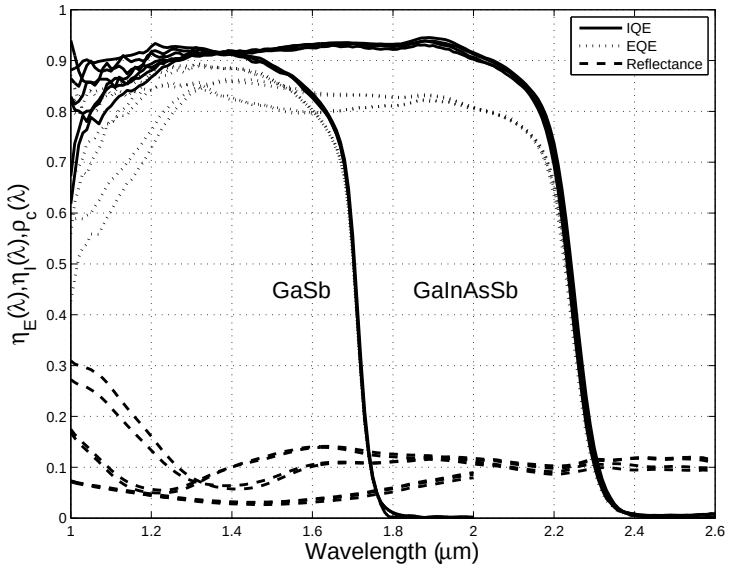

Figure E-1: Internal and external quantum efficiency and reflectivity measured at room temperature for GaSb and InGaAsSb cells. These data are not corrected for the effects of the bus bar.

does,

$$(\text{EQE}) = \rho_c(\text{IQE}). \tag{E.2}$$

We used the IQE in the above formula because q_{ci} already contains the cell's reflectivity.

An Optronics Labs OL750 monochromator with a QE accessory and a calibrated PbS detector was used to measure EQE and reflectivity simultaneously. Quantum efficiency was simply measured by illuminating the cell with monochromatic light of known intensity and measuring the short circuit current. Reflection was measured simultaneously by positioning the PbS detector to capture specular reflections from the cell. At the beginning of each measurement session, the monochromatic source was calibrated with the PbS detector.

When using a large spot size (1.5 mm), the front cell contact fingers cause an artificially low EQE and artificially high reflectivity because the cell has a fraction of its area, α, covered by gold fingers:

$$\text{EQE}' = (1-\alpha)\text{EQE} \tag{E.3}$$

$$\rho_c' = (1-\alpha)\rho_c + \alpha\rho_{Au} \tag{E.4}$$

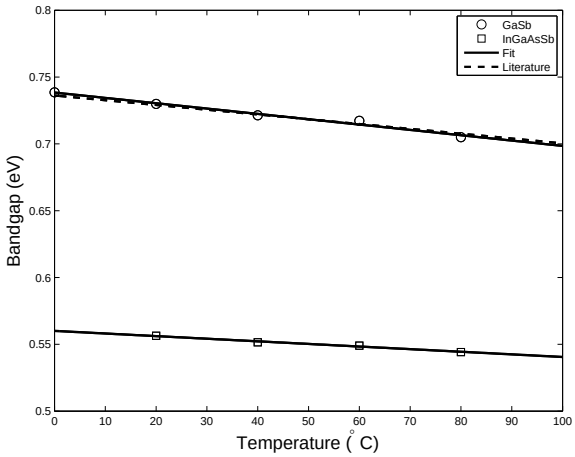

Figure E-2: Bandgap as a function of temperature.

The prime indicates a measured quantity and ρ_{Au} is the reflectivity of the gold fingers. The simplest way to handle this is to use the measured QE and the total cell area rather than the true QE and active area when calculating the photocurrent. Unless noted otherwise, this work uses the measured QE and reflectivity in all calculations.

Because TPV diodes operate with the majority of photons near the bandgap, a small change in bandgap can result in a substantial change in photocurrent. The bandgap of semiconductor materials depends on temperature approximately as

$$E_g(T) = E_g(0) - \frac{\alpha T^2}{T + \beta}, \tag{E.5}$$

where α and β are constants [124]. We measured quantum efficiency over temperature and extracted the bandgap from the inflection point in the absorption edge [125]. The temperature dependent bandgaps are shown if Fig. E-2. Because of the small temperature range, the bandgap narrowing was approximately linear; the results of the linear fit are presented in Table E.1. The temperature dependence of the GaSb bandgap agrees well with Ref. 126; whereas the values for our composition of InGaAsSb were not available in literature. To capture the temperature dependent bandgap concisely, the QE is approximated as a step function. For photon energies above the temperature dependent bandgap, the QE is approximated as its average value. Below the bandgap, it is approximated as zero.

To test the quantum efficiency measurements, the cells were illuminated with blackbody

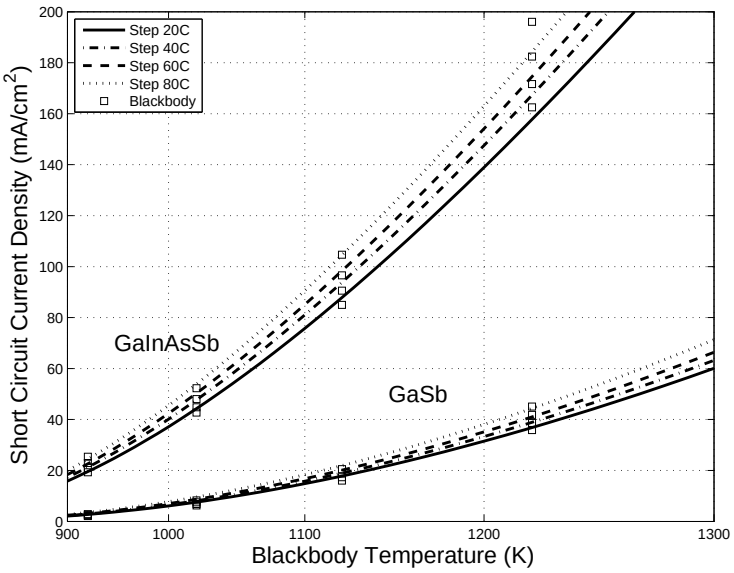

Figure E-3: Quantum efficiency verification. The cells were illuminated with blackbody radiation and the short circuit current was compared to that calculated with the QE. Note T^4 scaling on the x-axis.

radiation and the short circuit current was measured and reported in Fig. E-3. The photocurrent can be calculated from Eqn. E.1 assuming a blackbody source and no cold side filter in Eqn. 2.18. With these modifications, Eqn. E.1 reduces to

$$I_{ph} = eF \int_0^{\lambda_g(T_j)} \frac{\lambda}{hc} e_b(\lambda, T_e)\ \overline{\mathrm{EQE}}\ d\lambda, \tag{E.6}$$

where $\lambda_g(T_j)$ is the wavelength corresponding to the temperature dependent bandgap taken at the junction temperature, $e_b(\lambda, T_e)$ is the blackbody spectrum, and $\overline{\mathrm{EQE}}$ is the average value of the external quantum efficiency. We calculated the photocurrent due to blackbody radiation in Fig. E-3. With this model, we captured the increase in current due to increasing blackbody temperature because of σT_e^4 effects and because more of the spectrum is above the bandgap. We also captured the increase in current when the cell temperature increased and the bandgap decreased. Additionally, we see experimental that even a small change in bandgap can significantly change the photocurrent because many photons are near the bandgap.

E.2 Circuit model

The TPV cell can be described by the equivalent circuit in Fig. E-4a. The equivalent circuit for an externally illuminated photovoltaic cell consists of a current source representing the generated photocurrent and a diode with parasitic series and shunt resistances. If the photocurrent and all other component values are known then the terminal IV is

$$I = I_{ph} - I_0 \left(\exp \left[\frac{q}{n k_B T_j} (V + I R_s) \right] - 1 \right) - \frac{V + I R_s}{R_{sh}}, \tag{E.7}$$

where I and V are the terminal current and voltage, $q/k_B T_j$ is the thermal voltage, I_{ph} is the photocurrent, I_0 is the diode dark current, n is the diode ideality factor, and R_s and R_{sh} are the shunt and series resistances [41–43]. The solutions to Eqn. E.7 are Lambert-w functions although it is more straightforward to solve the equation numerically.

IV measurements were made in thermal steady state with a Keithley source meter. Photocurrents in excess of 2 A/cm^2 were provided by a 100 W quartz tungsten halogen lamp energized by a variable voltage power supply. The cells were mounted to a temperature controlled heat sink. Heat sink temperatures between 20°C and 80°C were measured with an embedded thermocouple and maintained by a thermoelectric element. We have made a full matrix of measurements over a temperature range and for all illumination levels. Due to the large volumes of data, we have only reported open circuit voltage (V_{oc}), short circuit current density (J_{sc}), and fill factor (FF) in Fig. E-5. Open circuit voltage and short circuit current are defined in Fig. E-4. Fill factor is the ratio of power at the maximum power point to the $V_{oc} I_{sc}$ product.

The five circuit parameters (I_{ph}, I_0, n, R_s, and R_{sh}) were found directly from experimental IV curves by fitting to Eq. E.7. The fitting process used MATLAB's `fminsearch` (implementing a Nelder-Mead simplex algorithm) to minimize a least squares error function. Accurate seeding values were required for the fit to converge. Seeding values were either extrapolated from previously fit data or estimated from limiting cases of the diode equation. For example, neglecting series and shunt resistance, the photocurrent is approximately the short circuit current. On the J_{sc}-V_{oc} plot, the slope is related to the ideality and the J_{sc}-intercept is related to the dark current. On individual IV curves, the horizontal asymptote

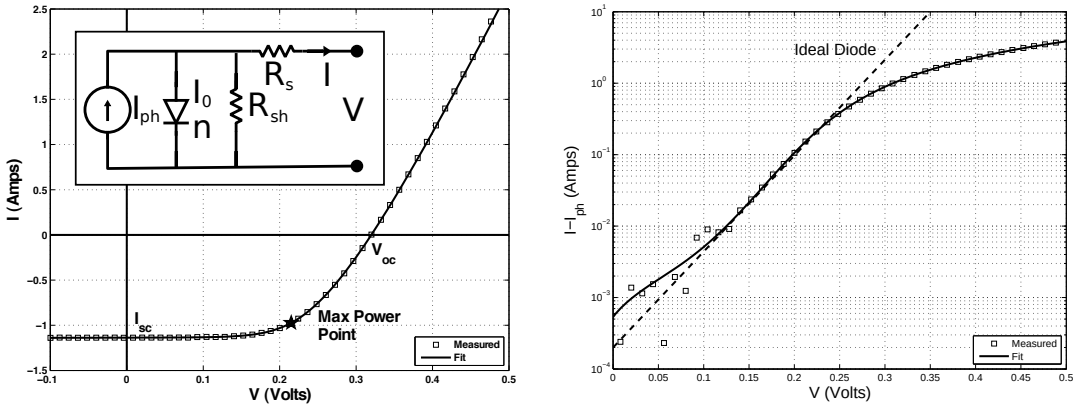

(a) Terminal IV curve

(b) Diode IV curve

Figure E-4: Electrical characteristics of a InGaAsSb cell under illumination. The terminal current-voltage relationship is presented on a linear scale in (a). The current through the diode is shown on a semilog scale in (b) in order to emphasize the ideal diode behavior of the cell (dotted line). The circuit inset in (a) is the equivalent circuit used in the model.

is the shunt resistance and the vertical asymptote is the series resistance. Data were fit on both linear and logarithmic scales. The linear fit in Fig. E-4a emphasizes photocurrent and the parasitic resistances; the logarithmic fit of the diode current ($I - I_{ph}$) in Fig. E-4b emphasizes the diode characteristics. Multiple passes on both axes are required to fine tune all five circuit parameters.

Once a large database of individual equivalent circuits was established (for each combination of cell temperature and illumination level), we reduced the data further by parameterizing the equivalent circuits. The goal is to be able to construct an equivalent circuit that is valid around a specified operating point defined by a photocurrent, I_{ph}, and junction temperature, T_j. A general relationship between the operating point and the circuit parameters is:

$$\begin{pmatrix} \ln(I_0) \\ n \\ R_s \\ R_{sh} \end{pmatrix} = \begin{pmatrix} M_{11} & M_{12} & M_{13} \\ M_{21} & M_{22} & M_{23} \\ M_{31} & M_{32} & M_{33} \\ M_{41} & M_{42} & M_{43} \end{pmatrix} \begin{pmatrix} 1 \\ I_{ph} \\ 1/T_j \end{pmatrix}, \tag{E.8}$$

where the circuit parameters are allowed to have linear dependencies on photocurrent and inverse junction temperature as well as a constant component.

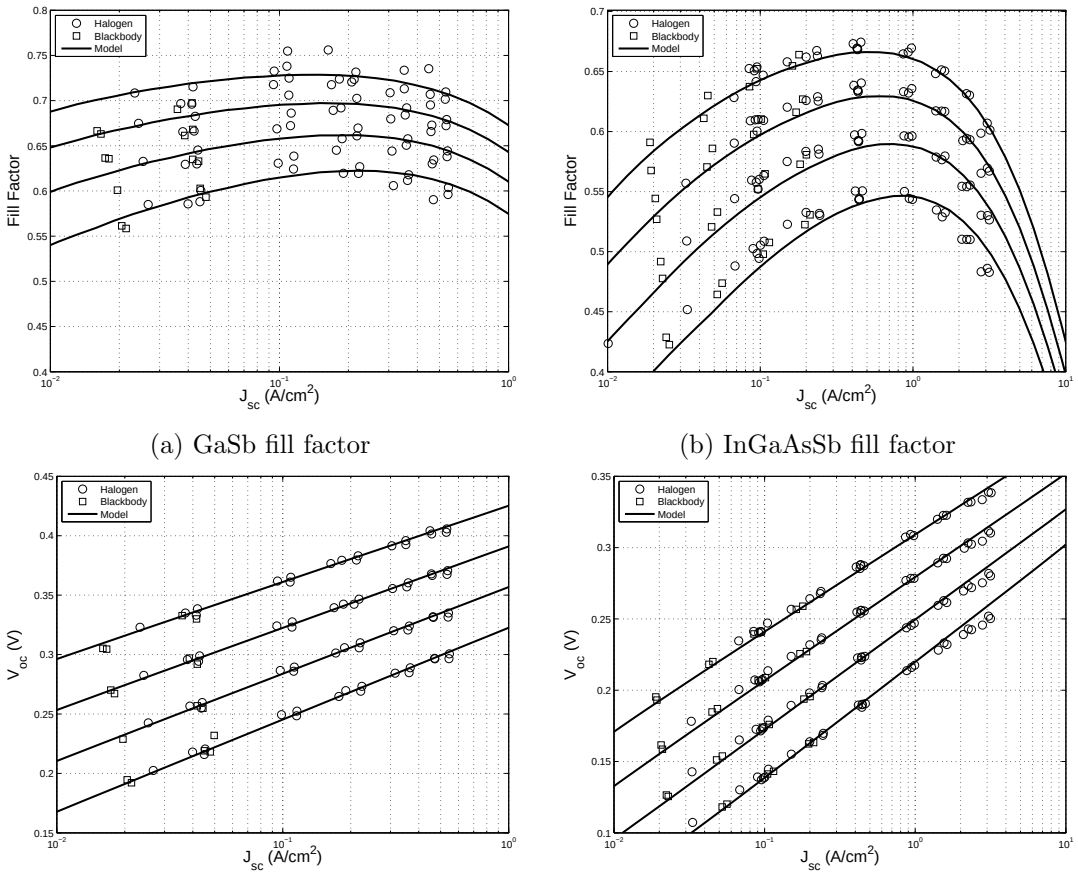

(a) GaSb fill factor

(b) InGaAsSb fill factor

(c) GaSb open circuit voltage

(d) InGaAsSb open circuit voltage

Figure E-5: Open circuit voltage and fill factor plotted against short circuit current density for GaSb and InGaAsSb cells. Model predictions are overlaid on blackbody and halogen measurements. This was done for cell temperatures of 20, 40, 60 and 80°C, ordered top to bottom in all plots.

The parameterization that will give minimum error between predicted and fit circuit parameters is when all elements of M are fit by least squares. While producing a good fit within the range of I_{ph} and T_j for which there is experimental data, this technique makes inaccurate predictions outside the range. Cell heating is at least partially responsible. We control the heat sink temperature, T_s, but the model depends on the junction temperature, T_j. The thermal resistance between the junction and heat sink is about 1.0 W/K for a packaged InGaAsSb cell and comparable for GaSb. At high photocurrents, the temperature difference can be appreciable, $T_j - T_s \approx 5°\text{C}$ for InGaAsSb cells. This was estimated from the sagging of the J_{sc}-V_{oc} data points in Fig. E-5d.

There is no simple method to eliminate the effects of cell heating when all entries of M are unknown: a change in one of the parameters and an increase in cell temperature are indistinguishable. The easiest fix is to force $M_{x2} = 0$ whenever M_{x3} is significant. Photocurrent dependence is ignored whenever a circuit parameter has a strong dependence on temperature. Thus, $M_{12} = 0$ because we know $I_0 \propto \exp(E_g/kT)$. Furthermore, we found that we could ignore the entire second and third columns of M except M_{13}. This simplification neglects certain second order effects. For example, ideality changes with operating conditions and was observed to slightly vary with the photocurrent [127].

From the equivalent circuits generated by the model, we calculated J_{sc}, V_{oc} and FF. The values of M that were used are listed in Table E.1. These results are plotted on top of the experimental data in Fig E-5. Overall, good agreement is achieved. The most notable fact about the fill factor graphs is that it has a maximum. The decrease in FF is due to the cell becoming series resistance limited. The photocurrent translates the dark IV curve down the voltage axis so far that the power producing quadrant only sees the series resistance asymptote. These considerations create an optimum photocurrent density to achieve maximum efficiency.

	InGaAsSb Cells (Lincoln Lab)				GaSb Cells (Fraunhofer)		
Cell No.	01-471-02	01-471-15	01-471-16	01-471-24	1544-41	1544-44	1544-45
$I_0(20°C)$ [μA]	10.8	14.8	11.6	15.1	0.438	0.284	0.376
M_{11}	12.74	13.91	14.09	13.45	17.86	20.16	17.33
M_{13}	-7085	-7333	-7459	-7191	-9522	-10322	-9412
n	1.123	1.171	1.135	1.155	1.106	1.098	1.104
R_s [mΩ]	29.9	30.5	34.9	34.0	31.0	23.2	38.9
R_{sh} [Ω]	204	210	372	1182	700	830	500
E_g [eV]	$0.5548 - (1.952 \times 10^{-4})(T - 300)$				$0.7276 - (3.990 \times 10^{-4})(T - 300)$		
QE	$\eta_I = 90\%$, $\eta_E = 82\%$				$\eta_I = 89\%$, $\eta_E = 86\%$		
Area	0.5 cm^2 total, 0.45 cm^2 active				1.55 cm^2 total, 1.40 cm^2 active		

Table E.1: Temperature dependent model parameters for InGaAsSb and GaSb cells. Dark current, I_0 depends on temperature as $\ln(I_0) = (M_{11} + M_{13}/T_j)$. All other electrical parameters are assumed to be constant. Quantum efficiency is approximated by a step function with a cutoff wavelength given by the bandgap, E_g, which is a function of temperature.

Appendix F

Heat Sink Model

Let us assume a fully ducted square heat sink with external length L_{hs}, width W_{hs}, base height H_{base}, and fin height H_{fin}. Each fin has width W_{fin} and the channels between fins is of width W_{ch}. The geometry is shown in Fig. 5-2. Furthermore, was assume flow of air over the fins with a free-stream volumetric flow rate of $\dot{v}$. Let the air have density ρ, kinematic viscosity ν, heat capacity c_p, thermal conductivity k_{air}. Let the heat sink material has a thermal conductivity k_{fin} and density ρ_{fin}.

We calculated the total thermal resistance of the heat sink shown in Fig. F-1 as the sum of the sum of the spreading resistance of the base plate and the base to air resistance:

$$\Theta_{tot} = \Theta_{sp} + \Theta_{hs} \tag{F.1}$$

where Θ_{sp} is the spreading resistance and Θ_{hs} is the heat sink resistance. The heat sink resistance is the sum of the resistance of the fin and the capacitive resistance of the air:

$$\Theta_{hs} = \frac{1}{\eta h A_s} + \frac{1}{c_p \rho \dot{v}} \tag{F.2}$$

where η is the is the heat sink efficiency, h is the heat transfer coefficient, and A_s is the

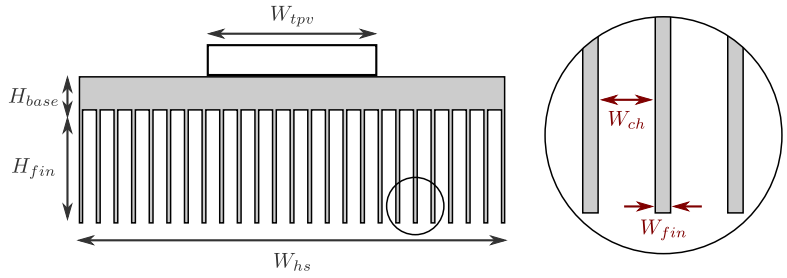

Figure F-1: The geometry of the heat sink. Dimensions to be optimized are shown in red.

heat sink's total surface area. Assuming $H_{fin} \gg W_{ch}$, the efficiency is approximated as

$$\begin{aligned} \eta &= \frac{\tanh\left(\sqrt{\frac{2h}{k_{fin}W_{fin}}}H_{fin}\right)}{\sqrt{\frac{2h}{k_{fin}W_{fin}}}H_{fin}} \\ h &= \frac{Nuk_{air}}{D_h} \\ Nu &= -1.047 + 9.326G \\ G &= \frac{\alpha^2+1}{(\alpha+1)^2} \end{aligned}$$

where Nu is the Nusselt number, and G is a geometric factor in terms of the aspect ratio of the channel $\alpha = W_{ch}/H_{fin}$ [128].

The spreading resistance was calculated with the non-dimensional geometry defined as

$$\epsilon = \frac{W_{tpv}}{W_{hs}} \tag{F.3}$$

$$\tau = \frac{H_{base}}{W_{hs}} \tag{F.4}$$

and where a and b are the radii of circles with areas equal to the TPV cell and heat sink, respectively. A closed-form approximation of the spreading resistance is

$$\begin{aligned} Bi &= \frac{1}{\pi\ k_{fin}\ b\ \Theta_{hs}} \\ \lambda &= \pi + \frac{1}{\epsilon\sqrt{\pi}} \\ \phi &= \frac{\tanh(\lambda\tau) + \lambda/Bi}{1 + \tanh(\lambda\tau)\lambda/Bi} \end{aligned}$$

$$\begin{aligned} \Psi &= \frac{\epsilon\tau}{\sqrt{\pi}} + \frac{1}{2}\phi(1-\epsilon)^{3/2} \\ \Theta_{sp} &= \frac{\Psi}{k_{fin}\ a\ \sqrt{\pi}}. \end{aligned}$$

according to Ref. 129.

From a fluid mechanics perspective, we modeled the heat sink as a tube. The pressure drop, Δp_{hs}, across the heat sink is given by the Darcy-Weisbach equation,

$$\Delta p_{hs} = f\frac{L_{hs}}{D_h}\frac{\rho u^2}{2} \tag{F.5}$$

$$u = \frac{\dot{v}}{nW_{ch}H_{fin}} \tag{F.6}$$

$$D_h = 2\frac{W_{ch}H_{fin}}{W_{ch}+H_{fin}} \tag{F.7}$$

where f is the friction factor, D_h is the hydraulic diameter of the channel, u is the air velocity in the heat sink, and n is the number of channels. We used the friction factor given in Ref. 128:

$$f = 4\frac{4.70 + 19.64G}{Re} \tag{F.8}$$

$$Re = \frac{uD_h}{\nu} \tag{F.9}$$

where Re is the Reynolds number and G is the geometric factor in Eqn. F.3. This model was validated by comparison to experimental data given in the literature [128]. Additional terms can be added to Equation F.5 to account for the abrupt change in cross section when entering and leaving the heat sink. We chose to neglect these terms for simplicity.

The pumping power required to move air across the heat sink is given by

$$P_p = \Delta p\, \dot{v}. \tag{F.10}$$

In reality, the electrical power required to drive the fan depends on many additional factors. For simplicity, we will assume that the fan has a constant efficiency.

Bibliography

[1] Committee on Electric Power for the Dismounted Soldier, *Energy-Efficient Technologies for the Dismounted Soldier*. National Academies Press, 1997.

[2] Committee on Soldier Power/Energy Systems, *Meeting the Energy Needs of Future Warriors Committee*. National Academies Press, 2004.

[3] R. Decher, *Direct energy conversion : fundamentals of electric power production*. New York: Oxford University Press, 1997.

[4] N. S. Lewis, "Portable Energy for the Dismounted Soldier," Tech. Rep. JSR-02-135, Office of Defense Research and Engineering, 2003.

[5] A. Mitsos, *Microfabricated power generation devices : design and technology*. Weinheim: Wiley-VCH, 2009.

[6] Horizon fuel cells. `http://www.horizonfuelcell.com/#!minipak/c156u`. Accessed 2015-02-23.

[7] M. Hanlon, "At last! an affordable, portable, pocket-sized personal fuel cell." `http://www.gizmag.com/at-last-an-affordable-portable-pocket-size-fuel-cell/15425/`, 2010. Accessed 2015-03-07.

[8] B. Wernsman, R. R. Siergiej, S. D. Link, R. G. Mahorter, M. N. Palmisiano, R. J. Wehrer, R. W. Schultz, G. P. Schmuck, R. L. Messham, S. Murray, C. S. Murray, F. Newman, D. Taylor, D. M. Depoy, and T. Rahmlow, "Greater Than 20% Radiant Heat Conversion Efficiency of a Thermophotovoltaic Radiator/Module System Using

Reflective Spectral Control," *IEEE Transactions on Electron Devices*, vol. 51, pp. 512–515, Mar. 2004.

[9] M. Zenker and a. Heinzel, "Efficiency and power density potential of combustion-driven thermophotovoltaic systems using GaSb photovoltaic cells," *IEEE Transactions on Electron Devices*, vol. 48, no. 2, pp. 367–376, 2001.

[10] P. L. Adair, *Design and fabrication of a thermophotovoltaic power generation unit.* PhD thesis, Auburn University, 1997.

[11] E. M. West and W. R. Connelly, "Integrated development and testing of multi-kilowatt TPV generator systems," vol. 446, pp. 446–456, 1999.

[12] K. C. Chen, D. Osborn, R. Sarmiento, A. Prasad, and S. Earath, "Small , Efficient Thermophotovoltaic Power Supply," Tech. Rep. DAAG55-97-C-0003, U.S. Army Research Office, 1999.

[13] L. M. Fraas, "Small efficient thermophotovoltaic power supply using infrared-sensitive gallium antimonide cells," Tech. Rep. DAAG55-97-C-0002, U.S. Army Research Office, 1999.

[14] E. Doyle, K. Shukla, and C. Metcalfe, "Development and Demonstration of a 25 Watt Thermophotovoltaic Power Source for a Hybrid Power System," Tech. Rep. TR04-2001, National Aeronautics and Space Administration, 2001.

[15] R. E. Nelson, "TPV systems and state-of-art development," in *Fifth Conference on Thermophotovoltaic Generation of Electricity* (T. J. Coutts, G. Guazzoni, and J. Luther, eds.), vol. 653 of *American Institute of Physics Conference Series*, pp. 3–17, 2003.

[16] O. M. Nielsen, L. R. Arana, C. D. Baertsch, K. F. Jensen, and M. A. Schmidt, "A thermophotovoltaic micro-generator for portable power applications," in *Transducers, Solid-State Sensors, Actuators and Microsystems, 12th International Conference on, 2003*, vol. 1, pp. 714–717, June 2003.

[17] T. Aicher, P. Kästner, A. Gopinath, A. Gombert, A. W. Bett, T. Schlegl, C. Hebling, and J. Luther, "Development of a Novel TPV Power Generator," *AIP Conference Proceedings*, vol. 738, no. 1, pp. 71–78, 2004.

[18] C. J. Astle, *Design and testing of a prototype thermophotovoltaic system.* PhD thesis, University of Alberta, 2004.

[19] Y. Wenming, C. Siawkiang, S. Chang, X. Hong, and L. Zhiwang, "Research on micro-thermophotovoltaic power generators with different emitting materials," *Journal of Micromechanics and Microengineering*, vol. 15, no. 9, pp. S239–S242, 2005.

[20] B. Bitnar, W. Durisch, and R. Holzner, "Thermophotovoltaics on the move to applications," *Applied Energy*, vol. 105, no. 0, pp. 430–438, 2013.

[21] W. R. Chan, P. Bermel, R. C. N. Pilawa-Podgurski, C. H. Marton, K. F. Jensen, J. J. Senkevich, J. D. Joannopoulos, M. Soljacic, and I. Celanovic, "Toward high-energy-density, high-efficiency, and moderate-temperature chip-scale thermophotovoltaics," *Proceedings of the National Academy of Sciences*, vol. 110, no. 14, pp. 5309–5314, 2013.

[22] A. Licciulli, D. Diso, G. Torsello, S. Tundo, A. Maffezzoli, M. Lomascolo, and M. Mazzer, "The challenge of high-performance selective emitters for thermophotovoltaic applications," *Semiconductor Science and Technology*, vol. 18, no. 5, p. S174, 2003.

[23] H. F. Ivey, "Candoluminescence and radical-excited luminescence," *Journal of Luminescence*, vol. 8, no. 4, pp. 271–307, 1974.

[24] H. H. Kolm, "Solar-battery power source," Tech. Rep. Group 35, MIT-Lincoln Laboratory, 1956.

[25] B. D. Wedlock, "Thermo-photo-voltaic conversion," *Proc. IEEE*, vol. 51, pp. 694–698, 1963.

[26] R. E. Nelson, "A brief history of thermophotovoltaic development," *Semiconductor Science and Technology*, vol. 18, no. 5, p. S141, 2003.

[27] T. J. Coutts, M. W. Wanlass, J. S. Ward, and S. Johnson, "A review of recent advances in thermophotovoltaics," in *Photovoltaic Specialists Conference, 1996., Conference Record of the Twenty Fifth IEEE*, pp. 25–30, May 1996.

[28] G. E. Guazzoni, "High- temperature spectral emittance of oxides of erbium, samarium, neodymium and ytterbium," *Applied Spectroscopy*, vol. 26, pp. 60–65, Jan. 1972.

[29] W. Durisch, B. Bitnar, F. von Roth, and G. Palfinger, "Small thermophotovoltaic prototype systems," *Solar Energy*, vol. 75, no. 1, pp. 11–15, 2003.

[30] A. Heinzel, V. Boerner, A. Gombert, B. Blasi, V. Wittwer, and J. Luther, "Radiation filters and emitters for the NIR based on periodically structured metal surfaces," *J. Mod. Opt.*, vol. 47, 2000.

[31] J. M. Gee, J. B. Moreno, S.-Y. Lin, and J. G. Fleming, "Selective emitters using photonic crystals for thermophotovoltaic energy conversion," in *Twenty-ninth IEEE Photovolt. Spec. Conf.*, pp. 896–899, May 2002.

[32] H. Sai, Y. Kanamori, and H. Yugami, "High-temperature resistive surface grating for spectral control of thermal radiation," *Appl. Phys. Lett.*, vol. 82, pp. 1685–1687, 2003.

[33] U. Ortabasi and B. Bovard, "Rugate technology for thermophotovoltaic applications: a new approach to near perfect filter performance," *AIP Conf. Proc.*, vol. 653, pp. 249–258, 2003.

[34] F. O'Sullivan, I. Celanovic, N. Jovanovic, J. Kassakian, S. Akiyama, and K. Wada, "Optical characteristics of one-dimensional Si/SiO2 photonic crystals for thermophotovoltaic applications," *Journal of Applied Physics*, vol. 97, no. 3, 2005.

[35] D. L. C. Chan, I. Celanovic, J. D. Joannopoulos, and M. Soljacic, "Emulating one-dimensional resonant Q-matching behavior in a two-dimensional system via Fano resonances," *Phys. Rev. A*, vol. 74, p. 64901, 2006.

[36] T. D. Rahmlow, D. M. DePoy, P. M. Fourspring, H. Ehsani, J. E. Lazo-Wasem, and E. J. Gratrix, "Development of front surface, spectral control filters with greater

temperature stability for thermophotovoltaic energy conversion," in *Seventh World Conference on Thermophotovoltaic Generation of Electricity* (C. Algora and V. Corregidor, eds.), pp. 59–67, American Institute of Physics, 2007.

[37] I. Celanovic, N. Jovanovic, and J. Kassakian, "Two-dimensional tungsten photonic crystals as selective thermal emitters," *Applied Physics Letters*, vol. 92, no. 19, p. 193101, 2008.

[38] P. Bermel, M. Ghebrebrhan, W. Chan, Y. X. Yeng, M. Araghchini, R. Hamam, C. H. Marton, K. F. Jensen, M. Soljacic, J. D. Joannopoulos, S. G. Johnson, and I. Celanovic, "Design and global optimization of high-efficiency thermophotovoltaic systems," *Opt. Express*, vol. 18, pp. A314–A334, 2010.

[39] W. R. Chan, R. Huang, C. A. Wang, J. Kassakian, J. D. Joannopoulos, and I. Celanovic, "Modeling low-bandgap thermophotovoltaic diodes for high-efficiency portable power generators," *Sol. Energy Mater. Sol. Cells*, vol. 94, pp. 509–514, 2010.

[40] M. F. Modest, *Radiative Heat Transfer*. McGraw-Hill, 1993.

[41] J. Charles, I. Mekkaoui-Alaoui, and G. Bordure, "A critical study of the effectivelness of the singe and double exponential models for IV characterization of solar cells," *Solid State Electronics*, vol. 28, no. 8, pp. 807–820, 1985.

[42] M. Chegaar, Z. Ouennoughi, and A. Hoffmann, "A new method for evaluating illuminated solar cell parameters," *Solid State Electronics*, vol. 45, pp. 293–296, 2001.

[43] S. Hegedus, "Current-voltage analysis of a-Si and a-SiGe solar cells including voltage-dependant photocurrent collection," 1997.

[44] B. S. Blackwell, *Design, fabrication, and characterization of a micro fuel processor*. PhD thesis, Massachusetts Institute of Technology, 2008.

[45] L. R. Arana, S. B. Schaevitz, A. J. Franz, M. A. Schmidt, and K. F. Jensen, "A microfabricated suspended-tube chemical reactor for thermally efficient fuel processing," *Microelectromechanical Systems, Journal of*, vol. 12, no. 5, pp. 600–612, 2003.

[46] M. Araghchini, *Efficient silicon micro-reactors for thermophotovoltaic applications.* Electrical engineer's thesis, Massachusetts Institute of Technology, 2011.

[47] S. Brown, *Thermal emission measurement and calibration.* Bachelor's thesis, Massachusetts Institute of Technology, 2009.

[48] Y. X. Yeng, *Photonic crystals for high temperature applications.* PhD thesis, Massachusetts Institute of Technology, 2014.

[49] R. C. N. Pilawa-Podgurski, N. A. Pallo, W. R. Chan, D. J. Perreault, and I. L. Celanovic, "Low-power maximum power point tracker with digital control for thermophotovoltaic generators," in *Applied Power Electronics Conference and Exposition (APEC), 2010 Twenty-Fifth Annual IEEE*, pp. 961–967, 2010.

[50] R. C. N. Pilawa-Podgurski, W. Li, I. Celanovic, and D. J. Perreault, "Integrated CMOS DC-DC converter with digital maximum power point tracking for a portable thermophotovoltaic power generator," in *Energy Conversion Congress and Exposition (ECCE), 2011 IEEE*, pp. 197–204, 2011.

[51] S. P. Murarka, *Silicides for VLSI applications.* New York: Academic Press, 1983.

[52] V. Rinnerbauer, J. J. Senkevich, J. D. Joannopoulos, M. Soljacic, I. Celanovic, R. R. Harl, and B. R. Rogers, "Low emissivity high-temperature tantalum thin film coatings for silicon devices," *Journal of Vacuum Science & Technology A*, vol. 31, no. 1, pp. –, 2013.

[53] D. W. A. Forbes, "Solder glass seals in semi-conductor packaging," *Glass Technology*, vol. 8, no. 2, 1967.

[54] T. H. Ramsey, "Thermal and X-Ray analyses of some electronic package sealing glasses," *Ceramic Bulletin*, vol. 50, no. 8, pp. 671–675, 1971.

[55] R. G. Frieser, "A review of solder glass," *Electrocomponent Science and Technology*, vol. 2, pp. 163–199, 1975.

[56] J. H. Partridge, *Glass-To-Metal Seals*. Sheffield: The Society of Glass Technology, 1949.

[57] C. A. Swenson, "Recommended values for the thermal expansivity of silicon from 0 to 1000 K," *Journal of Physical and Chemical Reference Data*, vol. 12, no. 2, 1983.

[58] T. S. Harrison, "Packaging of the MIT microengine," Master's thesis, Massachusetts Institute of Technology, 2000.

[59] V. Stelmakh, V. Rinnerbauer, J. D. Joannopoulos, M. Soljacic, I. Celanovic, J. J. Senkevich, C. Tucker, T. Ives, and R. Shrader, "Evolution of sputtered tungsten coatings at high temperature," *Journal of Vacuum Science & Technology A*, vol. 31, no. 6, pp. –, 2013.

[60] D. Kirikae, Y. Suzuki, and N. Kasagi, "A silicon microcavity selective emitter with smooth surfaces for thermophotovoltaic power generation," *Journal of Micromechanics and Microengineering*, vol. 20, no. 10, p. 104006, 2010.

[61] A. C. Fernandez-Pello, "Micropower generation using combustion: Issues and approaches," *Proceedings of the Combustion Institute*, vol. 29, no. 1, pp. 883–899, 2002.

[62] N. S. Kaisare, S. R. Deshmukh, and D. G. Vlachos, "Stability and performance of catalytic microreactors: Simulations of propane catalytic combustion on Pt," *Chemical Engineering Science*, vol. 63, no. 4, pp. 1098–1116, 2008.

[63] C. L. Yaws, L. Bu, and K. Y. Li, "Diffusion coefficients in air," in *Handbook of transport property data : viscosity, thermal conductivity, and diffusion coefficients of liquids and gases* (C. L. Yaws, ed.), Houston, Tex: Gulf Pub. Co, 1995.

[64] W. R. Chan, B. A. Wilhite, J. J. Senkevich, M. Soljacic, J. Joannopoulos, and I. Celanovic, "An all-metallic microburner for a millimeter-scale thermophotovoltaic generator," *Journal of Physics: Conference Series*, vol. 476, no. 1, p. 12017, 2013.

[65] C. K. Westbrook and F. L. Dryer, "Simplified reaction mechanisms for the oxidation of hydrocarbon fuels in flames," *Combustion Science and Technology*, vol. 27, no. 1-2, pp. 31–43, 1981.

[66] C. R. Wilke, "A viscosity equation for gas mixtures," *The Journal of Chemical Physics*, vol. 18, no. 4, pp. 517–519, 1950.

[67] R. Bird, *Transport phenomena*. New York: J. Wiley, 2007.

[68] E. N. Fuller, P. D. Schettler, and J. C. Giddings, "New method for prediction of binary gas-phase diffusion coefficients," *Industrial & Engineering Chemistry*, vol. 58, no. 5, pp. 18–27, 1966.

[69] D. G. Vlachos, L. D. Schmidt, and R. Aris, "Ignition and extinction of flames near surfaces: Combustion of H2 in air," *Combustion and Flame*, vol. 95, no. 3, pp. 313–335, 1993.

[70] C. M. Miesse, R. I. Masel, C. D. Jensen, M. A. Shannon, and M. Short, "Submillimeter-scale combustion," *AIChE Journal*, vol. 50, no. 12, pp. 3206–3214, 2004.

[71] M. G. Zabetakis, *Flammability characteristics of combustible gases and vapors*. Bureau of Mines, 1965.

[72] V. Stelmakh, V. Rinnerbauer, R. D. Geil, P. R. Aimone, J. J. Senkevich, J. D. Joannopoulos, M. Soljacic, I. Celanovic, M. Soljačić, and I. Celanovic, "High-temperature tantalum tungsten alloy photonic crystals: Stability, optical properties, and fabrication," *Applied Physics Letters*, vol. 103, no. 12, pp. 0–4, 2013.

[73] American Welding Society, *Brazing handbook*. Miami, FL: American Welding Society, 2007.

[74] P. F. Baldasaro, J. E. Raynolds, G. W. Charache, D. M. DePoy, C. T. Ballinger, T. Donovan, and J. M. Borrego, "Thermodynamic analysis of thermophotovoltaic efficiency and power density tradeoffs," *Journal of Applied Physics*, vol. 89, no. 6, pp. 3319–3327, 2001.

[75] Y. X. Yeng, W. R. Chan, V. Rinnerbauer, J. D. Joannopoulos, and I. Celanovic, "Performance analysis of experimentally viable photonic crystal enhanced thermophotovoltaic systems," *Optics Express*, vol. 21, no. S6, pp. 2879–2891, 2013.

[76] W. R. Allmon, C. M. Waits, and E. D. Tolmachoff, "Heat recuperator engineering for an ARL liquid-fueled thermophotovoltaic power source demonstrator," Tech. Rep. ARL-TR-711, Army Research Laboratory, 2014.

[77] T. Nagasaki, R. Tokue, S. Kashima, and Y. Ito, "Conceptual design of recuperator for ultramicro gas turbine," in *Proceedings of the International Gas Turbine Congress*, 2003.

[78] M. Olivero, *From turbocharger to micro gas turbine applications.* PhD thesis, Delft University of Technology, 2012.

[79] C. H. Marton, *An Air-Breathing, Portable Thermoelectric Power Generator Based on a Microfabricated Silicon Combustor.* PhD thesis, Massachusetts Institute of Technology, 2011.

[80] C. H. Marton, G. S. Haldeman, and K. F. Jensen, "Portable Thermoelectric Power Generator Based on a Microfabricated Silicon Combustor with Low Resistance to Flow," *Industrial & Engineering Chemistry Research*, vol. 50, no. 14, pp. 8468–8475, 2011.

[81] I. P. Prikhodko, B. R. Simon, G. Sharma, S. a. Zotov, A. a. Trusov, and A. M. Shkel, "High and moderate-level vacuum packaging of vibratory MEMS," in *International Symposium on Microelectronics*, pp. 705–710, 2013.

[82] W. R. Chan, C. M. Waits, J. D. Joannopoulos, and I. Celanovic, "Thermophotovoltaic and thermoelectric portable power generators," in *Proc. SPIE*, vol. 9083, pp. 90831W–8, 2014.

[83] D. Sabatino and K. Yoder, "Pyrolytic graphite heat sinks: a study of circuit board applications," *Components, Packaging and Manufacturing Technology, IEEE Transactions on*, vol. 4, pp. 999–1009, June 2014.

[84] T. Rahmlow, J. Lazo-Wasem, and E. Gratrix, "Front surface tandem filters using sapphire (Al2O3) substrates for spectral control in thermophotovoltaic energy conversion systems," Tech. Rep. LM-05K032, US Department of Energy, 2005.

[85] P. M. Fourspring, D. M. DePoy, T. D. Rahmlow, J. E. Lazo-Wasem, and E. J. Gratrix, "Optical coatings for thermophotovoltaic spectral control," *Appl. Opt.*, vol. 45, no. 7, pp. 1356–1358, 2006.

[86] T. D. Rahmlow, D. M. DePoy, P. M. Fourspring, H. Ehsani, J. E. Lazo-Wasem, and E. J. Gratrix, "Development of front surface, spectral control filters with greater temperature stability for thermophotovoltaic energy conversion," in *Seventh World Conference on Thermophotovoltaic Generation of Electricity* (C. Algora and V. Corregidor, eds.), pp. 59–67, American Institute of Physics, 2007.

[87] R. T. Kristensen, J. F. Beausang, and D. M. DePoy, "Frequency selective surfaces as near-infrared electromagnetic filters for thermophotovoltaic spectral control," *Journal of Applied Physics*, vol. 95, no. 9, pp. 4845–4851, 2004.

[88] Y. X. Yeng, J. B. Chou, V. Rinnerbauer, Y. Shen, S.-G. Kim, J. D. Joannopoulos, M. Soljacic, and I. Čelanović, "Global optimization of omnidirectional wavelength selective emitters/absorbers based on dielectric-filled anti-reflection coated two-dimensional metallic photonic crystals," *Optics Express*, vol. 22, no. 18, p. 21711, 2014.

[89] J. B. Chou, Y. X. Yeng, A. Lenert, V. Rinnerbauer, I. Celanovic, M. Soljačić, E. N. Wang, and S.-G. Kim, "Design of wide-angle selective absorbers/emitters with dielectric filled metallic photonic crystals for energy applications.," *Optics express*, vol. 22 Suppl 1, no. January, pp. A144–54, 2014.

[90] T. Christen and M. W. Carlen, "Theory of Ragone plots," *Journal of Power Sources*, vol. 91, no. 2, pp. 210–216, 2000.

[91] B. Dodson, "Miniaturized butane fuel cell system enables new USB battery charger,"

[92] MyFC. `http://www.powertrekk.com/`. Accessed 2015-02-23.

[93] T. Sookdeo, *Performance Measurment, Simulation, and Analysis of the Cox Tee Dee 0.010, the World's Smallest Production Internal Combustion Engine.* Master's thesis, University of Maryland, College Park, 2006.

[94] A. H. Epstein, "Millimeter-scale MEMS gas turbine engines," in *Proceedings of ASME Turbo Expo*, vol. GT-2003-38, 2003.

[95] W. J. A. Dahm, J. Ni, K. Mijit, R. Mayor, G. Qiao, A. Benajmin, Y. Gu, Y. Lei, and M. Papke, "Micro Internal Combustion Swing Engine (MICSE) for Portable Power Generation Systems," in *AIAA Aerospace Sciences Meeting*, 2002.

[96] A. Gomez, J. Berry, S. Roychoudhury, and J. Huth, "Palm power: using vombustion at small scales and a free piston stirling engine to replace batteries," in *International Mechanical Engineering Congress and of Exposition*, Nov. 2005.

[97] C. Teleki, "45-Watt thermoelectric generator," in *17th Annual Power Sources Conference*, pp. 31–33, 1963.

[98] O. Dessornes, S. Landais, R. Valle, A. Fourmaux, S. Burguburu, C. Zwyssig, and Z. Kozanecki, "Advances in the development of a microturbine engine," *Journal of Engineering for Gas Turbines and Power*, vol. 136, no. 7, p. 071201, 2014.

[99] T. M. Corry and G. Spira, "Thermoelectric generator design, performance, and application," *IRE Transactions on Military Electronics*, vol. MIL-6, no. 1, pp. 34–40, 1962.

[100] T. M. Corry, W. C. Moreland, and E. L. Strickland, "Design of a 100-watt thermoelectric generator," *Electrical Engineering*, vol. 79, pp. 482–488, June 1960.

[101] Protonex, "P200i." `http://www.protonex.com/products/p200i/`. Accessed 2015-04-21.

[102] Ultra Electronics AMI. `http://www.ultra-ami.com/portable-power-fuel-cell-products/roamio-defender-series/`. Accessed 2015-02-23.

[103] J. P. Angello and G. R. Frysinger, "Military multifuel thermoelectric generators," *SAE Technical Paper 680394*, 1968.

[104] Protonex, "M300-CX." `http://www.protonex.com/products/m300/`. Accessed 2015-04-21.

[105] A. Neild, "Thermoelectric generators for military portable oower," *SAE Technical Paper 670452*, 1967.

[106] J. C. Bass, "Preliminary design of a miniature thermoelectric generator," Tech. Rep. DAAK70-93-C-0062, US Army, Apr. 2007.

[107] Honda Power Equipment. `http://powerequipment.honda.com/generators/models/eu1000i`. Accessed 2015-02-23.

[108] H. Kumakura, H. Maekawa, and K. Murakami, "Development of portable gas turbine generator Dynajet 2.6," *IHI engineering review*, vol. 37, no. 3, pp. 113–114, 2004.

[109] A. J. Knobloch, M. Wasilik, C. Fernandez-Pello, and A. P. Pisano, "Micro internal-combustion engine fabrication with 900 μm deep features via DRIE," in *2003 ASME International Mechanical Engineering Congress*, vol. 5, pp. 1–9, 2015.

[110] D. Feroldi and M. Basualdo, "Description of PEM fuel cells system," in *PEM Fuel Cells with Bio-Ethanol Processor Systems* (M. S. Basualdo, D. Feroldi, and R. Outbib, eds.), pp. 49–72, London: Springer, 2012.

[111] V. Bagotsky, *Fuel Cells: Problems and Solutions*. Wiley, 2009.

[112] A. Kamitani, S. Morishita, H. Kotaki, and S. Arscott, "Miniaturized microDMFC using silicon microsystems techniques: performances at low fuel flow rates," *J. Micromech. Microeng.*, vol. 18, p. 125019, 2008.

[113] A. Bieberle-Hutter, D. Beckel, A. Infortuna, U. P. Muecke, J. L. M. Rupp, L. J. Gauckler, S. Rey-Mermet, P. Muralt, N. R. Bieri, N. Hotz, M. J. Stutz, D. Poulikakos, P. Heeb, P. Müller, A. Bernard, R. Gmur, and T. Hocker, "A micro-solid oxide fuel cell system as battery replacement," *Journal of Power Sources*, vol. 177, no. 1, pp. 123–130, 2008.

[114] S. B. Schaevitz, A. Franz, R. Barton, and A. Ludwiszewski, "Fuel cell apparatus and methods." Patent, Mar. 2011.

[115] G. J. Snyder and E. S. Toberer, "Complex thermoelectric materials," *Nature Materials*, vol. 7, pp. 105–114, Feb. 2008.

[116] T. Caillat, "Thermoelectrics for Space Applications: Past, Present and Future." MIT S3TEC Seminar, Nov. 2013.

[117] Y. Gao, A. M. Marconnet, M. A. Panzer, S. LeBlanc, S. Dogbe, Y. Ezzahri, A. Shakouri, and K. E. Goodson, "Nanostructured interfaces for thermoelectrics," *Journal of Electronic Materials*, vol. 39, no. 9, pp. 1456–1462, 2010.

[118] J. A. Nesbitt, E. J. Opila, and M. V. Nathal, "In situ growth of a Yb2O3 layer for sublimation suppression for Yb14MnSb11 thermoelectric material for space power applications," *Journal of Electronic Materials*, vol. 41, no. 6, pp. 1267–1273, 2012.

[119] D. Zhao, C. Tian, Y. Liu, C. Zhan, and L. Chen, "High temperature sublimation behavior of antimony in CoSb3 thermoelectric material during thermal duration test," *Journal of Alloys and Compounds*, vol. 509, no. 6, pp. 3166–3171, 2011.

[120] C. B. Vining, W. Laskow, J. O. Hanson, R. R. der Beck, and P. D. Gorsuch, "Thermoelectric properties of pressure sintered Si0.8Ge0.2 thermoelectric alloys," *Journal of Applied Physics*, vol. 69, no. 8, pp. 4333–4340, 1991.

[121] V. Rinnerbauer, Y. X. Yeng, W. R. Chan, J. J. Senkevich, J. D. Joannopoulos, M. Soljačić, and I. Celanovic, "High-temperature stability and selective thermal emission of polycrystalline tantalum photonic crystals," *Opt. Express*, vol. 21, pp. 11482–11491, May 2013.

[122] G. Humpston, *Principles of Soldering*. Materials Park, Ohio: ASM International, 2004.

[123] P. Socha, "Etching indium to remove oxides." `http://blogs.indium.com/blog/paul-socha/etching-indium-to-remove-oxides`, 2012. Accessed 2015-03-11.

[124] Y. P. Varshni, "Temperature dependence of the energy gap in semiconductors," *Physica*, vol. 34, no. 1, pp. 149–154, 1967.

[125] D. Aiken, M. Stan, C. Murray, P. Sharps, J. Hills, and B. Clevenger, "Temperature dependent spectral response measurements for III-V multi-junction solar cells," in *Photovoltaic Specialists Conference, 2002. Conference Record of the Twenty-Ninth IEEE*, pp. 828–831, May 2002.

[126] D. Martin and C. Algora, "Temperature-dependent GaSb material parameters for reliable thermophotovoltaic cell modeling," *Semiconductor Science and Technology*, vol. 19, pp. 1040–1052, July 2004.

[127] P. Ashburn, "A theoretical and experimental study of recombination in silicon p-n junctions," *Solid State Electronics*, vol. 18, pp. 569–577, June 1975.

[128] M. B. Kleiner, S. A. Kuehn, and K. Haberger, "High performance forced air cooling scheme employing microchannel heat exchangers," *IEEE transactions on components, packaging, and manufacturing technology. Part A*, vol. 18, no. 4, pp. 795–804, 1995.

[129] S. Song, V. Au, and K. P. Moran, "Constriction/spreading resistance model for electronics packaging," in *Proceedings of the 4th ASME/JSME thermal engineering joint conference*, vol. 4, pp. 199–206, 1995.